Changes in X-ray spectra of accreting pulsars on short and long time scales

Dissertation
der Mathematisch-Naturwissenschaftlichen Fakultät
der Eberhard Karls Universität Tübingen
zur Erlangung des Grades eines
Doktors der Naturwissenschaften
(Dr. rer. nat.)

vorgelegt von
Vadim Vybornov
aus Tula, Russland

Tübingen
2018

Gedruckt mit Genehmigung der Mathematisch-Naturwissenschaftlichen Fakultät der Eberhard Karls Universität Tübingen

Tag der mündlichen Qualifikation	20.12.2018
Dekan:	Prof. Dr. Wolfgang Rosenstiel
1. Berichterstatter:	Prof. Dr. Andrea Santangelo
2. Berichterstatter:	Prof. Dr. Klaus Werner

Zusammenfassung

Ein akkretierender Pulsar ist ein rotierender Neutronenstern, der Magnetfelder mit Stärken im Bereich von 10^{12} Gauss hat und Materie von seinem optischen Begleiter akkretiert. Da die Akkretion von Röntgenstrahlung begleitet wird, werden akkretierende Pulsare oft als Röntgenpulsare bezeichnet. Die Energieentnahme erfolgt aus der potenziellen Energie der Materie, die vom optischen Stern entweder durch den Roche-Lobe-Überlauf oder als Sternwind geliefert wird. Solche Neutronensterne sind also durch Akkretion angetriebene Pulsare, im Gegensatz zu Radiopulsaren, die ihre Energie durch die Spinrotation entnehmen.

Akkretierende Pulsare haben bekanntermaßen starke magnetische Dipolfelder. Der Druck des akkretierten Plasmas in der Magnetosphäre wird vom Magnetfeld dominiert.

Wenn das Plasma am Rand der Magnetosphäre erfasst wird, fließt es entlang der Magnetfeldlinien und erreicht dabei eine Geschwindigkeit von ~0.5 c. Dabei bildet das Material Hügel, an welchen sich die Gravitationsenergie in Röntgenstrahlen umwandelt.

Spektren einer Reihe akkretierender Pulsare enthalten ein Absorptionsmerkmal, das durch die Resonanzstreuung von Photonen durch Elektronen in einem extrem starken Magnetfeld verursacht wird. Dieses Merkmal wird daher als Zyklotronresonanzstreuungsmerkmal (CRSF) oder einfach als "Zyklotronlinie" bezeichnet. In aktuellen Modellen wird angenommen, dass die Linie entweder irgendwo im Akkretionshügel oder/und in der von der Neutronensternoberfläche reflektierten Strahlung entsteht. Es wurde kürzlich gezeigt, dass die Energie der Zyklotronlinie in einigen Quellen mit der Röntgenleuchtkraft korreliert ist, d. h. mit der Massenakkretionsrate. Daher kann die Zyklotronlinie verwendet werden, um den Akkretionshügel zu untersuchen. Obwohl zahlreiche Beobachtungen durchgeführt und mehrere Theorien zu Akkretionsprozessen entwickelt wurden, sind viele fundamentale Fragen bezüglich der spectralen Veränderlichkeit in Abhängigkeit von Zeit und Helligkeit, der Struktur der Akkretionshügel und der Wechselwirkungen zwischen dem Magnetfeld und dem akkretierten Plasma immer noch nicht vollständig verstanden.

Um voranzukommen, sind viele qualitativ hochwertige Beobachtungen erforderlich. Die Röntgenweltraummission Nuclear Spectroscopic Telescope Array (NuSTAR), die im Jahr 2012 gestartet wurde, bietet eine gute Gelegenheit, temporäre Röntgenquellen zu untersuchen, von denen viele akkretierende Pulsare darstellen. Der Hauptvorteil der modernen Röntgenoptik von NuSTAR ist die große effektive Fläche bei harten Röntgenstrahlen, die es ermöglicht, die Beobachtungen mit einem ausgezeichneten Signal-Rausch-Verhältnis von 3 keV bis zu 78 keV durchzuführen. NuSTAR hat gute zeitliche und ausgezeichnete spektrale Auflösungen bei hohen Energien. Dehalb ist NuSTAR die hauptsächlich genutzte Datenquelle in dieser Doktorarbeit.

Diese Arbeit konzentriert sich auf Beobachtungen von drei akkretierenden Pulsaren:

Hercules X-1 (Her X-1), Cepheus X-4 (Cep X-4) und V 0332+53. Das Vorhandensein des CRSF in ihren Spektren wurde zuvor bestimmt. Die positive Korrelation zwischen der zentralen CRSF-Energie und der Röntgenleuchtkraft in Her X-1, die mit RXTE erhalten wurde, war auch bekannt. Die Analyse der Daten wurde unter Verwendung der relativ neuen nach Pulsamplituden aufgelösten Technik durchgeführt. Mit dieser Methode erzeugten wir das Spektrum als eine Funktion der Pulsamplitude, was uns erlaubt, die spektrale Leuchtkraftvariabilität auf kurzen Zeitskalen (der Pulsperiode) zu untersuchen. Dies ist wichtig für permanente Quellen wie Her X-1. Die Methode ist auch erfolgreich auf temporäre Quellen anwendbar.

Eine Korrelation zwischen der zentralen CRSF-Energie und der Röntgenleuchtkraft, die mit dieser Methode abgeleitet wird, ist tatsächlich unabhängig von der Zeitvariabilität der Quelle. So konnten wir beispielsweise die Helligkeits- und Zeitabhängigkeiten in V 0332+53 entkoppeln und die reine $E_{\mathrm{CRSF}}/L_{\mathrm{x}}$-Abhängigkeit sowohl von langen als auch von kurzen Zeitskalen untersuchen. Basierend auf dieser Analyse argumentieren wir, dass die Zeitänderungen in der Zyklotronlinienenergie in V 0332+53 durch Änderungen in der geometrischen Konfiguration der Emissionsregion und nicht durch intrinsische Änderungen des globalen Dipolmagnetfeldes entstehen, wie dies zuvor von anderen Autoren vorgeschlagen wurde. Wir bestätigen ebenfalls mit hoher Signifikanz den Übergang von einer Antikorrelation zu einer Korrelation zwischen der Zyklotronlinienenergie und Röntgenleuchtkraft bei $L_{\mathrm{cr}} = (2.1 \pm 0.4) \times 10^{37}$ erg/s in V 0332+53 während des gigantischen Ausbruchs 2015.

Bezüglich Cep X-4 zeigen wir, dass die Energie der Zyklotronlinie positiv mit der Röntgenleuchtkraft und der spektralen Härte korreliert, was das Vorhandensein des unterkritischen Akkretionsregimes in der Quelle während des betrachteten Ausbruchs widerspiegelt. Die erhaltenen Korrelationen wurden verwendet, um ein Modell mit einem kollisionsfreien Schock zu testen, das von den russischen Kollegen von SAI MSU ausgearbeitet wurde. Die Härteabhängigkeit wird mit diesem Modell erfolgreich angepasst, wohingegen die Linienenergiekorrelation dadurch kaum beschrieben wird. Zusätzlich zu diesen Ergebnissen haben wir die harmonische Schwingung des CRSF deutlich erkannt, was frühere Behauptungen aus der Literatur bestätigt.

Die Zeiteigenschaften und Helligkeit von Her X-1 erlaubten uns nicht, die Pulsamplituden aufgelöste Methode anzuwenden. Die Pulsvariabilität der NuSTAR-Lichtkurve wurde von statistischem Rauschen dominiert.

Daher haben wir Einschränkungen der Methode bei realen Daten festgestellt und die Voraussetzungen der Anwendung der Methode zusammengefaßt: Die Quelle sollte hell sein und ihre Pulsperiode sollte lang genug sein, um eine ausreichende Anzahl von Photonen innerhalb eines Pulses zu sammeln, um eine Verteilung von Pulsamplituden zu erzeugen, die breiter ist als die entsprechende Poisson-Verteilung.

Neben der Untersuchung der NuSTAR-Daten von Her X-1 mit der Pulsamplituden-aufgelösten Methode haben wir die bekannte Spektralanalyse angewendet, um zu zeigen, dass die allmähliche Abnahme der Zyklotronlinienenergie während der NuSTAR-Beobachtungen 2015 noch andauert.

Abstract

An accreting pulsar is a highly magnetized rotating neutron star accreting plasma from a non-degenerate optical companion. Since accretion is accompanied by X-ray emission, accreting pulsars are often called X-ray pulsars. The energy sustaining X-ray emission is drawn from the potential energy of the plasma accreted from the donor companion through Roche lobe overflow or stellar winds. Such neutron stars are thus accretion-powered pulsars, unlike radio pulsars, which take their energy from the spin rotation.

Accreting pulsars are known to possess a strong dipole magnetic field, which dominates the accreted plasma pressure inside the magnetosphere. Captured at the outskirts of the magnetosphere, the accreted plasma begins to fall down along the magnetic field lines reaching a velocity of ~0.5 c near the stellar surface. At some height above the magnetic polar cap the accreted material is abruptly decelerated, forming an accretion mound, where the gravitational energy is thermalized into X-rays.

Spectra of a number of accreting pulsars contain an absorption feature caused by the resonance scattering of photons by electrons in an extremely strong magnetic field. This feature is therefore called the cyclotron resonance scattering feature (CRSF), or simply "cyclotron line". According to current models, CRSFs are believed to emerge from the accretion mound or in the radiation reflected from the neutron star surface. The energy of the CRSF in some sources has been recently showed to be correlated with the X-ray luminosity, i.e., with the mass accretion rate. Therefore, the cyclotron line can be used to probe the accretion mound. Despite an intense observational and theoretical research, many of the fundamental issues, concerning the formation of the spectra, their variability with time and luminosity, the structure of the accretion mound, the interactions between the magnetic field and accreted plasma, are still not well understood.

To move forward, plenty of high qualitative observations are needed. The Nuclear Spectroscopic Telescope Array (NuSTAR) mission launched in 2012 provides a good opportunity to investigate X-ray transients, many of which are accreting pulsars. The main advantage of the modern X-ray optics on board NuSTAR is the large effective area at hard X-ray energies allowing to perform the observations with an excellent signal-to-noise ratio from 3 keV up to 78 keV. The good temporal resolution and the excellent spectral resolution at higher energies make NuSTAR the main data source in the present work.

This work focuses on observations of three accreting pulsars, Hercules X-1 (Her X-1), Cepheus X-4 (Cep X-4) and V 0332+53. The presence of the CRSF in their spectra has been previously determined, and the positive correlation between the CRSF centroid energy and X-ray luminosity in Her X-1 obtained with RXTE was also known. The analysis of the data was performed using the so-called relatively new pulse-amplitude-resolved technique. By using this method we produce a spectrum as a function of pulse

4

amplitude, which allows us to investigate spectral-luminosity variability on short time scales of pulse period. This is essential for persistent sources, like Her X-1. The method is also successfully applicable to transient sources.

A correlation between the line centroid energy and flux derived with this method is in fact independent of time variability of the source. This allowed us, for example, to decouple the luminosity and time dependence in V 0332+53, and to investigate the pure $E_{\mathrm{CRSF}}/L_{\mathrm{x}}$ dependence on both long and short time scales. Based on this analysis we argue that the time changes in the cyclotron line energy in V 0332+53 are caused by changes in the geometrical configuration of the emission region rather than by intrinsic changes of the global dipole magnetic field as suggested before by other authors. We also confirmed with high significance the transition from an anti-correlation to a correlation between the cyclotron line energy and X-ray luminosity at $L_{\mathrm{cr}} = (2.1 \pm 0.4) \times 10^{37}$ erg/s in V 0332+53 during the giant 2015 outburst.

Regarding Cep X-4, we showed that the cyclotron line energy is positively correlated with the X-ray luminosity as well as the spectral hardness, reflecting the presence of the sub-critical accretion regime in the source during the considered outburst. The obtained correlations were used for testing a model with a collisionless shock elaborated by the Russian colleagues from SAI MSU. The hardness dependence is successfully fitted with this model, whereas the line energy correlation is hardly described. In addition to these findings, we firmly detected the harmonic of the CRSF, confirming previous claims found in literature.

The time properties and brightness of Her X-1 did not allow us to apply the pulse-amplitude-resolved method. The pulse variability of the NuSTAR light curve turned out to be dominated by statistical noise.

Therefore, we encountered restrictions of the method in real data and concluded the condition of the application of the method: a source should be bright and its pulse period should be long enough to collect a sufficient number of photons within a pulse to produce a pulse amplitude distribution wider than the corresponding Poisson distribution. Besides studying NuSTAR data of Her X-1 using the pulse-amplitude-resolved method, we applied the well established spectral analysis to show that the gradual decay of the cyclotron line energy was still ongoing during the 2015 NuSTAR observations.

Contents

1. Introduction

1.1   Evolution of binary systems

The cradle of stars is cold and dense clouds consisting of molecular hydrogen and dust with a temperature from 5 to 30 K. When a cloud reaches the so-called Jeans mass and size, it begins to shrink irreversibly under gravitational forces, which leads to the formation of a dense structure, in which stars are born. If the size of the cloud is larger than the Jeans length, the cloud is fragmented and each fragment compresses separately. In real conditions, the rotation of the cloud, magnetic fields, presence of the radiation of other stars and other factors also play a role opposing the gravitational forces. Since the compressed cloud is optically thick because of the presence of an amount of dust, the energy released during the compression can not effectively escape the cloud, and the temperature and pressure in the center thus increase until thermonuclear reactions start. At this stage of the evolution the protostar becomes an infant star, which then follows the so-called Hayashi track towards the main sequence if the mass is less than $3\,M_\odot$. If the mass is more than 3 solar masses, the star begins its evolution right from the main sequence without the pre-main-sequence phase. Note that at the pre-main-sequence phase, the compression of the star under gravitational forces plays the dominant role in the energy release, whereas at the main sequence, the energy release is caused by the nuclear fusion of hydrogen into helium called the proton-proton chain (pp-chain).

A star remains near its initial point on the main sequence as long as thermonuclear reactions take place in the core. It occurs on the nuclear timescale

$$\tau_n = \frac{0.1 M \eta}{L} = 10^{10} \frac{M}{M_\odot} \frac{L_\odot}{L} \text{ yr} \tag{1.1}$$

where M and L are the mass and luminosity of the star in solar masses and luminosities, η is the efficiency of the pp-chain and the coefficient 0.1 is the mass fraction of the star available for the hydrogen fusion on the main sequence.

As the star consumes the hydrogen fuel in the core, the gas pressure decreases and the star begins to shrink until the pressure and temperature in the hydrogen-abundant layers of the envelope become enough to ignite the hydrogen in these layers, providing sufficient energy generation to balance the gravitational pressure. At this stage the star leaves the main sequence and passes on to the giant branch. Once all hydrogen is consumed, the star contracts again and the pressure and temperature in the core become so high that helium starts to burn into carbon through the triple α-process. When helium is exhausted, the nuclear burning of heaver elements begins. Cycles of nuclear burning and gravitational contractions continue until the non-thermal pressure of the core matter can balance the gravitational pressure. If the mass of the core is less than $1.4\,M_\odot$ (the Chandrasekhar

limit), electron degeneracy pressure stops the core collapse, so that the core becomes a white dwarf and the expanding outer layers form a planetary nebula. If the mass of the core is more than $1.4\,M_\odot$, the core undergoes a rapid collapse into a neutron star or a black hole accompanied by a supernova explosion. Therefore, the evolution of the star is determined primarily by its initial mass, though the chemical composition should also be taken into account.

Solar-mass stars are known to be born mostly in binaries or multiple systems. The binary frequency for solar-mass stars is more than 60% and increases to high-mass stars, that is the majority of stars in our galaxy are members of binaries or multiple systems. In this regard, it is important to consider the evolution of stars in binaries because they can influence one another through tidal forces, heating or mass transfer. The mass transfer is the most important process, substantially changing the evolution of stars in binary systems.

A binary system with masses of components M_1 and M_2 has a modified gravitational potential called the Roche potential

$$\Phi = -\frac{GM_1}{r_1} - \frac{GM_2}{r_2} - \frac{\omega^2 r_3^2}{2} \tag{1.2}$$

where ω is the orbital angular velocity, r_1, r_2 and r_3 are the distances to the center of the star of M_1, with the mass M_2 and to the rotation axis, respectively. Contours of equipotential lines in the orbital plane of the binary are shown in Fig. 1.1. One of the properties of the Roche potential is that each star has its own sphere of gravitational influence, called the Roche lobe, beyond which the matter can not be attracted by the corresponding star. The size of a lobe R can be estimated with the approximation

$$\frac{R}{a} = 0,38 + 0.2\log\frac{M_1}{M_2} \tag{1.3}$$

where a is the major semi-axis of the system.

The Roche lobes of the stars in the binary touch each other in the inner Lagrangian point (usually referred to as L_1-point). Since there is an unstable equilibrium at this point, the material around this point can leave one star and be captured by another.

Evolution changes in the system begin from the more massive component (component I hereafter). Leaving the main sequence, component I plumps up until its envelope overfills the Roche lobe and begins to flow toward the secondary component through the L_1-point. At this moment component I stops expanding and loses mass intensively. This mass transfer is unstable, because the decrease of the mass of component I leads to a smaller Roche lobe and, according to the law of conservation of momentum, to a smaller distance between stars. This results in a higher rate of the mass transfer. Because of the accelerating transfer rate, the material piles up on the accretor and, in the end, overflows its Roche lobe. This leads to the formation of a common envelope around the binary. Further evolution is accompanied by the friction between the common envelope and the binary makes the stars spiral towards each other until the envelope has been ejected Paczynski (1976). In the end of the spiral-in phase, a much closer system with a period up to 10 days is left. If the release of the orbital energy during the spiral-in phase is not sufficient to eject the common envelope, the components come closer until they have been merged in a rapidly rotating star such as FK Com. The common envelope stage is supposed to
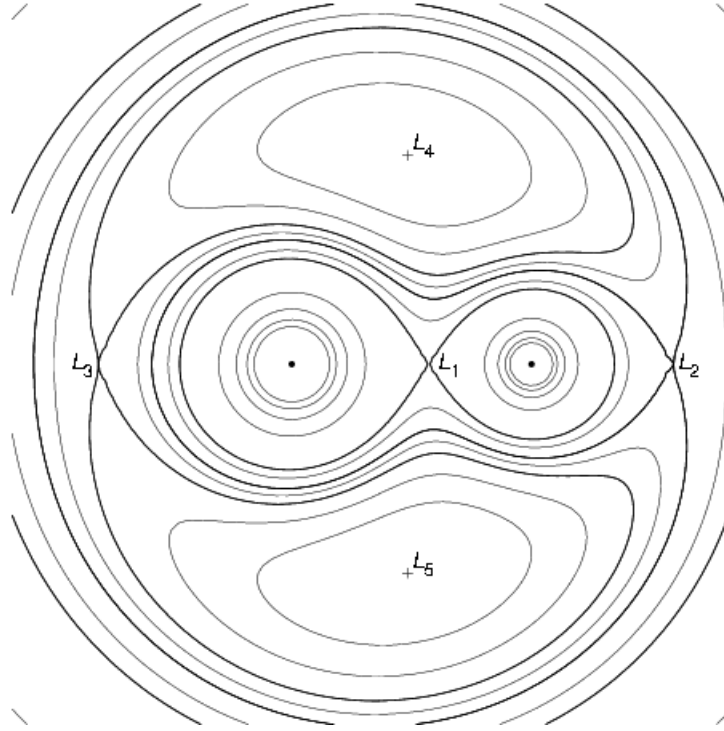
Figure 1.1: Contours of Roche equipotentials in the orbital plane of a binary with the labeled Lagrangian points. Credit: Wikipedia

be an important link in the binary evolution because it is hard to explain the formation of short-period binaries containing a compact object without losing momentum during the spiral-in stage Podsiadlowski et al. (2002); Ivanova et al. (2013).

Since at this stage component I leaves the main sequence and moves to the giant branch, that is this component has a helium core without thermonuclear reactions, the mass transfer occurs on timescales close to the Kelvin-Helmholtz timescale:

$$\tau_K = \frac{GM^2}{RL} = 3 \cdot 10^7 \left(\frac{M}{M_\odot}\right)^2 \frac{R_\odot}{R} \frac{L_\odot}{L} \text{ yr} \qquad (1.4)$$

where M, R and L is the mass, the radius and the luminosity of the donor star.

As a result of the mass transfer, the mass of the secondary star has significantly increased (up to a few times), while a helium remnant remains instead of the primary component. The secondary component thus becomes more massive than the primary component, which was initially more massive. Note that the less massive helium remnant is at a later evolutionary stage than the more massive now secondary component and brighter than a main-sequence star with the same mass. Such a situation is called the Algol paradox. The helium remnant usually has a thin hydrogen envelope and is considered to be a Wolf-Rayet star (WR-star) with the temperature of $\sim 10^5$ K and strong wide emission lines in the optical spectrum. In relatively rare cases the WR star can fill the Roche lobe and evolve further with formation of a star with a helium-rich envelope and a CO-core Delgado & Thomas (1981).

The further destiny of the helium remnant depends on its core mass. If the mass is less than the Chandrasekhar limit, a white dwarf forms. If the mass exceeds the Chandrasekhar

limit, the remnant explodes as a supernova of type Ib or Ic turning into a neutron star or a black hole. The second component has gained the mass but still remains a main-sequence star. The system does not brake up owing to the supernova explosion because the lower mass component explodes. However, the center of the mass of the system can start to move with velocities of about ~ 100 km/s, so that the system can move away from the galactic plain for several hundred parsecs.

Once the relativistic object has been born, it becomes optically very faint and the binary is in fact observed as a single star. But if a star has a high altitude above the galactic plane, one can suspect that it is a component of a binary system. Indeed, quasi-periodic oscillations in light velocities of many of "run-away" bright stars are observed, implying an invisible compact satellite.

A few million years after the supernova explosion, the normal component begins to expand filling its Roche lobe and the history repeats: the matter flows through the first Lagrange point and is accreted by the relativistic object. When the matter is accreted by the compact object, a huge amount of energy releases as electromagnetic radiation. Specific characteristics of the radiation and the energy spectrum depend on the type of the compact object. Here below only neutron stars will be considered as compact objects in binaries.

1.1.1 Low-mass X-ray binaries

X-ray binaries are traditionally divided into two groups: low-mass X-ray binaries (LMXBs) with the masses of the donor star of $\lesssim 1.5\,M_\odot$ and high-mass X-ray binaries (HMXBs) with donor masses of $\gtrsim 10\,M_\odot$. Such a division is not only formal but has a more fundamental base. These two classes have different space distributions and the material from the donor star transfers towards the NS in different ways.

There are only about 200 LMXBs in our Galaxy, which makes them sufficiently rare objects (Liu et al. 2007), meaning that specific conditions are needed for the formation of these binaries. Indeed, while the donor star in the system has the mass less than $1.5\,M_\odot$, the progenitor of the NS has to be a star with the mass $\gtrsim 10\,M_\odot$. Since the binary system typically loses more than half of the initial mass after the supernova explosion, the system should be destroyed, if only the vector of the kick momentum is not opposite oriented to the vector of the orbital velocity of the NS progenitor. There is however no guarantee that the binary remains bound in this case (Pfahl et al. 2003).

The second difficulty is that the typical separation between components in a LMXB is $0.1 - 10 R_\odot$, which is smaller than the radius of the NS progenitor (Liu et al. 2007; Revnivtsev et al. 2011). In other words, LMXBs are very close systems, implying the existence of a common envelope and a spiral-in phase at some stage of the evolution as a most effective mechanism to reduce the separation (Brandt & Podsiadlowski 1995). Nevertheless, despite of the difficulties, these systems are observed, and it is still unclear weather the mass of the donor star does not change after the supernova explosion or the low-mass binary descends from a binary with a donor star of an intermediate mass.

As shown in Fig. 1.3, LMXBs are distributed sufficiently widely with respect to the Galaxy disc. This fact has the following explanation. The neutron star is believed to receive a large kick during the supernova explosion. If the system remains bound after this event, the kick momentum is transferred to the whole system and as a consequence, the
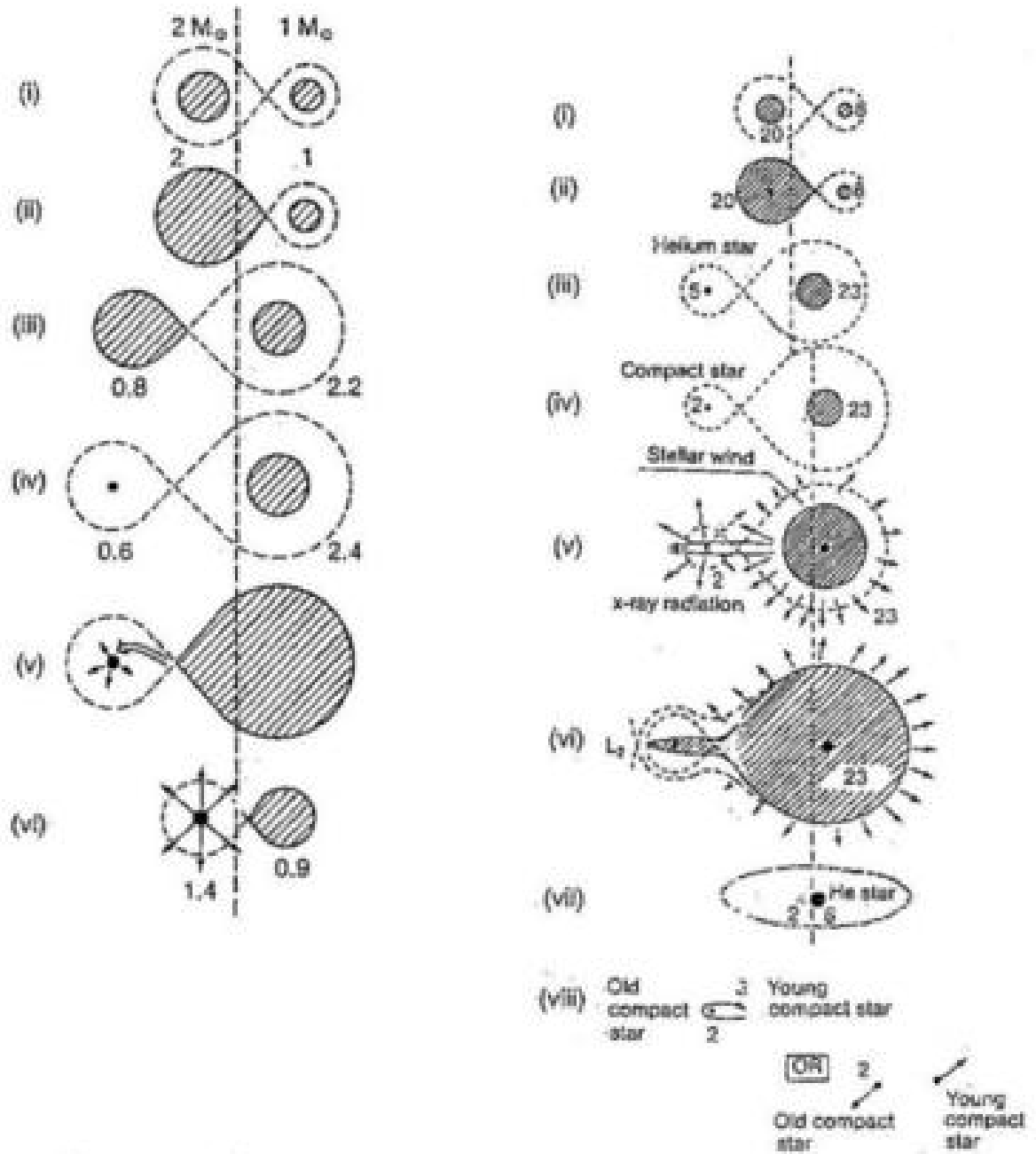
Figure 1.2: Two main pathways for stellar evolution in binary systems. On the left, evolutionary scenario for LMXBs, on the right: evolutionary scenario for HMXBs. Source: Karttunen et.al. 1987.
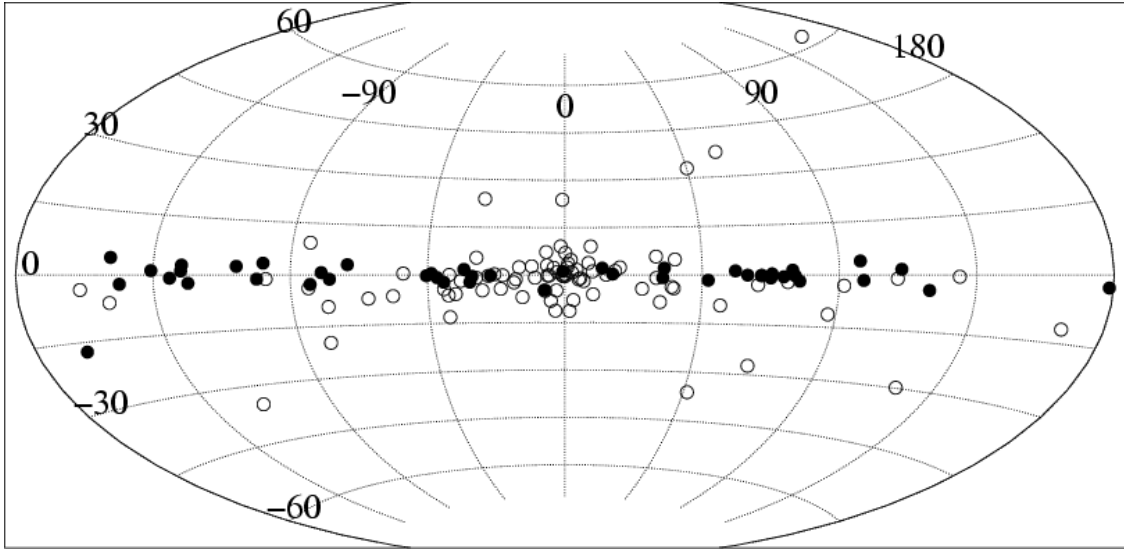
Figure 1.3: Distribution of LMXBs (open circles) and HMXBs (filled circles) in the Galaxy. Credit: Grimm et al. (2002)

center of mass of the binary has a proper motion. Possessing the same kick momentum, the binaries with lower masses apparently receive a larger kick velocity than the binaries that contain a high-mass companion. Since LXMBs are old systems, they are able to move further away from the galactic plane than the binary with a high-mass companion and a shorter lifetime. This explanation is in agreement with the simulations performed by (Brandt & Podsiadlowski 1995).

Since LMXBs contain a star with medium or low luminosity, which does not posses strong stellar winds, accretion can take place only through the Roche lobe overflow. The matter, flowing via the first Lagrangian point, forms a disc around the NS since it still has an angular momentum due to the rotation of the system. This type of accretion is called disc accretion. Note that in this case the accretion is dynamically stable because the mass of the donor star is smaller than the mass of the NS.

1.1.2 High-mass X-ray binaries

If an X-ray binary system hosts a luminous high mass component of the O-B spectral type (supergiants with mass typically more than $10\,M_\odot$), this system is referred to High-Mass X-ray Binary (HMXB). In this case accretion also can occur through overflowing of the Roche lobe, however a more common scenario is wind-fed accretion. Indeed, supergiants I/II stars possess a dense and sufficiently slow stellar wind, so that the NS directly accretes the matter when passing through the wind. Such binaries, hosting a supergiant star are combined in a subclass, called sgHMXBs. Many HMXBs contains a Be-class star as a donor component (often called BeHMXBs). A Be star rotates so rapidly that its matter outflows from the equator, resulting in formation of a circumstellar disc, sometimes called the decretion disc. The existence of the decretion disc is evidenced by observations of the H_α emission line. Again, when the compact object travels trough the disc, accretion occurs. In the both cases a comet-like tail is formed as, for instance, in Vela X-1 (Doroshenko et al. 2013; Malacaria et al. 2016).
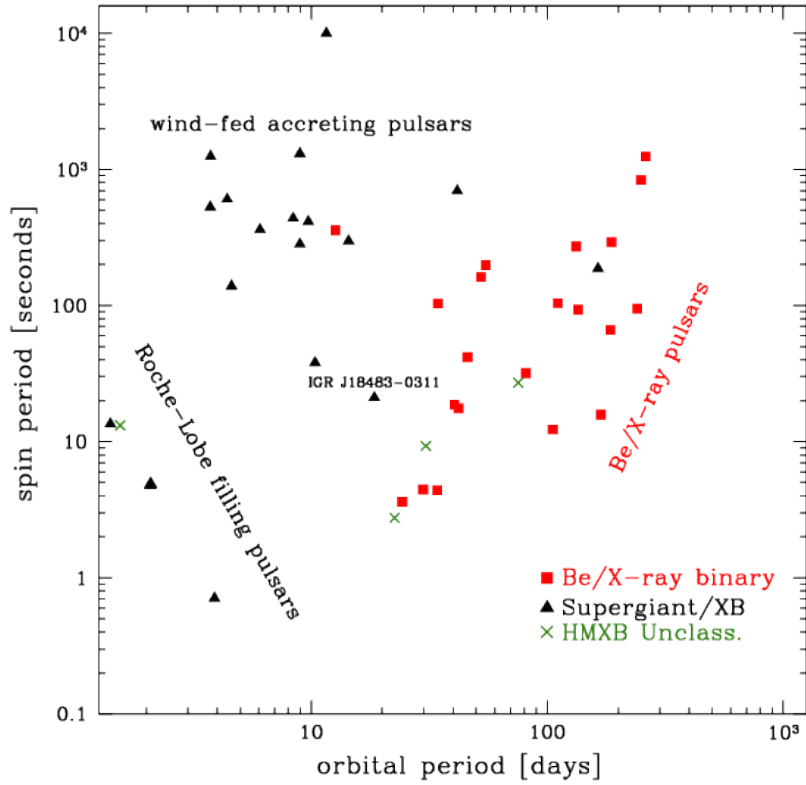
Figure 1.4: Corbet diagram of the HMXBs with three sub-classes of these objects, which are localized in distinct areas. BeHMXBs exhibit a wide positive correlations between P_{spin} and P_{orb}, whereas Roche lobe overflow HMXB systems show a negative correlation, and wind-fed systems have no correlation.

In BeHMXBs, however, accretion has a non-stationary character because the decretion disc is tilted and/or the orbit of the NS is eccentric (Okazaki & Negueruela 2001a; Reig 2007). This is manifested in outbursts, classified as Type I and Type II outbursts. When the NS periodically accretes the matter during its passages through the circumstellar disk, Type I outbursts are observed. In addition to periodical Type I outbursts, sources with a Be star normally show transient X-ray Type II outbursts. They are distinguished by their giant intensity in comparison with Type I outbursts. The phase of Type I outbursts are also observed to be shifted, likely due to the superperiodical rotation and changes of the circumstellar disk structure (see i.e. McGowan & Charles 2003). In some cases the absence of a persistent accretion could be explained by the fact that the circumstellar disc is truncated at some resonance distance inside the Roche lobe, which is caused by the presence of the compact object and tidal torques associated with it (Okazaki & Negueruela 2001b).

Note that sgHXMBs do not exhibit periodical Type I outbursts because the orbit of the NS tends to be circular, resulting in the presence of the compact object inside the stellar wind. Since the wind is almost symmetric, sgHXMB sources are mostly persistent X-ray sources, though the wind contains flow denser clumps, which makes accretion unstable. This leads to flares when X-rays flux can be drastically enhanced (Runacres & Owocki

14

Table 1.1: Parameters of the X-ray binaries that host a neutron star.

Type	LMXBs	HMXBs
Donor star	$K - M$ or WD	$O - B$
Age, yr	10^{10}	10^7
Orbital period, days	$0.01 - 10$	$1 - 100$
Accretion	disc	wind or/and disc
Magnetic field of NS, G	$10^7 - 10^9$	$\sim 10^{12}$

2005; Walter & Zurita Heras 2007; Leahy & Kostka 2008).

It is also interesting to note that BeHXMB and sgHXMB are situated in different parts of the Corbet diagram, which shows the neutron star pulse period as a function of the orbital period of the system (Corbet 1986). This diagram may be useful because it reflects intersections between accreted material and the neutron star. As can be seen from Fig. 1.4, BeHMXB systems differ from others showing a wide positive correlation between $P_{\rm spin}$ and $P_{\rm orb}$, which likely reflects the fact that in closer systems accretion acts occur more frequently with more dense accreted material, leading to a higher acceleration of the NS rotation.

1.2   Accretion onto a neutron star

1.2.1   X-ray pulsars

An accreting X-ray pulsar is a rotating highly magnetised ($B > 10^{11}$ G) neutron star (NS) accreting matter from an optical companion. The active study of these objects has been started since the discovery of pulsations in the X-ray source Cen X-3 (Giacconi et al. 1971). Accreting pulsars are observed only in binary systems since the matter from the companion is needed to maintain the accretion and X-ray emission, while amount of interstellar matter is not sufficient to make accretion visible in isolated NSs. Since accreted material is a plasma and the NS possesses a strong magnetic field, in the vicinity of the NS surface the matter can flow only along the magnetic field lines towards the NS magnetic poles, where it is decelerated from a free-fall velocity of around $0.6\,c$ and heated to $\gtrsim 10^8$ K, resulting in hard X-ray radiation. Since the magnetic poles are not located where the axis of rotation is, a distant observer sees pulses of the X-ray emission. Therefore, such objects are named accreting or X-ray pulsars by analogy with radio pulsars, which exhibit pulses of radio emission. To date, more than 200 accreting pulsars are known[1].

Regardless of the class of an X-ray binary, an accretion disk is most likely to be formed because the accreted matter, transferring from the donor component to the compact object, has an angular momentum due to the binary rotation, even if the accretion is wind-fed. The disc thus plays a key role in accretion processes for all types of X-ray binaries.

The neutron star magnetic field is considered to have a dipole structure at distances of more than several NS radii. This magnetic field apparently prevent the propagation of

---

[1]http://www.iasfbo.inaf.it/~mauro/pulsar_list.html

accreted matter at some radius, called the stopping radius R_s. This radius is determined differently, depending on the the type of accretion. The interaction between the magnetic field and accreted plasma differs significantly for the spherical accretion and the accretion with a rotating disc. While in the case spherical accretion onto a slowly rotating NS the stopping radius is mostly determined by the balance between the magnetic field and the matter pressures and corresponds to the so-called Alfvén radius, the interaction between the plasma and matter in the inner zone of the accretion disc is much more complicated and demand to take into account plasma instabilities, perturbations in the accretion disc and other effects. Depending on specific parameters of the object, acceleration torques can arise as well deceleration torques. One of the first work on the interaction between a rotation higly magetized NS and a accretion disc is Ghosh & Lamb (1978). However, the stopping radius in the case of the disc accretion is in the order of the Alfvén radius, which is determined by the equilibrium of the magnetic and plasma pressures.

The magnetic energy density is

$$P_m = \frac{B^2}{8\pi} = \frac{\mu^2}{8\pi r^6} \tag{1.5}$$

where B is the induction of the magnetic field and μ is the dipole magnetic moment. The energy density of the free falling matter is

$$P_f = \frac{1}{2}\rho v^2 = \rho \frac{GM}{r} \tag{1.6}$$

where ρ is the density, v is the free fall velocity for an object with the mass M. Suggesting for simplicity a spherically symmetric flow, i.e.

$$\rho = \frac{\dot{M}}{4\pi v r^2} \tag{1.7}$$

where $\dot{M}$ is the mass accretion rate. P_f can then be rewritten:

$$P_f = \frac{\dot{M}}{4\pi}\left(\frac{GM}{2r^5}\right)^{\frac{1}{2}} \tag{1.8}$$

The Alfvén radius, i.e. where the balance is approached, is

$$R_A = \left(\frac{\mu^4}{2GM\dot{M}^2}\right)^{\frac{1}{7}} \simeq 3.2 \times 10^8 \, \dot{M}_{17}^{-2/7} \mu_{30}^{4/7} \left(\frac{M}{M_\odot}\right)^{-\frac{1}{7}} \text{ cm} \tag{1.9}$$

where $\dot{M}_{17}$ is the mass accretion rate in units of 10^{17} g/s and μ_{30} is the magnetic momentum in units of 10^{30} Gauss cm^3.

Note that the magnetic energy density goes as r^{-6}, while the energy density of the free falling material goes as $r^{-5/2}$, implying that the magnetic field pressure increases much more rapidly with decreasing distance from the NS than the material pressure does. Therefore, the magnetic stresses are dominated by the material stresses far from the NS. For typical accreting pulsar fields of around 10^{12} Gauss, the magnetic stresses dominate close to the NS's surface.

At the Alfvén radius the accreted plasma is supposed to be frozen and dragged by the magnetic field, which forces the plasma to rotate as a solid body with the angular velocity
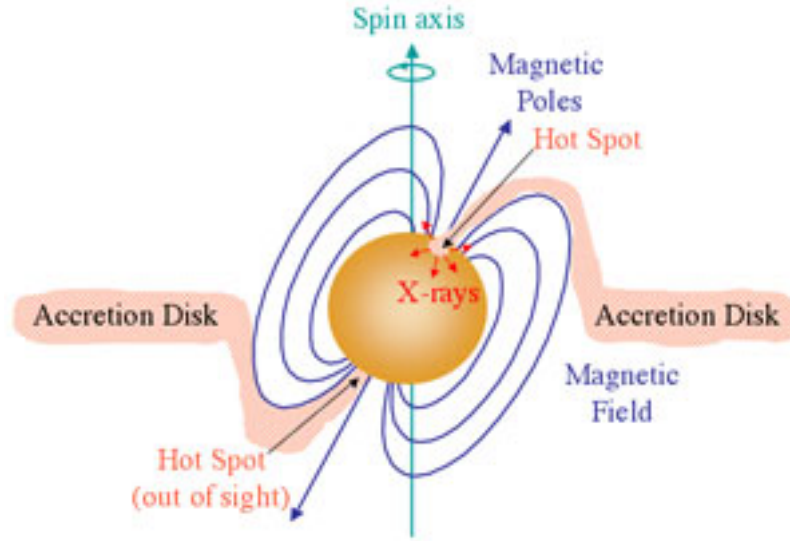
Figure 1.5: Sketch of an accreting pulsar showing accretion disc and the accretion matter flowing along field lines towards the magnetic poles. Source: http://astronomy.swin.edu.au

of the NS. The matter will apparently be accreted if its tangential velocity is less than the Keplerian velocity at the Alfvén radius,

$$\frac{2\pi}{T}R_A < \sqrt{\frac{GM}{R_A}} \tag{1.10}$$

or

$$R_A < \left(\frac{GMT^2}{4\pi^2}\right)^{\frac{1}{3}} = R_{cor} \tag{1.11}$$

where T is the spin period of the NS. The right side determines the so-called corotation radius R_{cor}, where the velocity of the solid body rotation is equal to the Keplerian velocity. If the tangential velocity is more than the Keplerian velocity, the centrifugal force makes the matter move outwards, and no accretion occurs (Pringle & Rees 1972; Lamb et al. 1973; Illarionov & Sunyaev 1975). The phase when $R_A > R_{cor}$ is called the propeller regime, where the analog of the propeller is the rotating NS. In this regime the NS undergoes spin-down because the NS angular momentum is transmitted to the accretion disc through the magnetic field. Sooner or later, the NS spins down, so that the accretion can take place. However, during accretion the NS is known to spin up, which can lead to the propeller regime again.

Therefore, if $R_A < R_{cor}$, the accretion flow can approach the NS surface radiating X-rays, which is observed as an accretion pulsar. If $R_A > R_{cor}$, the centrifugal force does not allow the matter to be accreted. Note, the necessary condition for a NS to be an accreting pulsar is that the Alfvén radius must be longer than the NS radius, implying minimal magnetic field to be 10^8 Gauss.

As already mentioned, accretion pulsars can spin up and spin down depending on the ratio between the Alfvén radius and corotation radius. These properties of the accreting pulsars turn out to be very useful to probe physical issues of accretion because a spin-up and spin-down can be measured from observations with high accuracy.

17

Qualitatively, spin-up and spin-down rates can be calculated from the consideration of the balance of acceleration and deceleration torques. The transmission of angular momentum occurs in the Alfvén zone at R_A (Ghosh & Lamb 1978). As shown by Pringle & Rees (1972), in the case of disc accretion the acceleration torque is

$$K_+ = \dot{M}\sqrt{GMR_A}. \tag{1.12}$$

Note that the upper limit for K_+ is apparently achieved at R_{cor} because at longer radii the matter is ejected by centrifugal forces. The deceleration torque is associated with friction forces arising between the magnetosphere and turbulence plasma in the Alfvén zone. It is worth noting that both the acceleration torque and deceleration torque are simultaneously present during accretion. (Elsner & Lamb 1977) showed that the resulting torque depends on the parameter defined as a ratio between the Alfvén radius and corotation radius

$$\alpha = \left(\frac{R_A}{R_{cor}}\right)^{\frac{3}{2}}. \tag{1.13}$$

A neutron star undergoes a spin-up when $\alpha \lesssim 0.8$. If $0.8 \lesssim \alpha \lesssim 1$, the NS spins down. The ejection of matter occurs when $\alpha > 1$ (Ghosh & Lamb 1978). This relation apparently depends on the magnetic moment μ and mass accretion rate $\dot{M}$ since R_A depends on these parameters. Based on rival torques, Ghosh & Lamb (1979) derived an expression for the period change,

$$-\dot{T} = f_1(\alpha)f_2(\mu, M)\,T^2\,L_{37}^{6/7}, \tag{1.14}$$

where $f_1(\alpha)$ is a dimensionless function whose sign changes depending on α, $f_2(\mu, M)$ is a dimensionless function of the magnetic moment μ and the mass of the NS M and L_{37} is the luminosity in units of $10^{37}\mathrm{erg\,s^{-1}}$. Accreting pulsars usually show a spin-up, in particular in outbursts, when active accretion processes take place, though spins-down are sometimes observed in some sources such as Her X-1 (Parmar et al. 1999; Oosterbroek et al. 2001).

It is also interesting to note that during its evolution, an accreting neutron star tends to be in a state, in which the acceleration torque and deceleration torque are balanced (Davidson & Ostriker 1973; Lipunov & Shakura 1976). The accretion, however, turns out to be unstable at this stage because, and small variations in mass accretion rate lead to the transition of the neutron star from accreting state to the propeller state and back, which is reflected in dramatic luminosity changes (Lipunov 1987).

Regardless of accretion type, accreted matter can flow only along magnetic field lines falling onto the magnetic pols (Fig. 1.6). In the vicinity of the neutron star surface, the matter accelerates up to $\sim 10^{10}\mathrm{cm\,s^{-1}}$, implying the efficiency of the energy release is $0.1\dot{M}c^2$, which makes the accretion onto a NS the most effective way of energy release (e.g. thermonuclear reactions have an efficiency output of $0.007Mc^2$). Specific mechanisms of energy release depend on mass accretion rate.

Since the flow of accreted matter within the magnetosphere is completely governed by the magnetic field, the energy is released in the region above the sufficiently small polar caps having a radius for a dipole magnetic field of about 1 km (Davidson & Ostriker 1973). The energy release is mostly in X-ray photons. Where and how these photons are born is still not fully understood but there are two qualitatively different regimes of breaking of accreted matter (Basko & Sunyaev 1976).
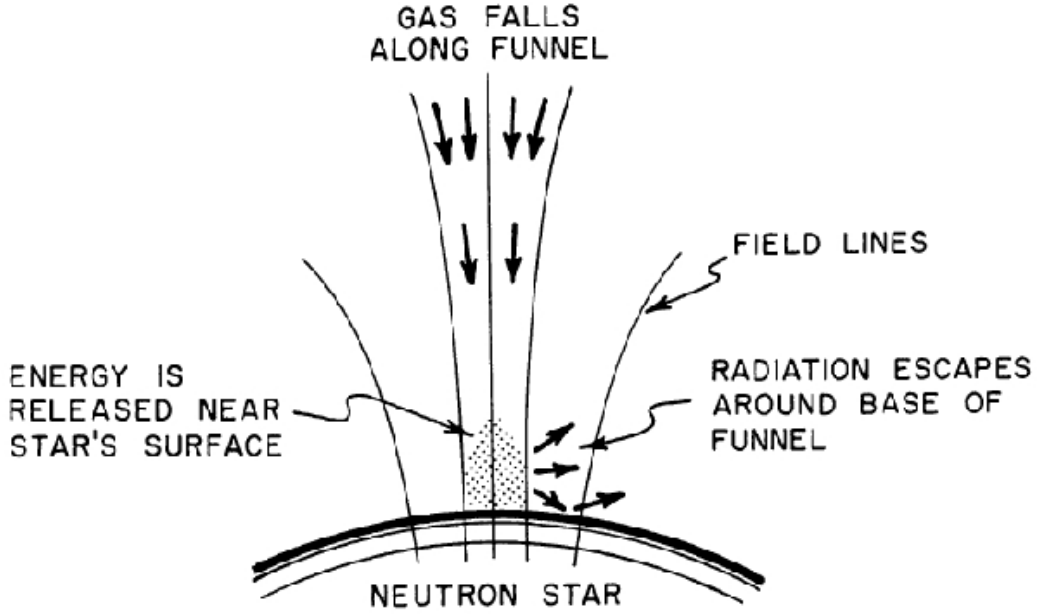
Figure 1.6: Sketch of the funnel formed by the magnetic field of the neutron star. Being governed by the strong magnetic field, the matter falls onto a polar cap of area of about 1km^2. Source: Davidson & Ostriker (1973).

The first regime – sub-critical regime – is realized at sufficiently low luminosity, when breaking of the falling matter occurs either in the NS atmosphere through Coulomb collisions (Staubert et al. 2007; Becker et al. 2012) or in a collisionless shock at a height of order of several hundred meters above the NS surface (Rothschild et al. 2017; Vybornov et al. 2017). In this case photons escape from a thin layer above the stellar surface mostly upwards forming a pencil-like X-ray beam (Basko & Sunyaev 1975).

As mass accretion rate increases, more photons appear in the same volume giving rise to a higher photon density and to a higher radiation pressure. At some accretion rate corresponding to a critical luminosity L_{cr}, the photon pressure and the pressure of the falling matter are balanced, which is associated with reaching of the local Eddington limit (Basko & Sunyaev 1976)

$$L_{\text{Edd}}^* = \frac{4\pi G M m_{\text{p}} c}{\sigma_{\text{T}} R_{\text{NS}}} \frac{r_{\text{cap}}}{R_{\text{NS}}} \tag{1.15}$$

where m_{p} is the proton mass, σ_{T} is the Thompson cross-section, r_{cap} and R_{NS} are the radii of the polar cap and the neutron star, respectively. Deriving the Eddington limit, the Thompson cross-section is supposed, but in presence of high magnetic fields the interaction between photons and electrons is much more complicated (Gnedin & Sunyaev 1973). There are different approaches to estimate the L_{cr} (Basko & Sunyaev 1976; Wang & Frank 1981; Becker et al. 2012; Mushtukov et al. 2015b), which give values of the order of $\sim 10^{37} \text{erg s}^{-1}$. However, some sources (such as V 0332+53, 4U 0115+63, EXO 2030+375) are known to reach luminosities of the order of $\sim 10^{38} \text{erg s}^{-1}$ during outbursts. To explain the accretion in these sources Basko & Sunyaev (1976) suggested the presence of an optically thick accretion column above the polar cap, which is formed when radiation pressure begins to dominate the pressure of the infalling matter. The higher the mass accretion rate, the more significant the radiation pressure, and conse-
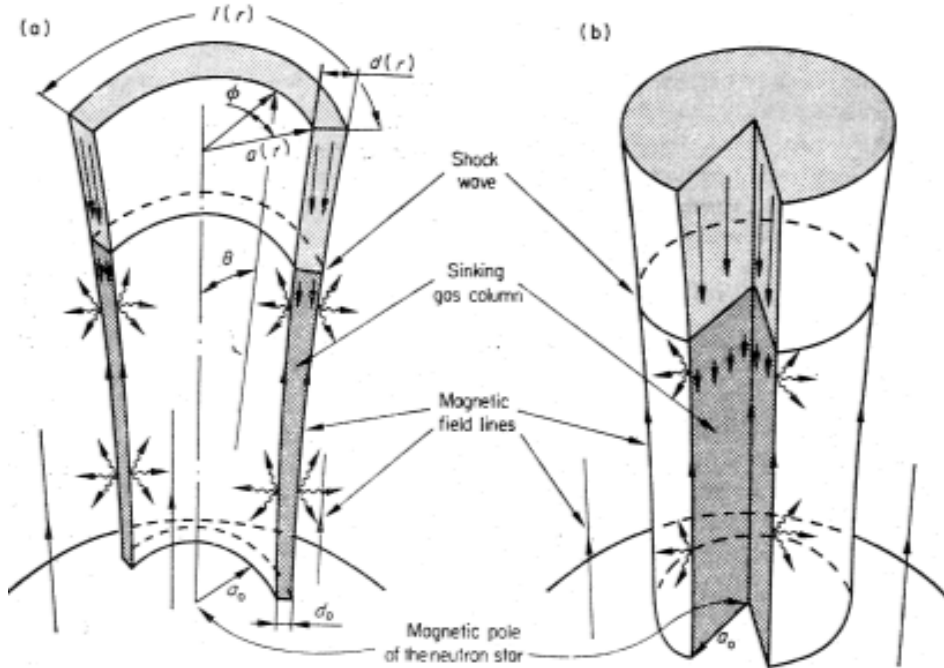
19

Figure 1.7: Two tipes of the radiation-dominated accretion column according to Basko & Sunyaev (1976): "hollow" (left) and "solid" (right). In the case of the "hollow" columns the infalling matter is confined to a wall of the funnel created by the magnetic field, whereas in the "solid" geometry the matter fills the whole funnel. Source: Basko & Sunyaev (1976).

quently, the taller the column. When the accretion column is formed, most of the photons is supposed to escape through sidewalls forming a fan-like emission beam (Lyubarskii 1986). In this case the regime is known as the super-critical regime, in which the infalling matter decelerates in a radiative shock. The height of the radiative shock is the order of kilometer.

Two kind of structure of the accretion column are suggested, "solid" and "hollow" columns, depending on the magnetic field structure (Fig. 1.7). The height of the "hollow" column should be lower than the "solid" at the same level of luminosity because the "hollow" column has a larger square of the wall sides at the same height. Basko & Sunyaev (1976) also suggested that the spectrum such columns is a power law with a cut-off at high energies. Indeed, continua of X-ray spectra of accreting pulsars are usually well described by a power law (in the 5-20 keV energy range) with an exponential cut-off at energies of 20-30 keV (Coburn et al. 2002). The continuum is thought to be formed due to bulk and thermal Comptanization (inverse Compton scattering) of blackbody seed photons coming from a region near the NS surface to higher energies by relativistic electrons in the accreting flow. Despite the same underlying physics, specific spectrum shape varies from source to source. This could be the result of different geometry and effects of gravitational light bending (Kraus 2001; Kraus et al. 2003), reflection of the radiation escaping from the accretion column by the NS surface (Poutanen et al. 2013; Postnov et al. 2015), etc.

In addition to a continuum, a prominent absorption feature, caused by the resonance scattering of photons in a strong magnetic field, is observed in the spectra of some X-ray pulsars. This feature is known as the cyclotron resonance scattering feature (CRSF) or

the cyclotron line. A few sources have two or three CRSFs in their spectra, which are harmonics of the fundamental line. The feature is a very important to probe the column structure. Properties of CRSF are discussed in more detail in the last subsection of the present chapter. Besides CRSFs, spectra of accreting pulsars include a blackbody component with the maximum at ~ 1 keV and the Kα fluorescent emission iron line at ~ 6.4 keV produced in the accretion disc or accretion flow.

1.2.2 Other cases

X-ray bursters

In accreting pulsars matter can flow only towards the polar caps where an accretion mound is formed. The existence of the accretion mound is possible by the strong magnetic field, which forms funnels above the polar caps. However, if the magnetic field is so weak that the Alfvén radius is on the order of NS's radius or smaller, accreted matter can be accumulated on large part of the neutron surface, and accretion manifests itself as periodical flaring activity. Indeed, many of neutron stars in LMXBs have a sufficiently weak magnetic field because these binaries are old systems and the magnetic field fades away with time.

The neutron stars in such binaries exhibit an eruptive activity with a periodicity from few hours to days. Between active phases persistent accretion occurs, and the matter is accumulated on the surface of the neutron star. As the matter is piled on, the temperature and pressure in the settled down layers increase, reaching critical values, at which the accreted hydrogen and helium are ignited. These periodical surges of activity, known as Type I X-ray bursts, are caused by burning of accreted mix of hydrogen and helium on the stellar surface, i.e they have the thermonuclear nature. The thermonuclear nature of the bursts comes from the fact that energy released during accretion between bursts is a few hundred times greater than the energy released during the bursts, reflecting the distinction between the accretion and fusion efficiencies.

The bursts show a sudden development with a rise time of a few seconds and decay during tens or hundreds of seconds (Fig. 1.8). The decay phase is shorter at higher energies and the time profile at this phase is usually well described by a simple exponential law. Note that such Type I bursts should not be confused with Type I outbursts in accreting pulsars because their physics and observational properties are completely different.

Although X-ray bursts take their energy from thermonuclear reactions, the specific type of reaction is distinct in each case, depending on mass accretion rate (Fujimoto et al. 1981; Fushiki & Lamb 1987a). At the lowest accretion rates hydrogen burns unstably, provoking helium ignition. At higher accretion rates hydrogen burning is stable between bursts, contributing to helium accumulation underneath the burning hydrogen layer. The temperature and pressure gradually increase until the pure helium layer ignites. The helium then burns via the α-process very unstably (Fushiki & Lamb 1987b). At accretion rates comparable to the local Eddington rate ($8.8 \times 10^4 \mathrm{g\,s^{-1}cm^{-2}}$), helium begins to burn steadily depleting the fuel of the bursts, and thus causing the termination of the flare activity (Paczynski 1983; Taam et al. 1996).

The X-ray bursts have blackbody spectra with a temperature of a couple of keV (Swank et al. 1977). The measured radius of the body emitting this thermal radiation turns out to be around 10 km, which is consistent with the typical radius of a neutron
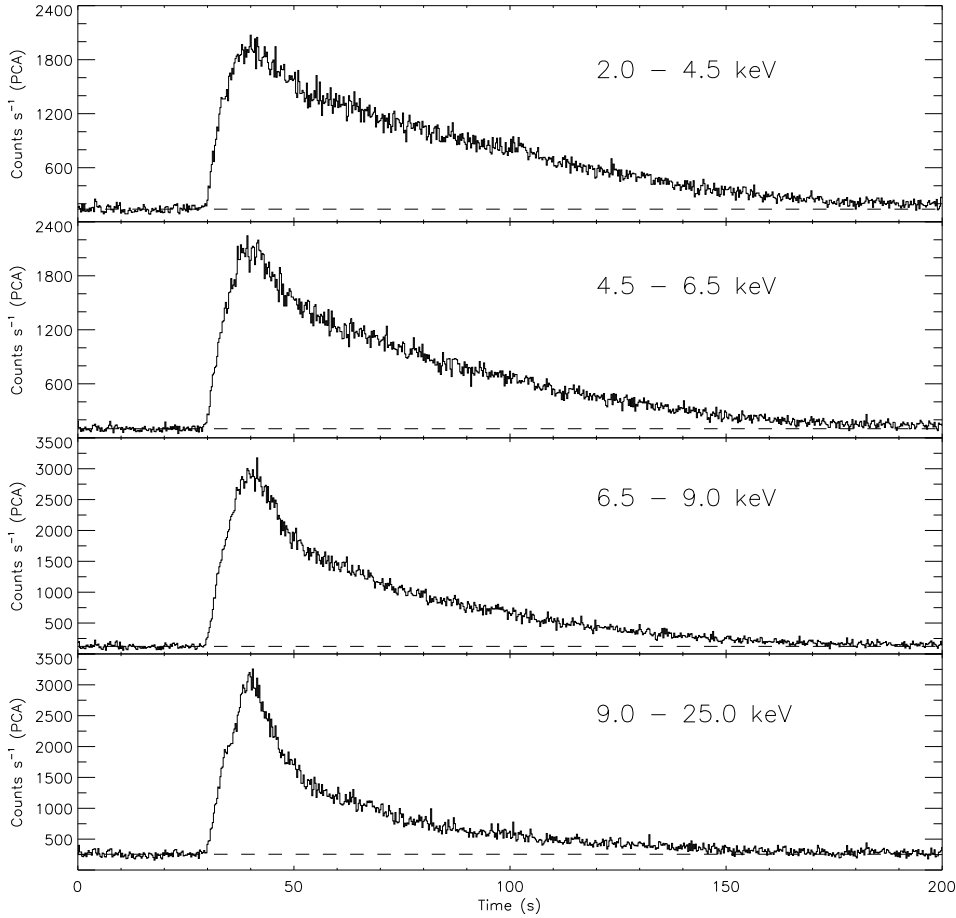
Figure 1.8: Example of a Type I X-ray burst in GS 1826-238 observed by RXTE/PCA in several energy bands. The decay time depends on energy, decreasing with increasing photon energy. Source: Kong et al. (2000).

star (Hoffman et al. 1977). Note that the original maximum of burst spectra should be at higher energies than that corresponding to the effective temperature of the radiative layer because of Compton scattering in the stellar atmosphere (London et al. 1984, 1986; Ebisuzaki & Nakamura 1988; Titarchuk 1994b).

A comprehensive review of X-ray bursts properties may be found in Strohmayer & Bildsten (2003).

ULX pulsars

In some cases the energy released in accretion onto neutron stars could be raised to as much as $10^{39} - 10^{41} \mathrm{erg\,s^{-1}}$. Because of their high luminosity level, such sources are called ultraluminous X-ray pulsars (ULXPs). Initially, all sources with such high X-ray luminosity were thought to be stellar-remnant black holes with intermediate masses (up to $100\,M_\odot$) because it is a challenge to explain this enormous luminosity within theoretical conceptions of accretion onto a neutron star. However, recently Bachetti et al. (2014) discovered pulsations with a period of 1.37 seconds from one of the ULXs. To date only thee ULX pulsars are known, M83 X-2 (Bachetti et al. 2014), NGC 7793 P13 (Fürst et al. 2016), NGC 5907 (Israel et al. 2017). All these sources share common properties: they

have a similar pulse period on the order of one second and show a strong gradual spin-up, caused by their high accretion rates. In addition to pulsations, the time profiles of the sources exhibit a long-term modulation of a couple of months (Walton et al. 2016; Kong et al. 2016; Hu et al. 2017). There are a few theoretical models to explain such extreme luminosities and to define the magnetic field of these objects (Mushtukov et al. 2015a; Kluźniak & Lasota 2015; Brightman et al. 2018), however the phenomenon of ULX pulses is far from being fully understood.

Transitional millisecond pulsars

Another intriguing class of objects showing accretion onto a neutron star is transitional millisecond pulsars. The most prominent characteristic of these objects is that they are alternatively observed in two completely different states: as an accretion-powered X-ray pulsar or a rotation-powered-radio millisecond pulsar. The idea that slowly rotating young neutron stars in binary systems could be spun up to millisecond periods and be observed as rapidly spinning radio pulsars by disc accretion has been proposed long ago (Alpar et al. 1982; Radhakrishnan 1982). This suggestion however remained a theoretical hypothesis until the radio pulsar J1023+0038, having a period of 1.7 ms, was discovered in 2007 (Archibald et al. 2009). The coordinates of the radio pulsar were coincident with a source previously suspected as a cataclysmic variable (Bond et al. 2002; Thorstensen & Armstrong 2005).
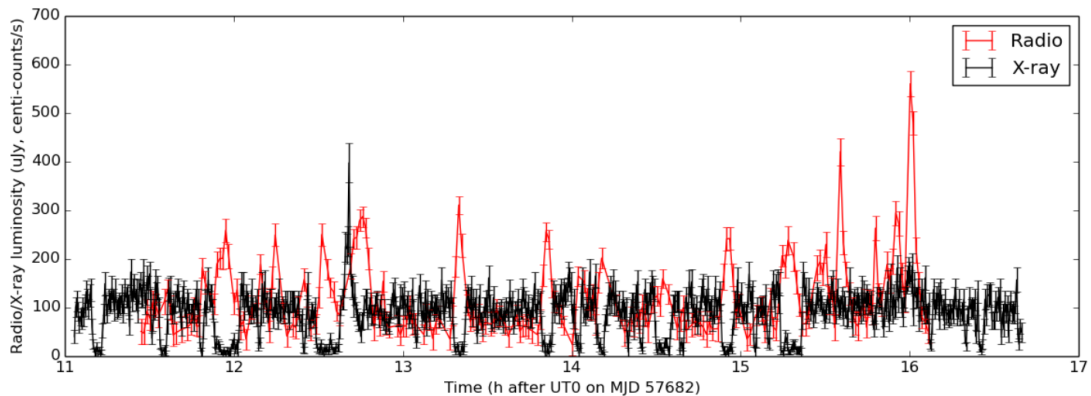

Figure 1.9: Anticorrelation of the VLA radio and Chandra X-ray light curves observed in J1023+0038. Source: Bogdanov et al. (2018).

The second transitional pulsar IGR J18245–2452 located in the globular cluster M28 was discovered in March 2013 as an X-ray transient observed with INTEGRAL, Swift and XMM-Newton. The 0.5-10 keV luminosity was 3.5×10^{36} erg s^{-1} The position and ephemerides were coincident with the previously known radio pulsar PSR J1824–2452I. This object switched its mode and began being observed as a radio pulsar, showing thus a direct confirmation of the recycling scenario for spin-up of the millisecond neutron stars. In June 2013, the source went into an accretion state again, being visible simultaneously in γ-rays and the optical band (Patruno et al. 2014; Stappers et al. 2014). Radio emission disappears during accretion states as in the case of J1023+0038 (Fig. 1.9).

To date, the last known such an object is the Fermi-LAT source XSS J1227-4859, which was in a radio pulsar mode in December 2012 and 2014 (Bassa et al. 2014; Roy et al. 2015).

1.3 Cyclotron resonance scattering feature

X-ray spectra of some accreting pulsars exhibit absorption-line-like features called cyclotron resonance scattering features (CRSFs), or cyclotron lines[2]. The first such line was discovered in 1976 during a balloon observation of Her X-1 (Trümper et al. 1978). Thanks to launches of X-ray space observatories such as Suzaku, RXTE and especially NuSTAR, the number of sources with a cyclotron line in the spectrum has been rapidly increased and, to date, around 30 such sources are known. In some cases harmonics of the cyclotron line are also detected.

Because of magnetic flux conservation after the supernova explosion, neutron stars possess very strong magnetic fields reaching the critical field strength

$$B_{\text{crit}} = \frac{m_e^2 c^3}{e\hbar} = 4.4 \times 10^{13} G \qquad (1.16)$$

where m_e, e are the electron mass and charge, and c is the speed of light.

In these conditions the momentum and the energy of a free electron in plasma are quantized, similarly to the Bohr's hydrogen atom model. The electron in such strong magnetic fields can thus occupy only discrete energy states, called Landau levels, radiating or absorbing a photon in transition between them. If a photon has the energy that corresponds to the transition energy, it is absorbed by the electron and immediately emitted in other direction. Such scattering processes alter the spectral and spatial distribution of the photons in the medium so that the optical depth at the transition energy is increased and, as a result, the absorption feature, called cyclotron line, is observed.

The energy of the cyclotron line corresponds to the difference between Landau level n and the fundamental state with $n = 0$

$$E_{\text{cyc}} = \frac{\hbar e}{m_e c} nB = 11.6[\text{keV}]B_{12}n, \qquad (1.17)$$

where B_{12} is the magnetic field strength in units of 10^{12} Gauss. To get the observed energy, the gravitation redshift z has to be taken into account

$$E_{\text{cyc}}^{\text{obs}} = \frac{E_{\text{cyc}}}{1 + z}. \qquad (1.18)$$

The fundamental cyclotron line corresponds to transition between the Landau level $n = 1$ and the fundamental state. If $n > 1$, lines are referred to as harmonics.

The magnetic field in plasma is known to introduce an asymmetry in the motion of charge particles and interactions between them. The cross-section of the cyclotron scattering thus depends on the angle between magnetic field lines and an incident photon, which will then be scattered by an electron. The cross-sections are sharply shaped at the resonant energies and shifted from each other the angle between magnetic field lines and

---

[2]http://www.iasfbo.inaf.it/~mauro/pulsar_list.html

the incident photon (Gonthier et al. 2014; Schwarm et al. 2017). Figure 1.10 shows cross-sections corresponding to different energies of photons, which excite the electron from the ground state to a higher state. The parameter $\mu = \cos\theta$, where θ is the angle between magnetic field lines and the incident photon.
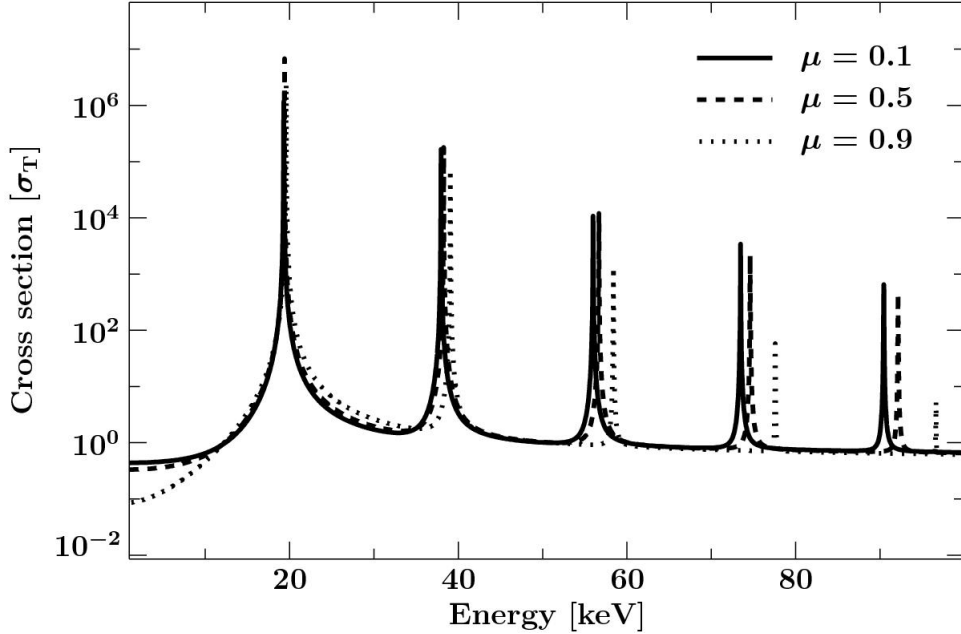

Figure 1.10: Scattering cross-section of an electron in the magnetic field $B = 0.04B_{\mathrm{crit}}$ as a function of the exiting photon energy obtained from Monte-Carlo simulations by Schwarm et al. (2017). The peaks correspond to the electron transitions from the ground Landau level with $n = 0$ to levels with $n < 7$, meaning that the first peak is the fundamental cyclotron resonance. The peaks are shifted from each other with parameter $\mu = \cos\theta$, where θ is the angle between magnetic field lines and the incident photon. Credit: (Schwarm et al. 2017)

The cyclotron feature has been found to change with X-ray luminosity L_{X} in the spectra of a few accreting pulsars. The correlation between the CRSF centroid energy E_{CRSF} and L_{X} has so far been firmly confirmed in six sources. Four of them exhibit a positive correlation for the fundamental line, one for the first harmonic (Vela X-1), and one X-ray pulsar (V0332+53) exhibits both a negative correlation at high luminosities and a positive one at low lumonosities for the fundamental line. Below a brief summary of the $E_{\mathrm{CRSF}}/L_{\mathrm{X}}$ correlations observed in these sources is provided.

- *Her X-1* is probably the best observed and investigated source that exhibits a cyclotron line feature discovered by Trümper et al. (1978) in 1976 using a balloon observation. This is also the first source where a tight positive $E_{\mathrm{CRSF}}/L_{\mathrm{X}}$ correlation was reported by Staubert et al. (2007) using RXTE observations. Klochkov et al. (2011) confirmed the correlation on a short timescale using a pulse-to-pulse analysis technique, which is a kind of the flux-resolved spectroscopy.

- *GX 304-1*. Yamamoto et al. (2011) discovered a CRSF with RXTE and Suzaku during the 2010 outburst and reported a marginal indication of a positive correlation

between its energy and the X-ray flux. The correlation was detected with high significance using INTEGRAL (Klochkov et al. 2012; Malacaria et al. 2015) and RXTE (Rothschild et al. 2017) data.

- *A 0535+26.* The source spectrum has two CRSFs: the fundamental and the first harmonic (Kendziorra et al. 1994; Caballero et al. 2008). A positive E_{CRSF}/L_X correlation for the fundamental line was first found on a short timescale, using the pulse-to-pulse technique applied to RXTE and INTEGRAL/ISGRI observations of a source outburst (Klochkov et al. 2011). The correlation was subsequently confirmed on longer timescales by Sartore et al. (2015) using INTEGRAL/SPI data.

- *Cep X-4.* During one of the outbursts, in 1988, pulsations as well as the CRSF in the spectrum at around 30 keV were detected, establishing the nature of the source as an accreting pulsar (Koyama et al. 1991; Mihara et al. 1991). Thanks to RXTE observations of the source during the 2002 outburst, the hardness of the spectral X-ray continuum was reported to increase with increasing luminosity, whereas the cyclotron line energy was independent of luminosity and was re-measured to be at around 31 keV (McBride et al. 2007). The source awoke again in 2014, after a 12-years snooze, with a giant Type II outburst, which was observed by NuSTAR and Suzaku (Fürst et al. 2015). The flux-resolved analysis of the NuSTAR spectra results in a detection of a tight positive correlation between the cyclotron line energy and luminosity (Vybornov et al. 2017). Vybornov et al. (2017) also revealed a harmonic of the cyclotron line in the NuSTAR data, which was reported by Jaisawal & Naik (2015) earlier, without a considerable dependence on X-ray luminosity.

- *Vela X-1.* The source spectrum also has two CRSFs interpreted as the fundamental line and the first harmonic, but the fundamental feature is considerably weaker than the first harmonic. A positive E_{CRSF}/L_X correlation for the harmonic line is observed in the source spectrum (Fürst et al. 2014; La Parola et al. 2016).

- *V 0332+53.* The fundamental cyclotron line in the source spectrum was discovered during the 1983 outburst with *Ginga* (Makishima et al. 1990). During subsequent outbursts, two harmonics were detected (Pottschmidt et al. 2005; Kreykenbohm et al. 2005). The energy of the fundamental CRSF was found to be negatively correlated with the source X-ray luminosity (Mowlavi et al. 2006; Tsygankov et al. 2006, 2010). Note, this is the only source for which a negative E_{CRSF}/L_X correlation is confirmed so far. Moreover, the source exhibits also a positive E_{CRSF}/L_X correlation at low luminosities as showed by Doroshenko et al. (2017), being thus a unique accreting pulsar with the two types of E_{CRSF}/L_X correlation.

There are also X-ray pulsars, in which an indication for a correlation between the CRSF energy and luminosity is reported but not unambiguously confirmed so far, such as 4U 0115+63 (Müller et al. 2013b; Iyer et al. 2015) and 4U 1538-522 (Hemphill et al. 2014).

Besides the positive E_{CRSF}/L_X correlation in Her X-1, the energy of the cyclotron line has been found to vary with time on a years time scales (Staubert et al. 2016, and references therein). Her X-1 thus is the first source for which a secular change of the CRSF has been reported. The fundamental cyclotron line energy of V 0332+53 has been recently

revealed to vary with time during the giant 2015 outburst (Cusumano et al. 2016) describing a hysteresis in a $E_{\mathrm{CRSF}} - L_{\mathrm{X}}$ graph (Doroshenko et al. 2017). Analyzing the NuSTAR observations during this outburst and the minor 2016 outburst (Type I), Vybornov et al. (2018) showed that the time drift of the line energy breaks at the transition from the negative $E_{\mathrm{CRSF}}/L_{\mathrm{X}}$ correlation to the positive one. The third object with a time dependence of the cyclotron line energy is Vela X-1, in which La Parola et al. (2016) revealed that the energy of the first harmonic has a long-term decay using Swift/BAT data over an almost decade.

2. Instrumentation and methods

2.1 Nuclear Spectroscopic Telescope Array (NuSTAR)

2.1.1 Mission overview

The Nuclear Spectroscopic Telescope Array (NuSTAR) mission was launched on a Pegasus XL rocket from the Kwajalein Atoll on June 12, 2012. The launch was undertaken with an air-launch system with the rocket released from the "Stargazer" L-1011 aircraft. After the launch, the NuSTAR satellite was brought to its normal equatorial low-Earth orbit at an altitude of approximately 600 km with an inclination of 6 degrees. Such an orbit was chosen in order to minimize effects associated with the passage through the South Atlantic Anomaly (SAA), a region with a high concentration of particles trapped in the Earth's inner Van Allen belt. These particles are responsible for a high level of radioactive background produced in detectors of hard energy X-ray observatories, which is why the almost equatorial orbit is preferable.

Table 2.1: Parameters of the NuSTAR mission.

No. of telescopes	Mass	Power	Orbit height	Orbit inclination	Lifetime
2	350 kg	600 W	~630 km	6°	~10 yr

The NuSTAR observatory is designed to perform a relatively long (form hours to several days) pointed observations. During an observation the telescope remains in the same position, being pointed to the target source even though the source is occulted by Earth. The observing efficiency for a typical source ($-50° > \delta > 50°$) is thus around 55%, and it is about 90% for sources at high declination. The attitude control is provided by a system of four star trackers. To use a solar array with a single axis of rotation and to simplify the thermal design of the detectors, the observatory is oriented so that one of its sides always faces the Sun, leaving the possibility for pointing to a selected source only by rotation around the Sun-Earth line. Therefore, the observation conditions depend on when during the year the target source can be observed.

2.1.2 Optics

NuSTAR is the first launched mission equipped with focusing high-energy X-ray optics, which operates at energies between 3 and 79 keV. The observatory consists of two telescopes as similar as possible to each other. Each telescope contains an X-ray optics
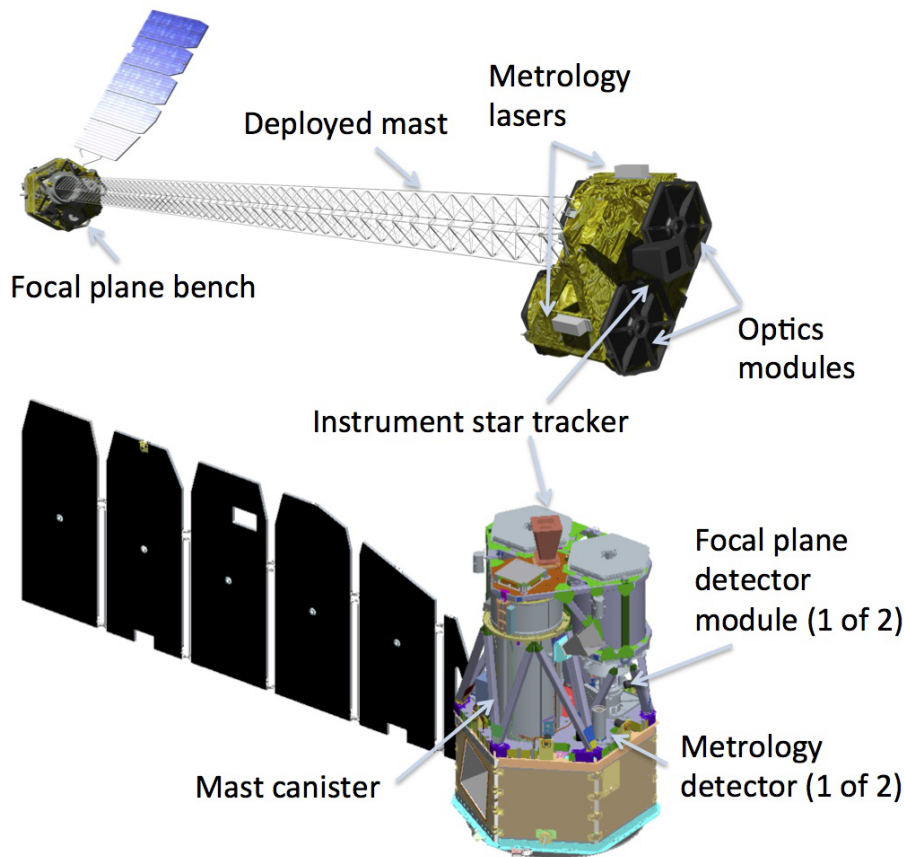
Figure 2.1: NuSTAR observatory in operation with the deployed mast (top) and in the stowed pre-launch configuration (bottom). Source: Harrison et al. (2013).

module and a detector module in the focal plane. The focal plane and optics modules are separated from each other with a mast deployed in orbit (Fig.2.1) by a distance of 10.14 m, which is the focal length of the optic system.

In spite of the mast isothermal design, small deflections remain due to alternating of night-day conditions, leading to motion of the optical axis. The typical amplitude of the axis deviation on the focal plane detector during a orbit cycle is around 3 mm, which corresponds to $1'$. To control the mast motion and to remove the effect thereof, a metrology system, consisting of two infrared lasers situated on the optic module and focused on corresponding detectors on the focal plane bench, is used.

The NuSTAR X-ray optics are conceptually based on the Walter-I design, however the real implementation is a conical approximation to this geometry (Hailey et al. 2010). Although the conical modification makes slightly worse the sharpness on axis, it increases the quality of the image of off-axis sources. In the Walter-I optic layout X-rays are reflected twice, from upper parabolic mirrors and then from lower mirrors shaped as hyperbolas. As shown on the scheme in Fig. 2.3, the incoming incident light is nearly parallel
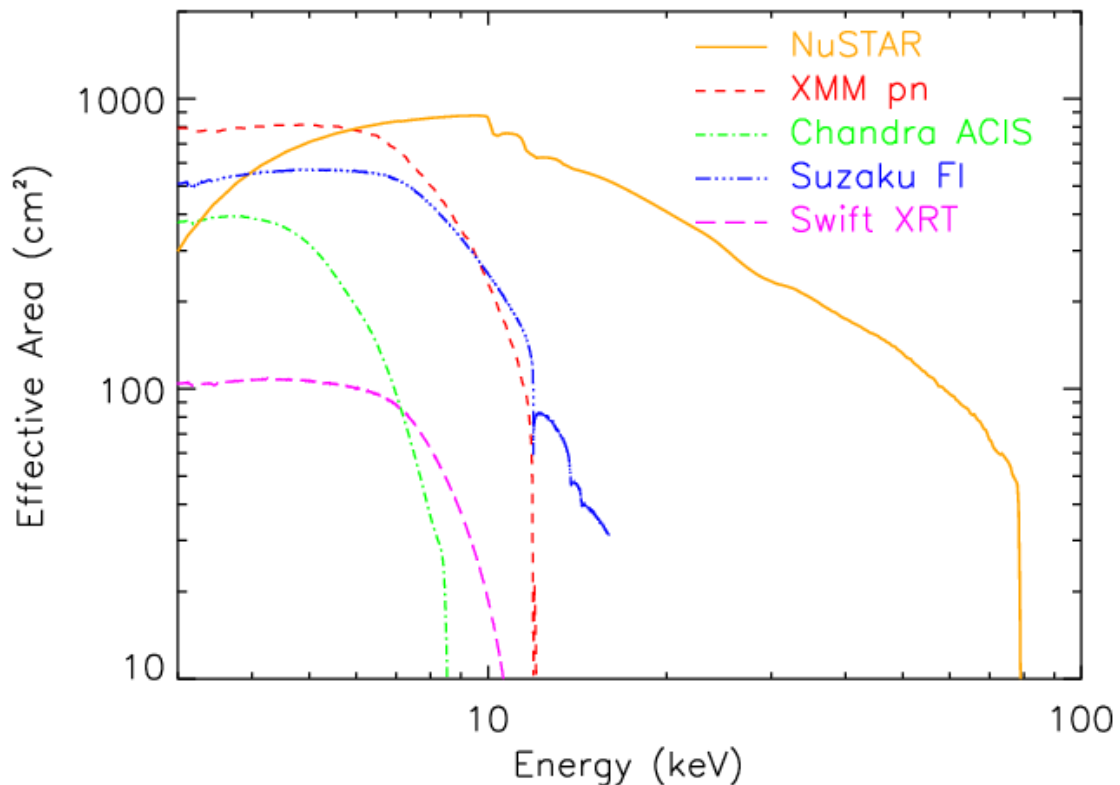
Figure 2.2: Effective area of NuSTAR compared to that of other X-ray observatiories. Despite a slightly lower capabilities at lower energies, above 10 keV, NuSTAR dominates, extending the operating energy band up to 79 keV. Source: Harrison et al. (2013).

to the surfaces of the mirrors, resulting in a small collecting area of a mirror. To resolve this problem, i.e., to fill out the aperture, several mirrors are nested tightly to each other. Each NuSTAR optic consists of 133 concentric mirror shells.

Besides a small incidence angle of light, the reflection of X-rays depends on the material of the mirror, in particular on the coating. The NuSTAR mirrors, unlike previous X-ray focusing missions such as XMM-Newton and Chandra, are coated with structures called depth-graded multilayers (Christensen et al. 2011). The use of this approach allows optics to effectively reflect X-rays up to 79 keV, which was unreachable with past missions possessing X-ray optics. A multilayer consists of 200 pairs of coatings. Each pair is two alternating materials having highly different densities, providing significantly enhanced reflectivity. NuSTAR utilizes Pt/SiC and W/Si multilayers, to operate at energies up to 79 keV. The upper border of the energy range is defined by the Pt K-absorption edge at 78.4 keV, above which the reflective efficiency decreases drastically.

In addition to the extension of the operating energy range, the depth-graded multilayers approach increases the grazing angle, thereby increasing the field relative to standard metal coatings. Nevertheless, higher energy photons are reflected at shallower grazing angles, resulting in a decrease of the effective field of view with photon energy. Note that although the shape of the NuSTAR point-spread function depends on off-axis angle, the integral of this function does not change with off-axis angle.
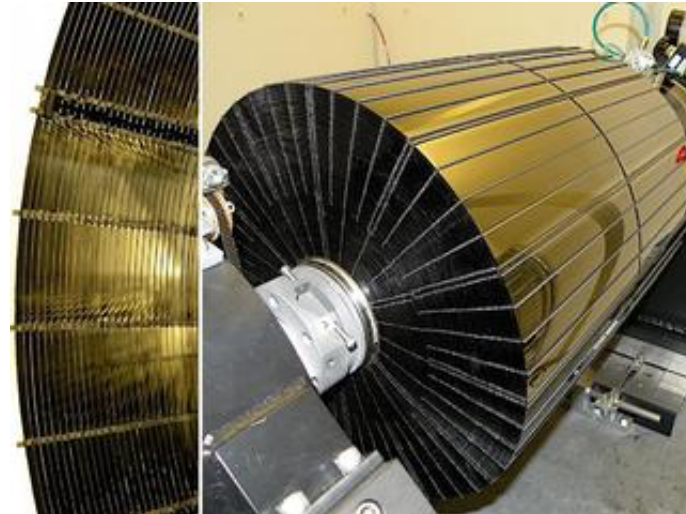
(a)
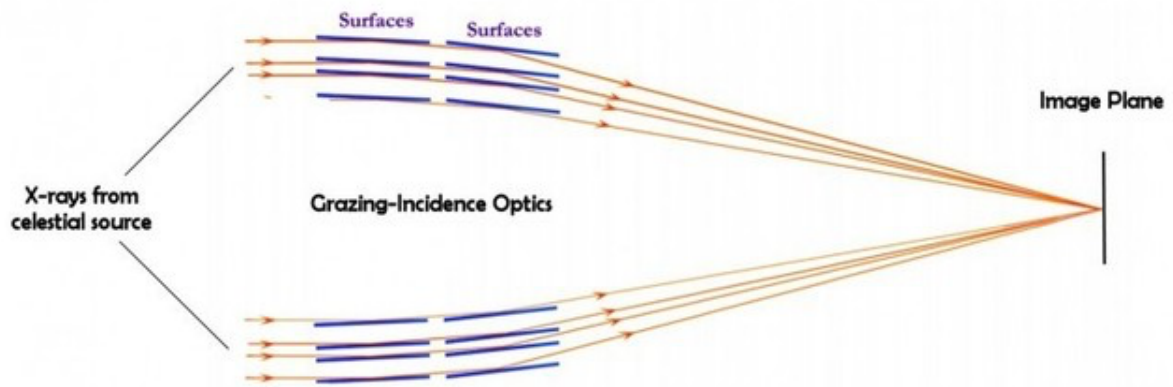
(b)

Figure 2.3: (a) Layers of the X-ray NuSTAR optics separated by graphite spaces (left) in the process of assembling (right). (b) Principal layout of the NuSTAR optics. Credit: https://www.nustar.caltech.edu.

2.1.3 Detectors

Each of the two NuSTAR telescopes has an independent set of electronics and detectors at the focal plane. The detector unit is composed of four solid CdZnTe detectors (Fig.2.4), each with a size of 20 mm x 20 mm x 2 mm divided into 32 x 32 pixels, which corresponds to a 12′ field of view.

The detector units are shielded by CsI crystals, whereby an anti-coincidence guard of the CdZnTe detectors is provided. The anti-coincidence shield is necessary to ignore the events occurred simultaneously in the detectors and the shield, suppressing thus spurious background and improving the signal-to-noise ratio.

The readout in the NuSTAR detectors, unlike CCDs (charge-coupled devices), is carried out from every pixel with its own discriminator. Given the information on the position of the pixel with the highest current, the electronics also read out current pulses from eight neighbour pixels (Rana et al. 2009; Kitaguchi et al. 2011). Therefore, the position
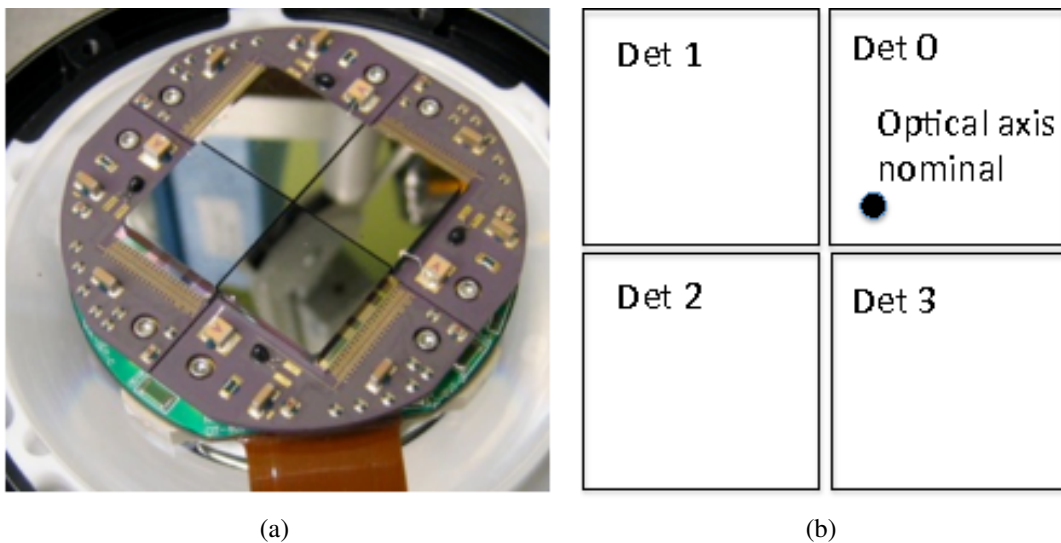
(a)   (b)

Figure 2.4: NuSTAR solid CdZnTe detectors, aranged as 2x2 array, situated at the focal plane (top). Each detector is divided into 32x32 pixels (i.e., with a pixel size in the sky of 12″.3). The default position of the optical axis is on Det 0, approximately 1′ from the chip border. Source: Harrison et al. (2013).

and energy of an interacting photon are calculated from the combined nine-pixel signal.

Since the signal is read out from all pixels independently, the detector is almost free from the pule-up effect (up to fluxes of $\sim 10^5$ counts s^{-1} pixel^{-1}), which is, for example, quite a serious matter in the case of the XMM-Newton's *EPIC-pn* detector. However, due to a sufficiently large processing time (2.5 ms), the NuSTAR detectors suffer from the dead-time effect, which limits the count rate to ~ 400 counts s^{-1}. The dead-time effect in the NuSTAR detectors begins to play a role from even smaller fluxes of ~ 100 counts s^{-1}. Nevertheless, the architecture of the NuSTAR electronics makes it possible to restore the incident flux well. The dead-time correction is crucial, especially for carrying out a timing analysis or an investigation of power-density spectra.

2.1.4 Key properties

The major property, defining the quality of every astronomical optical system, is the point-spread function (PSF). The point-spread function is the overall response of the system to a point source, which is a convolution of the image built by the optics and detector response. In the case of NuSTAR, the residual errors that remain after the mast position reconstruction also are included into the output response. Despite these errors, the dominant term in the point-spread function is the X-ray optics. The PSF of NuSTAR's telescope A is shown in Fig.2.5, which has been produced during an observation of the binary black hole GRS 1915+105, which is considered to be a suitable bright point source.

As a result of this measurement, the half of the X-ray photons is enclosed in a diameter of 58″ (half-power diameter). The center of the PSF for detector B is slightly shifted (~ 2″). Note, telescope B also has a slightly higher amplitude of its PSF.

The behaviour of the spectral resolution is the following. It is constant from 3 up to ~50 keV and found to be about 0.4 keV (FWHM), whereas above 50 keV it worsens to a

Table 2.2: Key parameters of the NuSTAR telescopes.

Parameter	Value
Focal length	10.14 m
Pixel size	0.6 mm ($12''.3$)
No. of mirrors	133
Energy range	3-79 keV
Energy resolution (FWHM) at 10 keV	0.4 keV
Energy resolution (FWHM) at 68 keV	0.9 keV
Angular resolution (HPD)[a]	$58''$
Angular resolution (FWHM)[b]	$18''$
Field of view at 10 keV	$10'$
Field of view at 68 keV	$6'$
Relative time resolution	$2\mu s$
Processing time	2.5 ms

[a] Half-power diameter.
[b] Full width at half maximum.
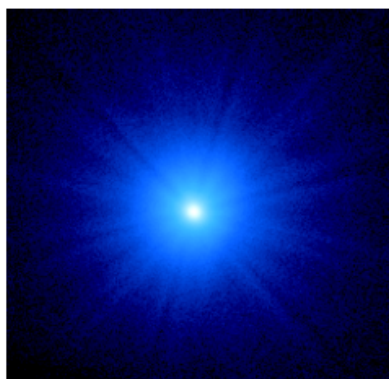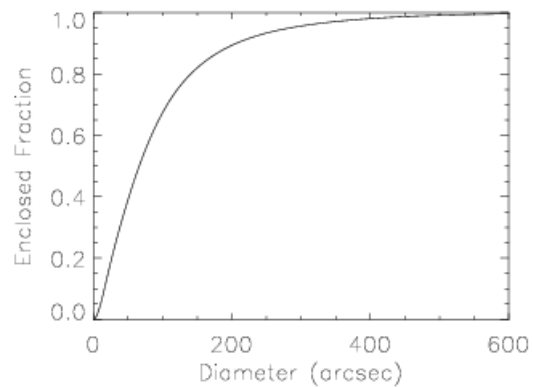
(a)   (b)

Figure 2.5: Panel (a) is an image of GRS 1915+105, used as a point source to measure the on-axis PSF of NuSTAR's detector A. Panel (b) shows the dependence of encircled energy on the diameter of the extraction region. Source: Harrison et al. (2013).

value of about 1.0 keV (FWHM) at the high energy boundary of the energy range. This behaviour is resulted from the electronic noise below 50 keV and charge trapping effects above this energy.

Although the accuracy of the photon arrival time is 2 μs, the electronics readout process takes 2.5 ms, thus resulting in the dead-time effect, which limits the search for features on millisecond timescales.

Because of the almost equatorial orbit, the NuSTAR background is relatively stable compared with missions operating in orbits with higher inclinations. Nevertheless, the NuSTAR background exhibits variations associated with changing geomagnetic latitude, which is, however, not relevant for the observations (more than an orbit cycle) because of averaging of these variations. Below ~10 keV the NuSTAR background is mostly determined by diffuse cosmic emission, whereas at higher energies the albedo from Earth and fluorescence lines arisen in the CsI shield as well as other internal activation lines make the main contribution.

2.1.5   Software and data reduction

To produce high-level data such as calibrated and cleaned event files, light curves, spectra, images, etc., which are then analyzed, the NuSTAR data analysis software (NuSTARDAS[1]) is provided as part of the HEASoft[2] software, distributed by HEASARC[3]. NuSTAR input and output files are in FITS format and fully compatible with FITS standard approved by the NASA/GSFC Office of Guest Investigator Programs to be analyzed using any utility from HEASoft.

The NuSTAR software is divided into several modules according to the LInux way to be used, i.e., each module is dedicated to a single task. It is however available to execute some of these modules together by running two main scripts, named "nupipeline" and "nuproducts", specifying appropriate parameters. The NuSTAR data reduction process consists of three main steps. The first is data calibration, including the event energy correction, the inspection for bad pixels, the coordinates transformation, etc. The input for this step is the FITS-formatted telemetry files. At the second stage filtering of the files from the first stage is performed. And finally the output of the third stage is scientific data, such as light curves, spectra, sky images and response files.

Here is an example of a concrete usage of the NuSTAR software to produce scientific data from telemetry ones. Firstly, data are retrieved using the search form of the HEASARC data archive[4]. The necessary input of the first step of the data reduction is the unfiltered event files (_uf.evt) and some other telemetry data. The "nupipeline" script, however, finds all needed files automatically, so only the input and output directories, the observation id and the mode of reduction have to be specified. For example.

```
nupipeline indir=10202002002 outdir=10202002002/out
steminputs=nu10202002002 obsmode=SCIENCE
```

returns calibrated and filtered event files and other necessary files for the both NuSTAR detector modules, which then can be used to produce the scientific products. The param-

---

[1] https://heasarc.gsfc.nasa.gov/docs/nustar/analysis/

[2] https://heasarc.gsfc.nasa.gov/docs/software/lheasoft/

[3] https://heasarc.gsfc.nasa.gov

[4] https://heasarc.gsfc.nasa.gov/cgi-bin/W3Browse/w3browse.pl

eter `steminputs` indicates the prefix used for all output files.

The next step is creating of the high-level scientific products by executing the "nuproducts" script. In the present work, only point-like sources are considered, so the simplest case of the extraction of those sources are given. First of all, source and background extraction regions have to be selected using, for example, the utility `ds9`[5]. Circular, elliptical and annual source extraction regions are supported. If the source is not too bright, the background is usually selected to be extracted from the darkest area on the same chip. Otherwise, the background can be scaled from deep survey fields.

The most general command to produce the whole set of high-level scientific data is

```
nuproducts indir=10202002002/out outdir=10202002002/products
instrument=FPMA steminputs=nu10012001002
srcregionfile=source.reg bkgregionfile=background.reg.
```

Note that each detector module is explicitly specified. If some scientific data do not need to be created, there is an option to pass `NONE` for these parameters. For example, the command

```
nuproducts indir=10202002002/out outdir=10202002002/products
instrument=FPMA steminputs=nu10012001002
srcregionfile=source.reg bkgregionfile=background.reg
lcfile=NONE bkglcfile=NONE imagefile=NONE
```

generates a source energy spectrum in the products directory as well as an ancillary response (ARF) and a response Matrix (RMF) files.

The barycenter correction, a crucial procedure for timing analysis, is available through adding the following parameters

```
barycorr=yes srcra_barycorr=254.45754 srcdec_barycorr=35.34233
orbitfile=10202002002/auxil/nu10202002002_orb.fits,
```

where `srcra_barycorr` and `srcdec_barycorr` are the celestial coordinates of the source. The additional argument `cleanup=no` leaves the cleaned barycenter corrected event file, otherwise it is deleted after the termination of the `nuproducts` script.

If the high-level scientific data products need to be analyzed in specific time intervals, the user can pass a so-called "Good Time Interval" FITS-formatted file, which contains a user defined temporal filter, through the `usrgtifile` argument when the `nuproducts` script is executed. It might be useful when performing a phase-resolved or a kind of timing analysis.

The scientific data products can also be created in a user defined energy range. This is achieved by providing the first and last energy channel through the parameters `pilow` and `pihigh`. By default, the products are created in the 35-1909 PI channel range, which corresponds to the 3-78 keV energy range.

Although the XSELECT multi-mission software package can be used to extract source and background light curves and energy spectra, it is strongly recommend to use the `nuproducts` script because it automatically runs also some other tasks that make all necessary corrections.

A more comprehensive guide is available on the NuSTARDAS page.

---

[5]http://ds9.si.edu/site/Home.html

2.2 Pulse-amplitude-resolved technique

The data analysis of the present work is based on the *pulse-flux-resolved* (or *pulse-amplitude-resolved*) technique.

The idea of this method is to generate the source spectrum as a function of the total number of counts (or events, which is the same in the context of this chapter) in pulse profile. In fact, this method is a modification of the standard phase-resolved spectroscopy. While in the phase-resolved spectroscopy, we produce the spectrum of the counts that fall into the same phase interval in every pulse, in the pulse-flux-resolved technique only the pulses with a "similar" total number of counts (amplitude) are considered. The "similarity" is in terms of the same quantile of the pulse height distribution. In other words, a distribution of pulses over total number of counts is built, which is then divided into a few parts, keeping the same number of counts in each, and finally the pulses from each part are used to produce a spectrum. As a result, we obtain as many spectra as many parts in the distribution.

In the case of the NuSTAR data, the procedure is the following. A barycenter corrected event file or/and the corresponding light curve should be produced. The light curve is necessary if the source is so bright ($\gtrsim 100\,\mathrm{counts\,s^{-1}}$) that the dead-time effect has to be taken into account, since the event file is not corrected for dead-time. The correction for the binary motion should also be applied to the light curve as well as to the event file. To do this, the actual orbit ephemerides should be used, though if the pulse period is relatively large (in the order of ten of seconds or more, as in the case of V0332+53), the binary motion could be neglected. The binary motion correction is done by using an IDL[6] script based on `binarycor.pro` task from the IDL astro-package, written at the Tuebingen Institute for Astronomy and Astrophysics (IAAT).

First, the `fsearch` and `efold` tasks from the HEASoft package are used to find an appropriate pulse period and to produce a pulse profile, respectively. To be sure that selected counts belong to the same pulse phase to within 0.1 phase, the precision of the pulse period should apparently be $0.1\,P_{\mathrm{spin}}/T_{\mathrm{obs}}$, where P_{spin} is the pulse period and T_{obs} is the on-source time. After producing the pulse profile, it should be specified where the phase zero is. For our purpose, the phase zero is usually chosen at the minimum of the pulse profile. Then, using the `efold` task, the epoch that corresponds to the phase zero is selected. Looking at the pulse profile, a pulse phase interval is defined, in which counts will be collected. In the present work the brightest part of the pulse profile is selected for the analysis.

Second, the phase of every event from the event file is computed with respect to the zero-phase epoch. For each pulse, the events that fall into the specified phase interval are collected and the total number of counts within this interval is calculated. Since the data of the both NuSTAR's detectors are involved in the analysis, it has to be controlled that only pulses present in both the FPMA and FPMB modules are considered. The distribution of these numbers of counts is built, which is then compared to the Poisson distribution with the same mean value. If the obtained distribution is wider than the Poisson distribution, further analysis can be proceeded, namely the distribution is divided into a few parts, and for each part the spectrum is produced. Otherwise, the procedure should be terminated because the pulse height variability is statistical fluctuations. In addition to the number of

---

[6]http://www.harrisgeospatial.com/SoftwareTechnology/IDL.aspx

collected counts, for each pulse, the indices of the first and last count of the interval are also saved. If the source flux is sufficiently high (i.e., $\gtrsim 100\,\mathrm{counts\,s^{-1}}$), the total number of counts is estimated from the light curve.

Third, GTI-files are generated separately for each of the detectors. Note, this step is carried out for each part of the distribution. Since a GTI-file is passed as a parameter when starting `nuproducts` script, the time intervals in the GTI-file must be in the time system of the original event file, which is uncorrected for the Earth and binary motions. However, for each pulse, the time boundaries of the specified phase interval are in the time system of the corrected event file, and to obtain them in the time system of the original event file, the inverse time transformation should be performed, which is not trivial. To avoid this problem, we use the information about indices of the first and last event of the phase interval in each pulse. Since these indices both in the corrected event file and uncorrected event file are the same, we can find the time boundaries of the phase interval in the time system of the original uncorrected event file simply by looking at the indices. Here we assume that the first and last events of the phase interval in each pulse determine the time boundaries. Technically, it is not so, but since each pulse contains hundreds of events, the error in the boundary times determination related to this assumption is neglected. The pulse phase boundary times set the good time intervals included the GTI-file, which is used to produce the spectrum. The number of GTI-files corresponds to the number of parts of the event number distribution.

A straightforward method to check whether the spectrum is derived from the specified phase interval is to mark the interval borders for each pulse right at the light curve. However, not every source exhibits such sufficient variability and statistics that single pulses can be distinguishable. In this case, the verification can be carried out by means of dividing of the pulse profile into 10-15 phase intervals and calculation of the total numbers of counts in these intervals. The dependence of these numbers on pulse phase should resemble the pulse profile. If so, the spectra generating procedure was correct and the obtained spectra indeed correspond to a specified pulse phase interval.

The procedure and visualization were mainly performed using the Python 2.7 programming language involving such libraries as PyFITS[7], NumPy, SciPy[8], Matplotlib[9], and Sherpa[10]. In addition to Python scripts, the spectral analysis was carried out using XSPEC[11] package.

---

[7]https://pythonhosted.org/pyfits/

[8]https://docs.scipy.org/doc/

[9]https://matplotlib.org

[10]http://cxc.cfa.harvard.edu/contrib/sherpa/

[11]https://heasarc.gsfc.nasa.gov/xanadu/xspec/

3. Observations of Cep X-4

3.1 Introduction

The accreting pulsar Cepheus X-4 (Cep X-4) was discovered in 1972 with the Orbiting Solar Observatory - 7 (Ulmer et al. 1973) and re-discovered in 1988 with *Ginga* as GS 2138+56 during a one-month-long X-ray outburst (Makino & GINGA Team 1988). During the 1988 outburst, pulsations with a period of 66.2 s were detected (Koyama et al. 1991), which established the nature of the source as an accreting magnetized neutron star. Observations of this outburst yielded the discovery of a cyclotron line at around 30 keV (Mihara et al. 1991).

During observations of the 1993 outburst, the accuracy of the X-ray source position was improved, allowing Roche et al. (1997) to propose a Be spectral class star as the optical counterpart of the neutron star. This identification was confirmed later by Bonnet-Bidaud & Mouchet (1998), who also estimated the distance to the source to be 3.8 ± 0.6 kpc. However, the distance according the latest Gaia release is 20 ± 8 kpc, which does not seem right because other authors give values between 3 and 9 kpc, depending on method (Treuz et al. 2018).

During the 2002 outburst, the CRSF energy was re-measured with RXTE to be at $30.7^{+1.8}_{-1.9}$ keV without a significant dependence on X-ray luminosity, although the continuum was reported to become harder with increasing luminosity (McBride et al. 2007). The source went into outburst again in 2014 and was observed with the Nuclear Spectroscopic Telescope Array (NuSTAR) by the two detectors FPMA and FPMB. Two NuSTAR observations of Cep X-4 were performed during this outburst (Fig. 4.1). The average fluxes in these observations differ by a factor of about 3.5, providing an opportunity to investigate the spectrum-luminosity variability. The CRSF energy was found to be different between the two observations: the lower cyclotron line energy corresponds to the fainter observation, indicating a possible positive correlation between the CRSF energy and luminosity, although with only two data points (Fürst et al. 2015). Fürst et al. (2015) also reported a distorted cyclotron line profile in the source. However, it should be noted that the line shape might depend on the selected continuum model.

3.2 Observations and data reduction

NuSTAR observed the source twice during the 2014 outburst (Fig. 3.1), on June 18-19, referred to as observation I in the following, and on July 1-2, referred to as observation II. The first observation is near the outburst maximum with a total on-source time of 47.9 ks (ObsID 80002016002, MJD 56826.92-56827.84). The second observation was performed
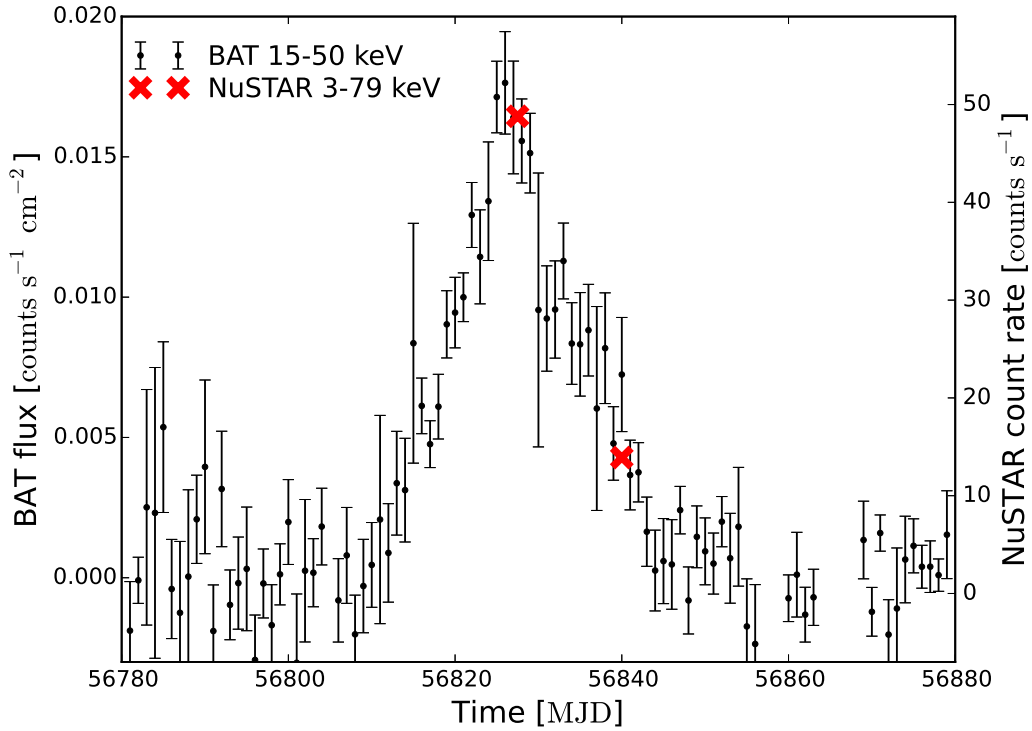
Figure 3.1: Light curve of the 2014 outburst of Cep X-4 taken with Swift/BAT (black data points). The NuSTAR observations analysed here are indicated with red crosses.

at the decay of the outburst with a total on-source time of 45.2 ks (ObsID 80002016004, MJD 56839.43-56840.31). Figure 4.1 also represents the Swift/BAT observations of the outburst[1].

For our pulse-to-pulse analysis described in Sect. 3.3.2, all source spectra of the two NuSTAR detectors FPMA and FPMB are extracted from a circular region with a radius of 80" on the detector plane. The background spectra are extracted from a circular region of the same radius at the periphery of the NuSTAR field of view, similarly to Fürst et al. (2015). The same extraction regions were initially also used for our pulse-averaged spectra. For a detailed investigation of the possible cyclotron harmonic feature around 55 keV, we used modified extraction regions as described in Sect. 3.3.1.

The data processing was performed using the standard `nupipeline` and `nuproducts` utilities and XSPEC[2] v12.9 as part of HEASOFT[3] 6.18.
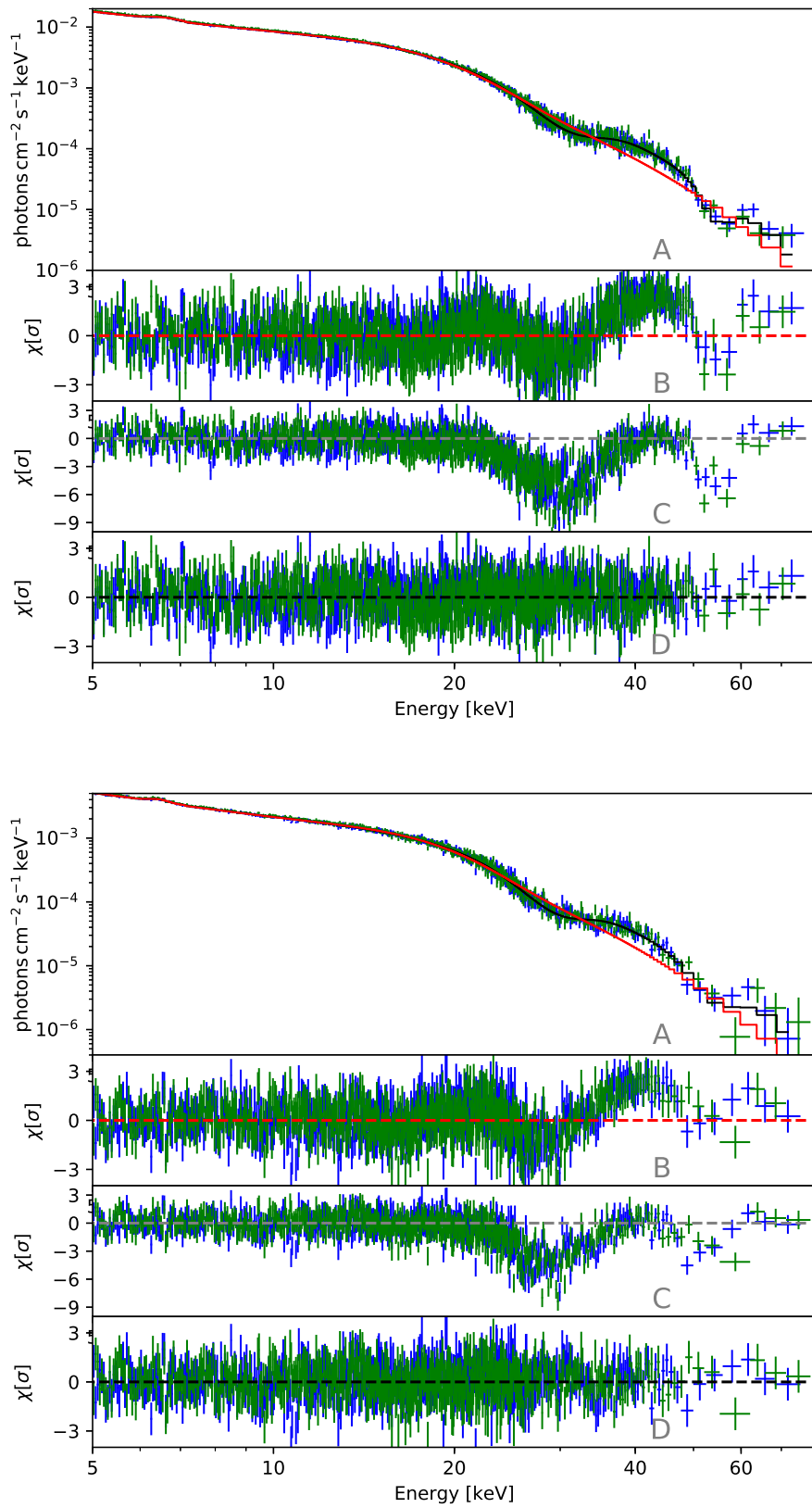
Figure 3.2: Unfolded NuSTAR spectra of obs. I (top) and obs. II (bottom). A detailed explanation of the figure is given in the text.

3.3 Spectral analysis and results

3.3.1 Flux-averaged spectroscopy

The spectral continuum of highly magnetised accreting neutron stars is typically described with phenomenological power law models with an exponential cutoff at higher energies (e.g. Coburn et al. 2002). Some models, however, include a detailed description of the physics of the polar emitting region (Wang & Frank 1981; Becker & Wolff 2007; Farinelli et al. 2012, 2016; Ceccobello et al. 2014; Wolff et al. 2016). These physical models have been already successfully applied in some cases (Ferrigno et al. 2009; Farinelli et al. 2016; Wolff et al. 2016). However, assumptions and approaches used in these models are still being tested and revised. Since in this work we focused on the behaviour of the CRSF centroid energy and the general properties of the continuum, like its hardness, it is sufficient to describe the spectra using traditional phenomenological models, which also allows us to compare our results with the previous works.

McBride et al. (2007) showed that the continuum of the Cep X-4 pulse-averaged spectrum between 3.5 and 70 keV is described well by a power-law with index Γ (`powlaw` in XSPEC), modified by a Fermi-Dirac cut-off (`fdcut`, Tanaka 1986)

$$\text{Fdcut}(E) \propto E^{-\Gamma} \frac{1}{1 + \exp\left(\frac{E - E_{\text{cut}}}{E_{\text{fold}}}\right)}, \tag{3.1}$$

where E_{cut} and E_{fold} are the cut-off and folding energies, which characterized the Fermi-Dirac cut-off. To describe the continuum, an additional component is required: a wide additive Gaussian emission line

$$F(E) = \frac{A}{\sigma \sqrt{2\pi}} \exp \frac{-(E - E_{\text{add}})^2}{2\sigma^2}, \tag{3.2}$$

at around E_{add}=14 keV to account for a bump-like feature in the residuals between 8 and 20 keV. A is the amplitude in total photons s^{-1} cm^{-2} in the line, σ is the line width and E_0 is the centroid energy.

A broad line-like feature like this and at these energies, known as the 10 keV feature, is reported for some other accreting pulsars observed with RXTE, *Ginga*, BeppoSAX, and other missions (Coburn et al. 2002). To reproduce the 10 keV feature in the Cep X-4 spectrum, we can use not only a broad emission line, but also an absorption line or a combination of the two. The additional wide Gaussian emission line does not correspond to a separate physical component. The 10 keV feature thus apparently reflects limitations of the simple phenomenological function used to describe the continuum of the high-quality NuSTAR spectrum of Cep X-4.

We describe the fundamental CRSF, clearly seen in the NuSTAR spectra at around 30 keV (Fig. 3.2), as a multiplicative absorption line with a Gaussian optical depth profile (`gabs` in XSPEC)

$$M(E) = \exp\left(-\frac{d}{\sigma \sqrt{2\pi}}\right) \exp \frac{-(E - E_{\text{cyc}})^2}{2\sigma^2}, \tag{3.3}$$

---

[1]http://swift.gsfc.nasa.gov/results/transients/weak/Ginga2138p56/
[2]https://heasarc.gsfc.nasa.gov/xanadu/xspec/
[3]http://heasarc.nasa.gov/lheasoft/

where E_{cyc} is the cyclotron line energy and σ is the line width, which is related to the optical depth $\tau = d/(\sigma \sqrt{2\pi})$.

In addition to the fundamental CRSF, we found its harmonic at 55 keV, presented in both observations. To model the harmonic, we also used a multiplicative absorption line with a Gaussian optical depth profile as for the fundamental feature.

The Fe K_α fluorescent line at around 6.4 keV is modelled as an additive Gaussian emission line with the shape described by Eq.3.2. We also take photoelectric absorption into account in the soft part of the spectra using the `phabs` model in XSPEC with photoelectric cross-sections from Verner et al. (1996) and element abundances from Wilms et al. (2000).

The described spectra with the best-fit model (black line) are shown on panel A of Fig. 3.2. The red line indicates the continuum model without cyclotron lines. The blue and green data points correspond to FPMA and FPMB, respectively. Panel B shows the residuals of the best fit for a model without cyclotron lines (red line). Residuals to the best-fit model (black line in panel A) are shown in panel D. Panel C shows residuals to the model setting the strengths of the the two cyclotron lines to zero, but leaving the other parameters at their best-fit values obtained using the model with the lines (in order to illustrate the contribution of the lines to the continuum). The best-fit parameters of the model with the lines are listed in Table 3.1.

Panels B of Fig. 3.2 show sharp residuals around 55 keV. These residuals are present in the spectra of the the two NuSTAR observations in the data of FPMA and FPMB. To describe this line-like feature as well as possible and to clarify whether the feature could be a harmonic of the CRSF, we analysed the spectrum in the energy range between 50 and 70 keV. First, we used background spectra extracted from different areas on the detector plane and found that the feature does not disappear. The dependence of the effective area on energy does not contain any peculiarities around 55 keV either. Second, we performed an analysis searching for an optimal size of the source extraction region at which the signal-to-noise ratio has a maximal value in the energy range of 50-70 keV. We found that the optimal size lies between 50″ and 70″ and extracted the source spectrum from a 60″ radius region. Background spectra were extracted from a circular region of 160″ radius at the periphery of the NuSTAR field of view. This adjustment of the extraction region does not significantly change the best-fit parameters of the continuum and of the fundamental cyclotron line. We then built the source spectrum describing the feature with the `gabs` model (Fig. 3.2). We therefore conclude that the feature at around 55 keV in the Cep X-4 spectrum is indeed the first harmonic of the CRSF. A very similar feature is present in the Suzaku spectrum of Cep X-4 taken during observations of the same outburst. Jaisawal & Naik (2015) analysed the Suzaku data and interpreted the feature as the first harmonic.

Panels C of Fig. 3.2 demonstrate the deviation of the true spectrum from the continuum. Both lines are well localized and do not dominate the continuum, in contrast to the case of 4U 0115+63, for example, where inadequately modelled cyclotron lines could fully distort the continuum, as illustrated in Fig. 8 of Müller et al. (2013b) for instance.

The applied model can therefore be written as

$$\text{ABS} \times (\text{FDCUT} \times \text{CRSF} \times \text{CRSF}_h + \text{ADD} + \text{Fe}), \qquad (3.4)$$

where ABS is the photoelectric absorption (`phabs`), FDCUT is the `fdcut` function, ADD is the additional emission Gaussian line in the continuum, the CRSF and CRSF$_h$ are `gabs`

Table 3.1: Parameters of the best-fit models of the pulse-averaged spectra represented in Fig. 3.2 in the energy range of 3-79 keV from a circular region with a radius of 60". The indicated uncertainties are at 1σ (68%) confidence level.

Parameter	Observation I	Observation II
N_H [10^{22} cm^{-2}]	$2.6^{+0.3}_{-0.3}$	$2.8^{+0.3}_{-0.4}$
Γ	$1.29^{+0.07}_{-0.06}$	$1.33^{+0.06}_{-0.06}$
A[a]	$0.21^{+0.04}_{-0.03}$	$6.6^{+0.7}_{-0.6} \times 10^{-2}$
E_{cut} [keV]	13^{+4}_{-6}	13 (fixed)
E_{fold} [keV]	$10.3^{+1.0}_{-0.9}$	$10.5^{+0.5}_{-0.5}$
E_{add}[b] [keV]	$11.5^{+0.4}_{-0.4}$	$12.9^{+0.5}_{-0.5}$
σ_{add} [keV]	$5.9^{+0.3}_{-0.3}$	$5.7^{+0.4}_{-0.4}$
A_{add}[a]	$4.5^{+0.7}_{-0.7} \times 10^{-2}$	$7.3^{+1.3}_{-1.2} \times 10^{-3}$
$E_{Fe\,K_\alpha}$ [keV]	$6.53^{+0.02}_{-0.02}$	$6.42^{+0.03}_{-0.03}$
$\sigma_{Fe\,K_\alpha}$ [keV]	$0.35^{+0.04}_{-0.03}$	$0.22^{+0.05}_{-0.05}$
A_{Fe}[a]	$1.04^{+0.08}_{-0.07} \times 10^{-3}$	$1.9^{+0.3}_{-0.3} \times 10^{-4}$
E_{CRSF} [keV]	$30.6^{+0.2}_{-0.3}$	$29.0^{+0.3}_{-0.2}$
σ_{CRSF} [keV]	$3.9^{+0.2}_{-0.2}$	$3.8^{+0.2}_{-0.2}$
d_{CRSF}[c]	$6.6^{+0.9}_{-0.8}$	$7.0^{+0.8}_{-0.6}$
E^h_{CRSF}[d] [keV]	$54.8^{+0.5}_{-0.5}$	$54.0^{+1.5}_{-1.4}$
σ^h_{CRSF} [keV]	$3.2^{+0.5}_{-0.4}$	$4.4^{+1.1}_{-0.9}$
d^h_{CRSF}	$9.6^{+2.0}_{-1.8}$	$9.2^{+3.3}_{-2.9}$
C_{FPMB}[e]	1.0374 ± 0.0013	1.024 ± 0.002
Flux$_{3-78\,keV}$[f]	26.9 ± 0.1	7.10 ± 0.02
χ^2_{red}/d.o.f.	1.06/1611	1.05/1320

[a] In photons s^{-1} cm^{-2} keV^{-1} at 1 keV.

[b] The parameters of the additional wide Gaussian emission line are denoted by the "add" subscript.

[c] Optical depth $\tau = d/(\sigma\sqrt{2\pi})$.

[d] The "h" superscript marks the harmonic line parameters.

[e] A cross-calibration constant for FPMB relative to FPMA.

[f] Unabsorbed flux in 10^{-10} erg s^{-1} cm^{-2}.

models for the fundamental CRSF and the harmonic, respectively, and Fe is the iron K_α complex modelled as a Gaussian emission line. The best-fit parameters of this model for the pulse-phase averaged spectra for the two NuSTAR observations are listed in Table 3.1. Owing to lower statistics, the spectra of observation II do not allow us to constrain E_{cut}. Since we prefer to use the same spectral model in both observations, we fixed E_{cut} in observation II to the best-fit value we obtained in observation I.

3.3.2 Flux-resolved spectroscopy

To investigate the variation of spectral parameters as a function of he X-ray luminosity within individual observations, we applied the pulse-to-pulse technique elaborated in Klochkov et al. (2011) and Müller et al. (2013a). This method is aimed at investigating the spectrum-luminosity dependence using the pulse-to-pulse variability that is generally exhibited by accreting pulsars (Staubert et al. 1980; Frontera et al. 1985; Tsygankov et al. 2007).

Our pulse-to-pulse analysis includes the following stages. First, all photon arrival times are barycentered using the DE-200 solar system ephemeris. We measured pulse periods of 66.3352 ± 0.0003 and of 66.3336 ± 0.0002 s for observation I and observation II, respectively. These values are used to obtain the pulse profiles shown in Fig. 3.3. We then specify a phase interval containing the brightest part of the pulse profile, which is referred to as *pulse* (shaded areas in Fig. 3.3). To characterise the brightness of the pulse, we define the *pulse amplitude* as the total number of counts in the entire NuSTAR energy band (3–79 keV) within the specified phase interval of an individual pulsation cycle divided by the width of this interval. The number of counts in a single pulse is insufficient to extract a meaningful spectrum, therefore we group pulses with similar amplitudes together, similarly to Klochkov et al. (2011). For this purpose, we construct frequency distributions of pulse amplitudes, which are shown in Fig. 3.4. Although the average flux within each observation does not change much, the distribution clearly covers a dynamical range of a factor of two in amplitude, indicating a strong intrinsic pulse-to-pulse variability of the source. We then split the distribution into four bins such that approximately the same number of events are in each bin (the dashed vertical lines in Fig. 3.4). The width of the bins is wider than the statistical fluctuation (variance) of pulse amplitudes, which guarantees that the observed variability reflects the intrinsic flux changes. Finally, we extract a broadband spectrum for each pulse amplitude bin.

Since the number of photons in each pulse amplitude bin spectrum is lower than 25% of the pulse-averaged spectrum, the harmonic becomes insignificant, especially in observation II. Since our purpose in this part was to investigate the variability of the energy of the fundamental CRSF, we extracted spectra between 3 and 48 keV to eliminate any possible influence of the residuals around the harmonic energy on the fundamental line. Therefore we here use the same model as in the analysis of the pulse-averaged spectrum described above, except for the harmonic component, and we do not fix the cut-off E_{cut} energy in observation II.

As mentioned above, to describe the continuum successfully, we introduced an additional component to model the 10 keV feature. To ensure that this component did not influence the determination of the CRSF centroid energy (see e.g. Boldin et al. 2013), we constructed the contour plots for the CRSF energy versus the parameters of the 10 keV
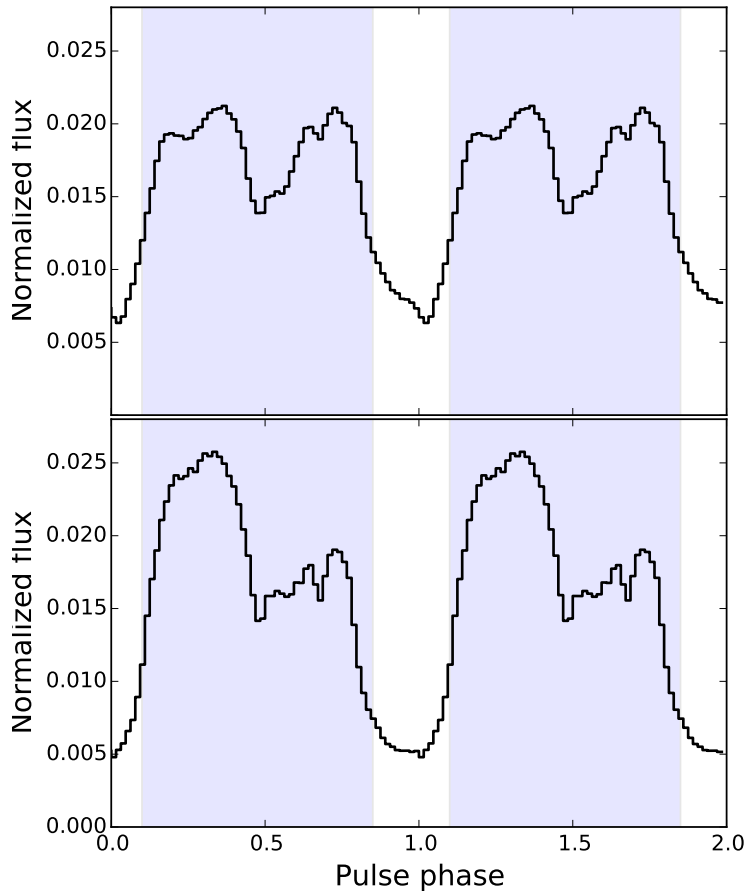
Figure 3.3: NuSTAR pulse profiles in the 3-79 keV energy range from observations I (top) and II (bottom). The shaded areas indicate the phase interval considered for the pulse-to-pulse analysis. The part of the profile within the interval is referred to as *pulse* (see text).

component (Fig. 3.5). The confidence regions in the plots do not indicate any significant correlation between the parameters, reflecting that the reported variations in the line energy are not associated with possible variations in the 10 keV feature.

From a circular region with a radius of 80″ (see Sect. 3.2), we extracted four spectra per detector for each observation, corresponding to the four pulse amplitude bins. In our fits, we left the relative normalisation of the two detectors free because there is a slight difference in their calibration. The model parameters of the spectra of the amplitude bins were coupled (bound) except for the parameters whose behaviour as a function of pulse amplitude was investigated. The investigated parameters are the energy of the fundamental cyclotron line E_{CRSF} and the power-law index Γ. The continuum hardness HR considered below is defined as the ratio of the flux in the 8-12 keV range to the flux in the 4-6 keV range. All other parameters (except for the relative normalization, as mentioned above) were coupled. We verified that the coupled parameters do not show any noticeable variability with pulse amplitude when they are left free.
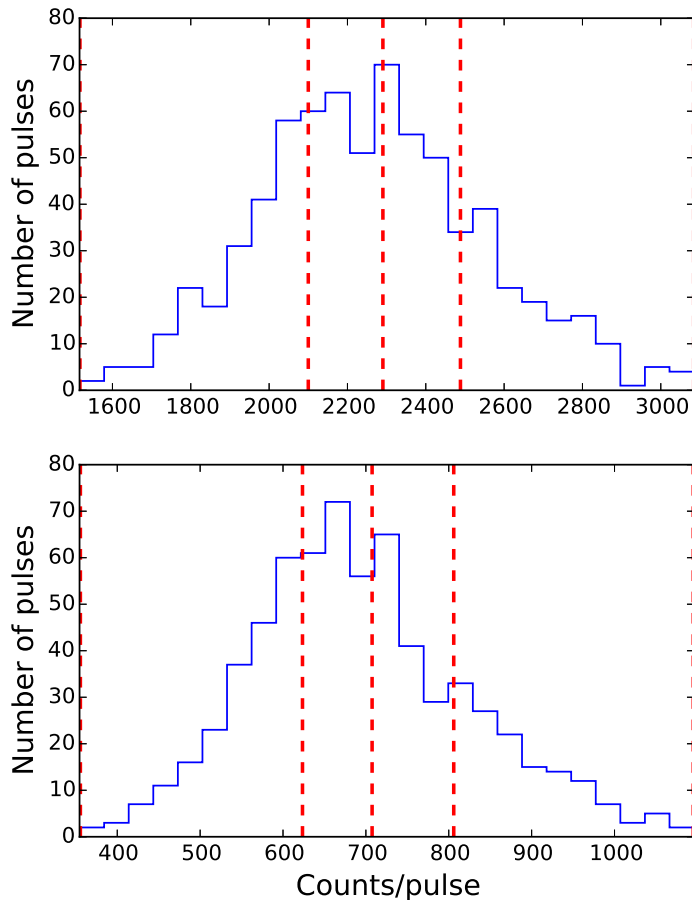
Figure 3.4: Distributions of counts in individual pulses (representing the pulse amplitudes) for observations I (top) and II (bottom). The red dashed lines indicate the boundaries of the amplitude bins we used to extract amplitude-resolved spectra. In each distribution, the total number of counts is evenly distributed among the bins.

The dependence of the fundamental CRSF centroid energy and of the continuum hardness ratio on pulse amplitude is shown in Fig. 3.6. The bottom axis represents the bin-averaged count rate in the 3-79 keV range, while the top axis represents the corresponding X-ray luminosity in the same energy band for the assumed distance of 3.8 kpc. The vertical and horizontal error bars on the data points in Fig. 3.6 correspond to 1σ uncertainties.

Since the emission of the pulsar is not isotropic, the flux in the pulse cannot be converted into luminosity by simply multiplying by $4\pi D$, where D is the source distance. Therefore we first calculated the pulse-averaged flux using the unfolded spectrum of each observation. This flux may to some extend be considered as the source flux averaged over the total solid angle and can therefore be converted into luminosity in the usual way. Using the pulse averaged flux, we calculated the average luminosity for each of the two observations. We then assumed that the relative changes in the pulse amplitude with respect to the average pulse amplitude in an observation are equal to the relative change in the luminosity with respect to the average luminosity in this observation. Under this
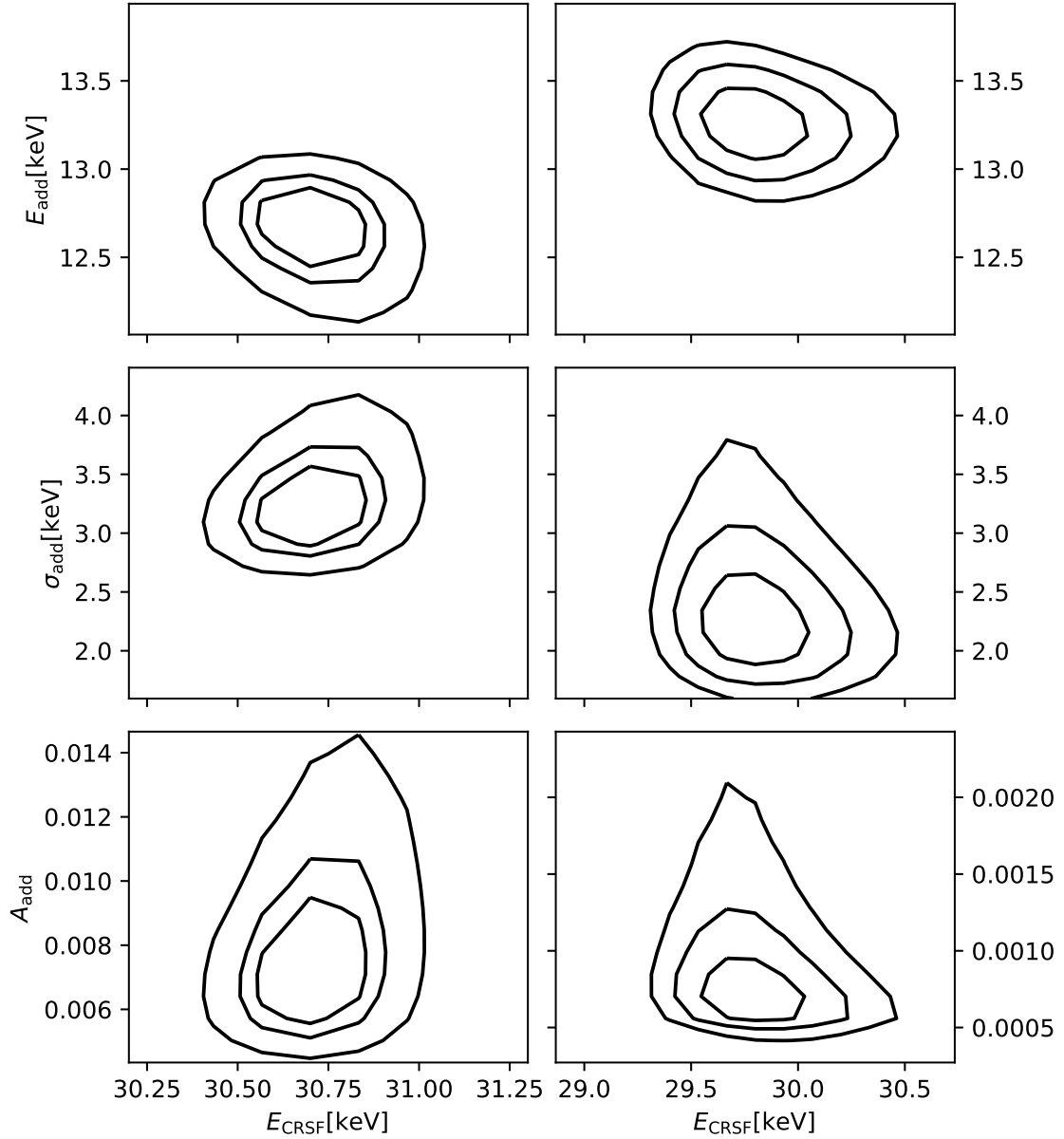
Figure 3.5: Confidence regions to investigate possible intrinsic correlation between the CRSF centroid energy E_{CRSF} and the parameters of the Gaussian line describing the 10 keV feature in the continuum. The left and right columns show results for observations I and II, respectively. The contours correspond to the 1σ, 2σ, and 3σ confidence levels for the two parameters of interest. The colour scale indicates $\Delta\chi^2$: darker areas correspond to lower $\Delta\chi^2$. A_{add} is in photons $s^{-1}\,cm^{-2}\,keV^{-1}$ at 1 keV.

assumption, we calculated the luminosity of each pulse or the average luminosity in each pulse amplitude bin, which is shown on the top axis of Fig. 3.6.

As shown in the top panel of Fig. 3.6, the data reveal a strong positive correlation between the fundamental CRSF energy and the X-ray luminosity. Furthermore, the correlation is present in the data of observation I alone (data points in the top right). Here the differences in luminosity between the data points are caused by pulse-to-pulse variability. The data of observation II alone (data points on the bottom left) have insufficient statistics to claim a correlation.

The common linear fit to all the data points is shown with a solid line and yields a slope of $0.034 \pm 0.002\,\mathrm{keV\,(cts/s)^{-1}}$. This slope is formally consistent with separate linear fits to the data points of the two observations with slopes of 0.043 ± 0.009 and of $0.021 \pm 0.014\,\mathrm{keV\,(cts/s)^{-1}}$ for observations I and II, respectively. The dashed lines mark 1σ cones of the allowed slope ranges from the separate fits of the two observations. We conclude that the E_{CRSF}/L_X dependence is roughly the same in the two observations and between them.

The bottom panel of Fig. 3.6 shows the spectral hardness as a function of pulse amplitude or luminosity. The hardness ratio clearly rises with increasing luminosity from observation II to observation I as well as within each observation. It can also be seen that the dependence is substantially flatter in observation I. Linear fits have slopes of $(2.0 \pm 0.2) \times 10^{-3}$ and of $(9.2 \pm 3.3) \times 10^{-3}\,\mathrm{(cts/s)^{-1}}$ for observations I and II, respectively (dashed lines). The difference in slopes is thus statistically significant.

To ensure the reliability of the dependencies, we fitted the spectrum continuum with an alternative phenomenological model. Specifically, we used a power law with an exponential cut-off

$$\mathrm{Highecut(E)} \propto \begin{cases} E^{-\Gamma} & E \leq E_{\mathrm{cut}} \\ E^{-\Gamma} \exp\left(-\frac{E - E_{\mathrm{cut}}}{E_{\mathrm{fold}}}\right) & E > E_{\mathrm{cut}} \end{cases} \tag{3.5}$$

(White et al. 1983, `highecut` in XSPEC) and an additive emission Gaussian line to flatten the 10 keV feature. We also added a `gabs` component to the continuum to smooth the derivative discontinuity at E_{cut} in this case. The CRSF was also described as a multiplicative absorption line with a Lorentzian optical depth profile (`lorentz` in XSPEC)

$$L(E) = A \frac{\sigma}{2\pi} \frac{1}{(E - E_0)^2 + (\sigma/2)^2}. \tag{3.6}$$

In addition to our model, we thus tested three alternative models: the `highecut * gabs + gauss` model for the continuum with either the `gabs` or the `lorentz` model for the cyclotron line, and the `fdcut+gauss` model for the continuum with the `lorentz` model for the cyclotron line. The iron line was described as an additive emission `gauss` in all models. All the dependencies described above are found to be present in all the alternative models, and all our conclusions remain valid independently of the choice of a specific spectral function.

3.4 Discussion

The aforementioned dependence between the fundamental CRSF energy and the X-ray luminosity, the spectral hardness ratio and the X-ray luminosity in separate observations re-
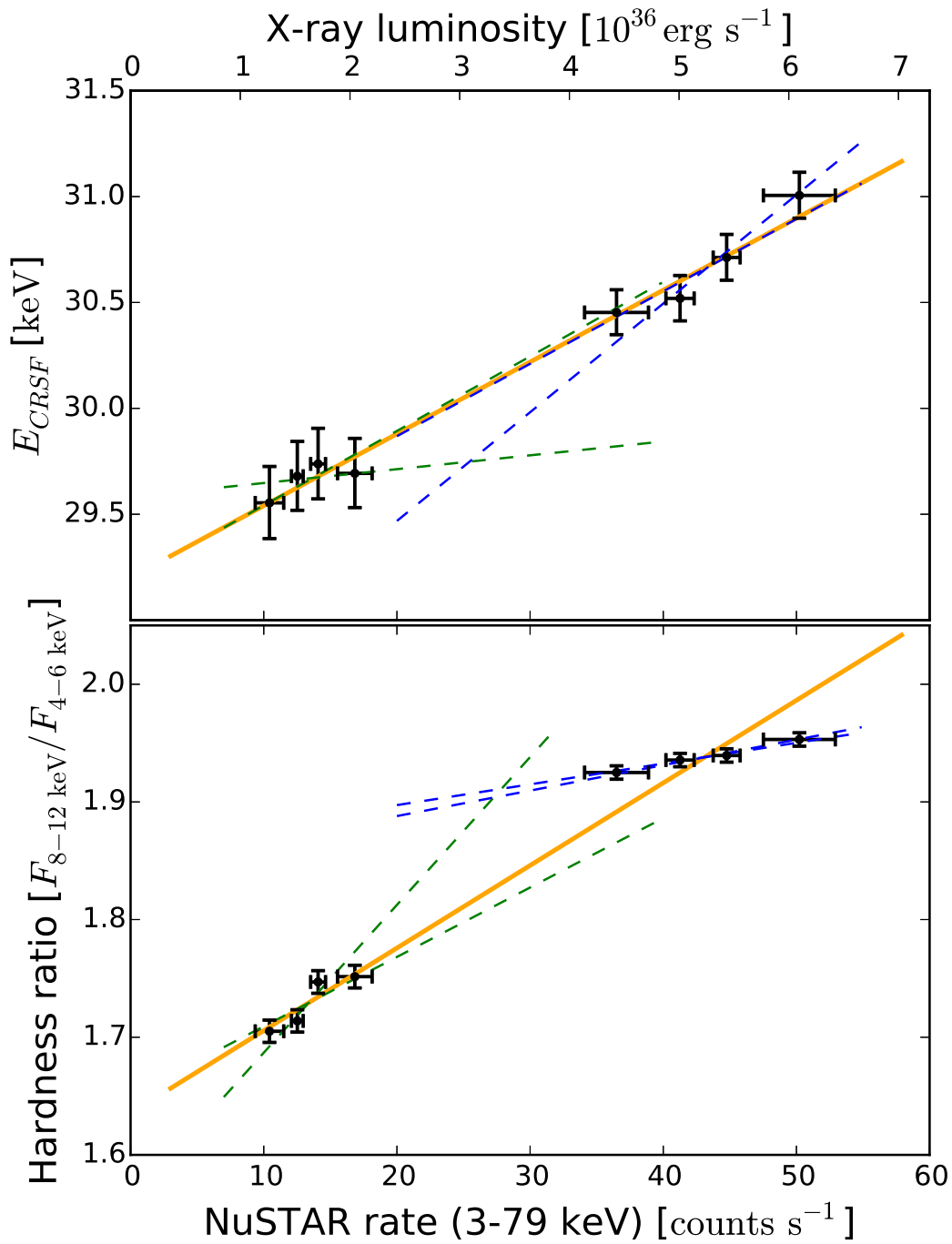
Figure 3.6: Fundamental CRSF centroid energy (top) and the spectral hardness ratio (bottom) of Cep X-4 as a function of pulse amplitude, which is converted to luminosity on the top axis. The orange solid line represents a common linear fit to the data points for the two observations. The dashed lines mark 1σ cones of the allowed slope ranges from the separate fits to the two observations.

sults from the pulse-to-pulse analysis, which is used to describe the intrinsic source pulse-to-pulse variability. For both observations, this dependence is observed on a timescale corresponding to one cycle of X-ray pulsations, that is, on the order of minutes (the pulse period of Cep X-4).

In the case of the $E_{\mathrm{CRSF}}/L_{\mathrm{x}}$ correlation, however, the same linear dependence is observed to be present on both short (a pulse cycle) and long (outburst duration) timescales. We can therefore assume that the physical processes behind the positive $E_{\mathrm{CRSF}}/L_{\mathrm{x}}$ dependence observed in Cep X-4 are linear, in a first approximation, on timescales from a minute to a dozen days, or in other words, the properties of these processes remain constant on these timescales.

In the case of the spectral hardness, on the other hand, such a linearity is not observed. Thus, the shape of the HR/L_{x} dependence is likely to be more complex on longer timescales, while on short timescales it seems to be linear.

As mentioned in Sect. 1.3, positive and negative correlations between the CRSF energy E_{CRSF} and the X-ray luminosity L_{x} are observed in some X-ray pulsars. The critical luminosity $L_{\mathrm{cr}} \sim 10^{37}$ erg s^{-1} that reflects the mass accretion rate $\dot{M}$ is believed to separate accretion regimes that are characterised by different signs of the correlation (Basko & Sunyaev 1976; Staubert et al. 2007; Becker et al. 2012; Mushtukov et al. 2015b). A positive $E_{\mathrm{CRSF}}/L_{\mathrm{x}}$ correlation is observed below L_{cr}, while a negative correlation is observed above it.

Above L_{cr}, the radiation pressure in the polar emitting region of the NS dominates the gas pressure such that the infalling plasma is decelerated mainly through interactions of the plasma electrons with photons. This regime is often referred to as supercritical. The hight of the emitting region, which in this case is believed to have roughly a column-like shape (accretion column), is expected to grow with the mass accretion rate (Davidson 1973; Basko & Sunyaev 1976; Wang & Frank 1981; Burnard et al. 1991; Postnov et al. 2015; Mushtukov et al. 2015a). If the CRSF is formed in a region associated with the accretion column as suggested in Becker et al. (2012), for example, the cyclotron line energy will be anti-correlated with the height of the column. Indeed, the strength of the NS dipole magnetic field decreases with increasing height above the stellar surface and so does the cyclotron line energy, which is proportional to the field strength.

Alternatively, the CRSF might form in the radiation reflected by the NS surface surrounding the accretion column, as suggested by Poutanen et al. (2013). A growth of the column would widen the stellar surface that is illuminated by the radiation from the column, including areas farther away from the magnetic pole where the magnetic field is weaker. As a result, an anti-correlation between the line energy and the accretion rate should be observed.

In accreting pulsars with luminosities below L_{cr}, which are referred to as subcritical sources, the radiation pressure is unimportant compared to gas pressure. In this case, the infalling plasma has to be decelerated through Coulomb collisions, collective plasma effects, or through a collisionless shock that forms above the stellar surface. The following ideas have been proposed in the literature to explain the positive $E_{\mathrm{CRSF}}/L_{\mathrm{x}}$ correlation in the subcritical case. In Staubert et al. (2007) and Becker et al. (2012), the line-forming region was again assumed to be associated with the stopping region such that variations in the height of this region above the stellar surface lead to corresponding changes in the CRSF energy. It was shown that contrary to the supercritical case, the stopping region

approaches the surface with increasing mass accretion rate. Therefore an anti-correlation between the CRSF centroid energy and luminosity is expected. An alternative idea has been elaborated in Mushtukov et al. (2015c), who suggested that the variations in the energy of the cyclotron line are due to the Doppler effect. The dependence of the mean velocity of the infalling matter in the line-forming region on the mass accretion rate is responsible for the positive $E_{\mathrm{CRSF}}/L_{\mathrm{x}}$ correlation in this model.

3.4.1 Collisionless shock model

The idea that a collisionless shock could appear in the infalling matter accreted by the neutron star was suggested by Bisnovatyi-Kogan & Fridman (1969). Furthrer theoretical studies of the accretion onto a neutron star carried out by (Shapiro & Salpeter 1975) and Langer & Rappaport (1982) revealed that a stationary collisionless shock at a certain height above the neutron star surface could exist. This possibility that infalling matter could decelerate in a collisionless shock is so far poorly explored in the case of accreting pulsars, which is why it is considered here. To have a general understanding, how collisionless shocks form in space plasma, please see Appendix A A.

This shock is likely to be the main stopping agent of the accretion flow only when the photon luminosities are low enough for radiation pressure to be unimportant for the accretion flow breaking. Radiation pressure however could play a role in the cyclotron line because of its high optical depth even at low luminosities (Bykov & Krasilshchikov 2004).

This model has recently been used to describe the observed non-linear dependencies of the CRSF parameters on luminosity in another subcritical X-ray pulsar GX 304−1 (Rothschild et al. 2017). Here, this model is being developed in more detail to describe the evolution of the spectral hardness ratio (HR) as well as the energy of the cyclotron line with luminosity.

CRSF energy – luminosity dependence

The height of the collisionless shock forming in the infalling flow near the NS surface is expected to depend on electron density n_{e} as $H_{\mathrm{s}} \propto 1/n_{\mathrm{e}}$ (Shapiro & Salpeter 1975). The electron density $n_{\mathrm{e}} \propto \dot{M}/A$, where $\dot{M}$ is the mass accretion rate and A is the accretion area of the accretion flow on the stellar surface depending on the magnetospheric radius R_{m} as $1/R_{\mathrm{m}}$ in a dipole field approximation. The magnetospheric radius $R_m \propto \dot{M}^{-x}$, where $x = 2/7$ for disc accretion or Bondi quasi-spherical accretion, and $x = 2/11$ for quasi-spherical settling accretion (Shakura et al. 2012), so that $A \propto \dot{M}^x$ and

$$H_{\mathrm{s}} \propto 1/n_{\mathrm{e}} \propto A/\dot{M} \propto \dot{M}^{x-1} \propto \dot{M}^{-\alpha}, \tag{3.7}$$

where $\alpha = 1 - x = 5/7$ for disc accretion or Bondi quasi-spherical accretion, and $\alpha = 9/11$ for quasi-spherical settling accretion. Assuming the disc accretion in Cep X-4, we use $\alpha = 5/7$ in all formulas below.

With increasing mass accreting rate, the height of the collisionless shock thus decreases such that the line-forming region moves towards stronger magnetic fields and the cyclotron line shifts to higher energies. In a dipole field, $E_{\mathrm{CRSF}}(r) \propto B(r) \propto 1/r^3$, and
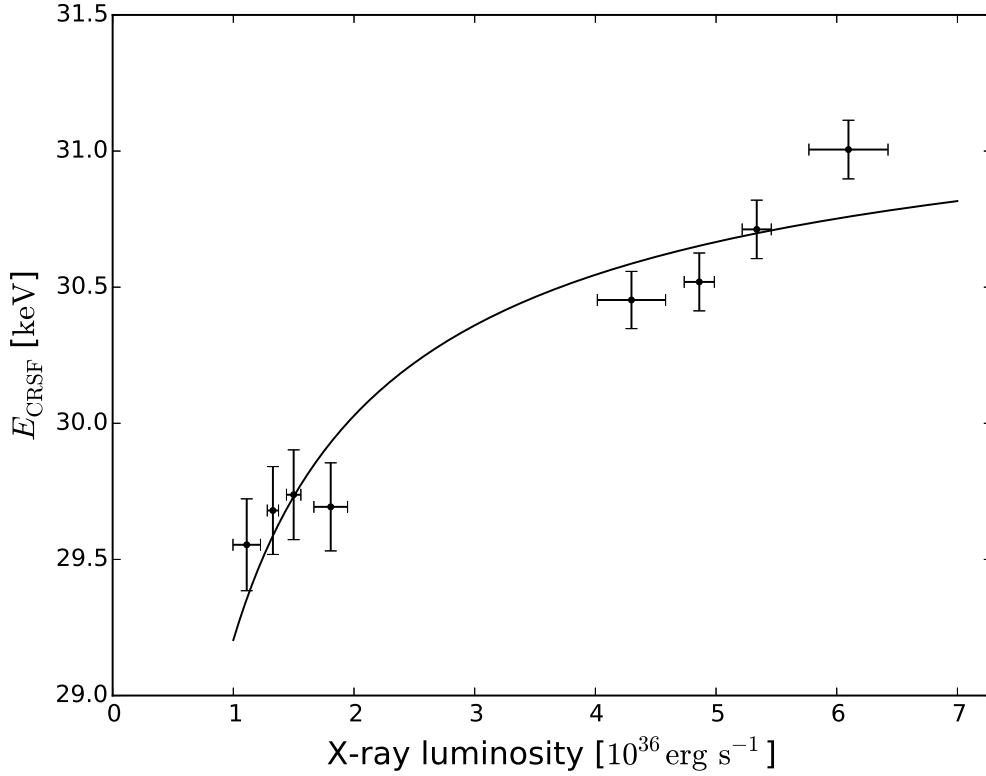
Figure 3.7: Centroid energy of the fundamental cyclotron line in Cep X-4 as a function of X-ray luminosity (data points with 1σ error bars). The solid curve represents a fit using our model assuming a collisionless shock (see text), $\chi^2_{\mathrm{red}}/$d.o.f. = 1.75/7.

considering that $r = R_{\mathrm{NS}} + H_{\mathrm{s}}$, where R_{NS} is the NS radius and H_{s} is a function of accretion rate, we express the energy of the cyclotron line as a function of mass accretion rate:

$$E_{\mathrm{CRSF}}(\dot{M}) = E_0 \left(\frac{R_{\mathrm{NS}}}{H_{\mathrm{s}}(\dot{M}) + R_{\mathrm{NS}}} \right)^3 , \tag{3.8}$$

where E_0 is the cyclotron line energy corresponding to the magnetic field at the NS surface on the magnetic poles. Assuming that the observed X-ray flux F_{x} is directly proportional to the mass accretion rate $\dot{M}$ and using Eq. (3.7), we obtain that $H_{\mathrm{s}} \propto F_{\mathrm{x}}^{-\alpha}$. Introducing the dimensionless quantity $H_{\mathrm{s}}/R_{\mathrm{NS}}$, we can write

$$H_{\mathrm{s}}/R_{\mathrm{NS}} = KF_{\mathrm{x}}^{-\alpha}, \tag{3.9}$$

and finally,

$$E_{\mathrm{CRSF}}(F_{\mathrm{x}}) = \frac{E_0}{(KF_{\mathrm{x}}^{-\alpha} + 1)^3}, \tag{3.10}$$

where the factor K determines the height of the collisionless shock. E_0 and K are found as fit parameters of observational data. In our case, $E_0 = 31.4 \pm 0.2$ keV and $K = 0.024 \pm 0.003$ $(\mathrm{erg/s})^\alpha$.

As shown in Fig. 3.7, the collisionless shock model represented with the solid curve describes the observed positive E_{CRSF}/L_x correlation reasonably well. We note the apparent turn-up of CRSF energies at the high end of the explored X-ray luminosity range, however. The model presented above does not predict such a behaviour, but only yields a flattening at high luminosities. If this were real, the visible turn-up may indicate gradual deviations from the model being considered here. Indeed, with increasing mass accretion rate, the radiation pressure becomes more and more important, so that the simplest version of the collisionless shock may not be fully applicable for the brightest states. This intermediate case between the two regimes is the most difficult to treat, and apparently full-radiation hydro simulations are needed to investigate this interval of luminosities. We also note that the limited number of data points and their accuracy do not exclude the possibility that the indication of the second derivative is a pure statistical or systematic effect.

Substituting the measured F_x and K, and assuming $R_{NS} = 10$ km in Eq. (3.9), we obtain averaged shock heights of ~200 m and 100 m above the NS surface for observations II (in the outburst decay) and I (near the outburst maximum), respectively.

Hardness ratio – luminosity dependence

The X-ray spectral analysis presented above revealed a strong and apparently non-linear correlation between spectral hardness ratio and X-ray luminosity in Cep X-4. Generally, an increase of spectral hardness with luminosity is expected to be due to the increase of the electron number density n_e with increasing $\dot{M}$, leading to more effective Comptonisation of the emerging X-ray spectrum. In the model with a collisionless shock, most of the energy is released near the NS surface where the continuum spectrum comptonized by electrons between the NS surface and the shock, is produced. Numerical simulations performed by Bykov & Krasilshchikov (2004) suggest that at a given accretion rate neither T_e and n_e change significantly downstream of the shock. The shape of the emerging spectrum depends on the energy exchange between photons and electrons (the dimensionless Comptonisation y-parameter, Kompaneets (1956)), which in the strong magnetic field is (Basko & Sunyaev 1975)

$$y = \frac{2}{15} \frac{kT_e}{m_e c^2} \text{Max}\{\tau, \tau^2\}, \qquad (3.11)$$

where τ is the characteristic optical depth of the region and all other notations are standard. Consider a cylindrical geometry of the accretion region with the polar cap area A and height H_s. In real X-ray observations, the geometry is averaged over the viewing angle by the rotation of the NS, therefore the appropriate characteristic scale of the problem is

$$r_{eff} = (AH_s)^{1/3}. \qquad (3.12)$$

Comptonisation is effective for $y \sim 1$, and the number of scatterings in this region is $\sim \tau_{eff}^2 \propto n_e^2 r_{eff}^2$. The effective y-parameter of the problem therefore scales as

$$y_{eff} \propto \tau_{eff}^2 \propto n_e^2 r_{eff}^2 \propto \left(\frac{\dot{M}}{A}\right)^2 (AH_s)^{\frac{2}{3}} \propto \dot{M}^{\frac{10}{7}} \dot{M}^{\frac{4}{21}} \dot{M}^{-\frac{10}{21}} \propto \dot{M}^{\frac{24}{21}}, \qquad (3.13)$$

where we have made use of the standard dependence $A \propto \dot{M}^{2/7}$ (a dipole magnetic field geometry). Next, we use the standard solution of the unsaturated Comptonisation problem

(Pozdnyakov et al. 1983), where the emerging spectral flux at photon energies $h\nu < kT_e$ can be written as

$$F_\nu = C\nu^{-\alpha} \tag{3.14}$$

with the spectral index

$$\alpha = -\frac{3}{2} + \sqrt{\frac{9}{4} + \frac{2}{15y_{eff}}} \,. \tag{3.15}$$

(Here we made use of the decrease in the efficiency of the energy exchange between electrons and photons in a strong magnetic field, see Eq. (3.11) above). The spectral hardness ratio is determined in the usual way:

$$\mathrm{HR} = \frac{\int\limits_{\nu_3}^{\nu_4} F_\nu d\nu}{\int\limits_{\nu_1}^{\nu_2} F_\nu d\nu}, \tag{3.16}$$

where, in our case, the frequencies ν_1, ν_2, ν_3, and ν_4 correspond to energies of 4, 6, 8, and 12 keV, respectively. Plugging Eq. (3.14) and Eq. (3.15) into Eq. (3.16) and taking Eq. (3.13) into account, we arrive at

$$\mathrm{HR} = \frac{\int\limits_{\nu_3}^{\nu_4} \nu^{3/2 - \sqrt{9/4 + 2/(15y_{eff})}} d\nu}{\int\limits_{\nu_1}^{\nu_2} \nu^{3/2 - \sqrt{9/4 + 2/(15y_{eff})}} d\nu} = \frac{\int\limits_{\nu_3}^{\nu_4} \nu^{3/2 - \sqrt{9/4 + 2/(15K_y \dot{M}^{24/21})}} d\nu}{\int\limits_{\nu_1}^{\nu_2} \nu^{3/2 - \sqrt{9/4 + 2/(15K_y \dot{M}^{24/21})}} d\nu}, \tag{3.17}$$

where the parameter K_y is found from fitting of the observed HR change with X-ray flux.

The best-fit model is presented in Fig. 3.8. Clearly, the model of Eq. (3.17) describes the observed behaviour of hardness ratio with increasing X-ray luminosity of Cep X-4 well. The best-fit value of the sole parameter is $K_y \simeq 0.14$, which corresponds to an effective y-parameter range $\sim 0.2 - 1.2$ during the observed luminosity change in Cep X-4. These values of y_{eff} are consistent with the unsaturated Comptonisation regime, which justifies the use of Eq. (3.14) and Eq. (3.15) for the model fitting.

3.4.2 Numerical simulations

To illustrate the qualitative analysis given above, we performed numerical simulations of radiative transfer in the scattering medium above the neutron star polar cap using a two-dimensional Feautrier method to obtain the hardness ratio.

The Feautrier method is a powerful tool of radiation transfer calculations in regions with given structure (temperature and density distributions) and is widely used for spectrum calculations (Nagel 1981a,b; Nagel & Meszaros 1985; Alexander et al. 1989). In these works a one-dimensional model for two particular geometries was applied. In a collisionless shock model, where the radiation from the top of the column could be comparable to that of the sidewalls, it is necessary to take a two-dimensional radiative transfer into account.
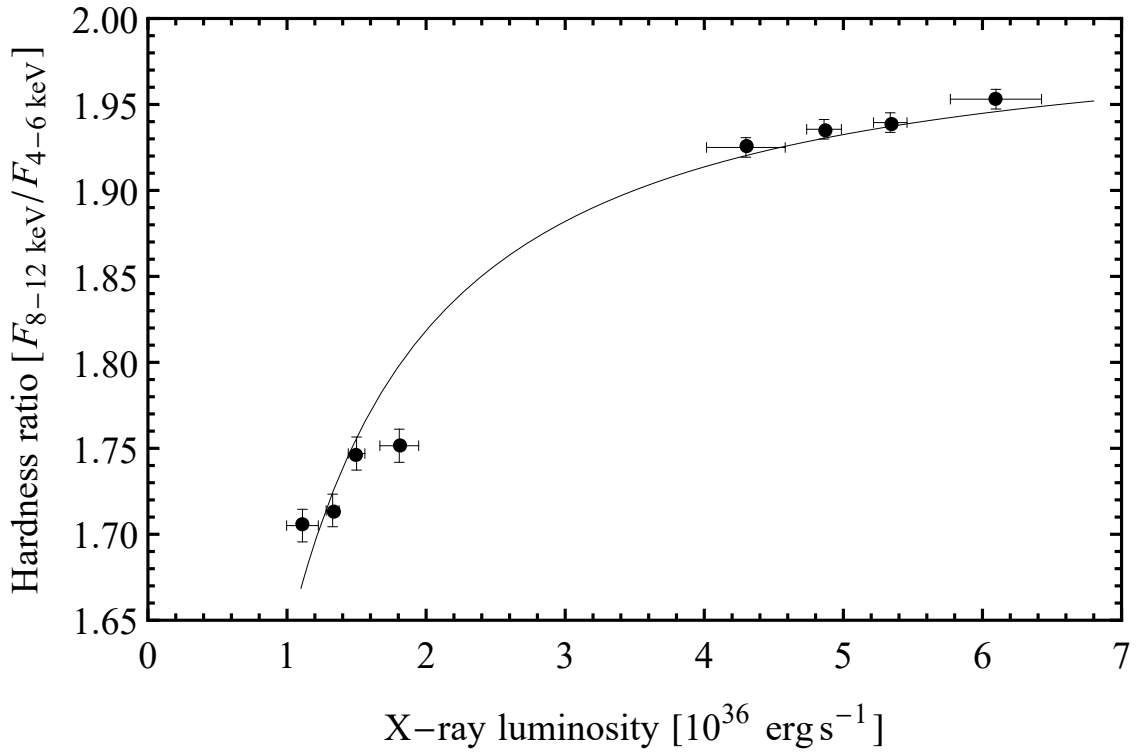
Figure 3.8: Similar to Fig. 3.7, but for the spectral hardness ratio. The solid curve represents a model expressed by Eq. (3.17), $\chi^2_{\text{red}}/\text{d.o.f.} = 1.36/7$.

For this reason, we used a generalised two-dimensional Feautrier method (Cannon 1970) to calculate the continuum and (with less accuracy) the fundamental CRSF feature. The calculation domain is taken to be a cylindrical column filled with plasma of constant temperature and density. The radiative transfer for two polarisation modes is used in the geometrical optics limit. We employ cylindrical coordinates, assuming axial symmetry; $z = 0$ at the NS surface and $r = 0$ at the centre of the column.

The radiative transfer equation for the scattering atmosphere reads

$$\frac{\sin^2 \theta_i}{2\sigma_i} \left(\frac{\partial^2 u_i}{\partial r^2} + \frac{1}{r} \frac{\partial u_i}{\partial r} \right) + \frac{\cos^2 \theta_i}{\sigma_i} \frac{\partial^2 u_i}{\partial z^2} - \sigma_i u_i + \sum_{j=1}^{N} S_{ij} u_j = 0. \tag{3.18}$$

Here θ is the angular coordinate, $u_i(\omega, \theta, r, z) = \frac{1}{2} [I_i(\omega, \theta, r, z) - I_i(\omega, -\theta, r, z)]$, where I is the intensity; $\sigma_i = \sigma_i(\omega, \theta, z)$ is the scattering coefficient independent of the r-coordinate because the magnetic field is assumed to be oriented along the z-axis.

The redistribution matrix elements S_{ij} are calculated using the equations for differential scattering cross sections from Bussard et al. (1986) derived in a fully relativistic approximation. Thus the second-order Doppler effect and the non-harmonicity of the electron Landau levels are included in our calculations. We restricted ourselves to considering the $n = 1$ Landau level for the intermediate excited state and did not take spin-flip transitions into account. The derivation of the fully relativistic normal modes including vacuum and plasma effects requires special treatment, and here we used the non-relativistic vacuum-plasma normal modes from Nagel & Meszaros (1985), for the sake of simplicity.

The calculations were performed assuming the mass accretion rates $\dot{M} = 5 \cdot 10^{16}$ g s^{-1} and $\dot{M} = 1.5 \cdot 10^{16}$ g s^{-1} , corresponding to the averaged luminosities of observations I and II, respectively. The electron temperature of the column was set to 5.8 keV for both accretion rates, which is close to the electron temperature obtained in numerical modelling (Bykov & Krasilshchikov 2004). The electron number density is a function of $\dot{M}$ and the polar cap radius (Eq. (3.7)).

The bottom of the column (polar cap with area A where most of the accretion power is released) serves as the source of photons. Because scattering is important in a thin emission region above the polar cap, we assume a modified black-body spectrum of seed photons. Other boundary conditions are that there is no incident radiation onto the top and the sidewall of the column, $\partial u / \partial r = 0$ along the z-axis.

The temperature of the seed radiation is a function of the accretion rate. Taking into account that $L \propto T^4 A \propto \dot{M}$ and using the standard dependence for the polar cap area, $A \propto \dot{M}^{2/7}$, the temperature ratio for different mass accretion rates is

$$\frac{T_1}{T_2} = \left(\frac{\dot{M}_1}{\dot{M}_2} \right)^{5/28} . \tag{3.19}$$

The temperature of the radiation coming from the polar cap was fixed to 12 keV for observation II with the lower mass accretion rate.

The results of the simulation for the two accretion rates are shown in Fig. 3.9.

Figure 3.9 shows the emerging model spectra from the accretion column calculated as specific flux per unit surface integrated over the entire column for observations I (dashed line) and II (dash-dotted line). To compare them with the observed continua (solid and dotted lines, respectively), the modeled specific luminosity from two columns was divided by some factor to match the continuum given by the `fdcut` function. This factor is equal to $4\pi d^2$, where $d \sim 4$ kpc is the distance to the source.

The hardness ratios of the modelled spectra are calculated to be 1.93 and 1.74 for observations I and II, respectively, which is very similar to the observed values (see Fig. 3.6). This shows that the model spectra are in good agreement with the observed continua, confirming the expected hardening of the continuum with increasing mass accretion rate. It should be noted that here we did not study the E_{CRSF}/L_x correlation obtained from the simulations because the accuracy of the calculations is not high enough to analyse the line centroid energy. The application of the Feautrier method for the cyclotron line energy variations will be explored in the future work.

We therefore conclude that changing the electron density downstream of the collisionless shock above the NS polar cap is consistent with the observed hardness ratio evolution with X-ray luminosity in Cep X-4.

3.5 Conclusions

We have investigated the spectral-luminosity variability in the X-ray pulsar Cep X-4 using NuSTAR observations of the 2014 outburst. The intrinsic pulse-to-pulse variability of Cep X-4 allowed us to reveal strong positive E_{CRSF}/L_x correlations on short timescales of one cycle of X-ray pulsations (minutes) as well as on long timescales of weeks (at least 12 days during which the source becomes fainter by a factor of about 3.5). Moreover, linear
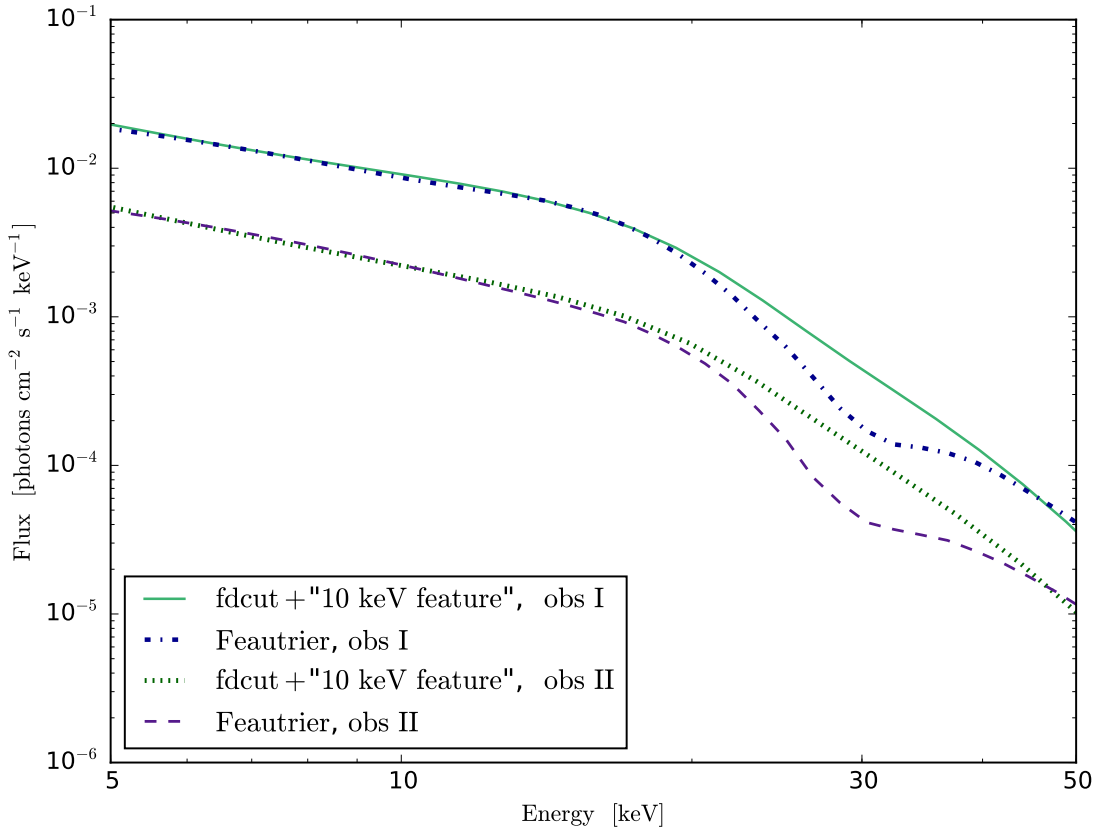
Figure 3.9: Model spectra with the observed `fdcut` continua for observations I and II. (I): $\dot{M} = 5 \cdot 10^{16}$ g s^{-1}, the polar cap radius $r_0 = 0.38$ km, the height of the column $z_0 = 77$ m, $n_e = 2.66 \cdot 10^{21}$ cm^{-3}. (II): $\dot{M} = 1.5 \cdot 10^{16}$ g s^{-1}, $r_0 = 0.32$ km, $z_0 = 180$ m, electron density $n_e = 1.12 \cdot 10^{21}$ cm^{-3}. The temperature of the scattering electrons is $T_e = 5$ keV in both cases.

fits to the data points seem to have the same slope, which might suggest linearity of the processes behind the $E_{\mathrm{CRSF}}/L_{\mathrm{x}}$ correlations.

We also confirm that the continuum becomes harder with X-ray luminosity, that is the spectral hardness ratio ($F_{8-12\,\mathrm{keV}}/F_{4-6\,\mathrm{keV}}$) increases with X-ray flux. However, the slope of the linear fit to the points of the measured hardness ratio clearly changes from the first observation to the second, which implies a more complex form of the dependence than a linear one on long timescales (during at least one outburst).

The evolution of the spectral hardness ratio with X-ray luminosity is successfully described by a model in which a collisionless shock above the neutron star surface is formed. This model also describes the observed positive $E_{\mathrm{CRSF}}/L_{\mathrm{x}}$ correlation reasonably well. Within this model, heights of cyclotron line emerging layers were estimated.

Furthermore, we found a harmonic of the cyclotron feature in both NuSTAR observations. We thus confirm the harmonic of the cyclotron line in the Cep X-4 spectrum, as previously found by Jaisawal & Naik (2015) in Suzaku data.

4.   Observations of V 0332+53

4.1   Introduction

The transient X-ray pulsar V 0332+53 was discovered with the Vela B5 observatory in 1973 during an outburst lasting about three months (Terrell & Priedhorsky 1984). The optical companion is a O8-9Ve spectral class star BQ Cam possessing a decretion disk, which provides the matter accreted by the neutron star. Observations of the optical component resulted in the estimated distance to the binary of about 7 kpc (Negueruela et al. 1999).

During further Tenma and EXOSAT observations performed in 1983 and 1984, pulsations with a period of 4.38 s as well as an orbital period of 34.25 d, with recurrent outbursts, were determined (Stella & White 1983; White et al. 1984). The pulse profile was found to change from double to single peaked with decreasing luminosity during the EXOSAT observations (Stella et al. 1985).

The suggestion that V 0332+53 has a cyclotron resonance scattering feature at around 28.5 keV was based on the spectrum obtained with the *Ginga* observatory (Makishima et al. 1990). This implies the corresponding magnetic field of the line forming region to be of about 3×10^{12} G. During the subsequent outburst in 2004, the line energy was re-measured at 26.3 ± 0.03 keV. In addition to this line, two other absorption features at 49 ± 0.2 and 74 ± 2 were detected. These three absorption feature, interpreted as the fundamental line, the first and second harmonics (Coburn et al. 2005), were also observed in the INTEGRAL and RXTE spectra of V 0332+53 (Kreykenbohm et al. 2005; Pottschmidt et al. 2005).

The transient X-ray pulsar V 0332+53 is a unique cyclotron line source since it exhibits a clear negative correlation of the observed CRSF energy with X-ray luminosity L_x at high luminosities (Tsygankov et al. 2006). In addition to the negative correlation, the cyclotron line energy in this source has been recently shown to be positively correlated with flux at low luminosities (Doroshenko et al. 2017; Vybornov et al. 2018), making V 0332+53 the only source showing both types of E_{cyc}/L_x correlations. Moreover, the line energy has been observed to decay with time during the giant 2015 outburst (Cusumano et al. 2016). Our further analysis revealed that the line energy rebounded to the value that it had at the beginning of the giant 2015 outburst by the weak 2016 outburst (Vybornov et al. 2018), so that the source exhibited more complex time dependence than previously thought.

The time dependence of the line could be related either to accretion-induced changes in the neutron star's intrinsic magnetic field (Cusumano et al. 2016) or to changes in the emission region geometry associated with the changes in the accretion disk structure (Doroshenko et al. 2017; Vybornov et al. 2018).

Table 4.1: Parameters of the analyzed NuSTAR observations.

	ObsID	Date (MJD)	Exp. (ks)	Period (s)
		Group 1		
	80102002002	57223.42-57223.85	10.5	4.3761(6)
2015	80102002004	57275.94-57276.42	14.9	4.3759(0)
	80102002006	57281.92-57282.36	17.0	4.3758(9)
		Group 2		
	80102002008	57295.96-57296.40	18.1	4.3759(4)
	80102002010	57299.99-57300.49	20.8	4.3759(6)
2016	90202031002	57599.75-57600.27	25.2	4.3762(8)
	90202031004	57600.76-57601.27	25.0	4.3763(5)

Here the E_{cyc} behavior during the two consecutive outbursts of the source in 2015 and 2016 is analyzed. The spectral analysis was performed both on long (days) and short (pulse cycle) timescales using a flux-resolved spectroscopy. The first issue to be resolved was to disentangle the luminosity and time dependence by using the flux-resolved spectroscopy since it allows to reconstruct the "pure" luminosity dependence and thus to determine the transition luminosity more precisely. Moreover, the flux-resolved spectroscopy gives an increased number of data points since the E_{cyc}/L_x correlation is built for each observation, i.e. on short time-scales. Another goal is to investigate the time behavior of the line energy in more detail to answer the question whether changes in the global magnetic field or in the geometry of the emitting area are responsible for the time evolution of the line energy during the outbursts in 2015-2016 (Cusumano et al. 2016; Doroshenko et al. 2017). The results of this investigation have recently been published in Vybornov et al. (2018).

4.2 Observations and data reduction

The data of the NuSTAR observations of V0332+53 during the 2015 giant and the 2016 minor outburst (Fig. 4.1), referred to below as the 2015 and 2016 outburst, are analyzed. Although the Swift/BAT light curve[1] is used in Fig. 4.1 to show where the NuSTAR observations are, the BAT data are not considered here as in Doroshenko et al. (2017) to avoid uncertainties related to the cross-calibration between the NuSTAR detectors and Swift/BAT. A short summary of the NuSTAR observations is given in Table 4.1.

The data reduction was performed using the `nupipeline` and `nuproducts` utilities distributed as part of HEASoft 6.19 with calibration files CALDB 20170120 and standard data reduction procedure described in the NuSTAR software documentation[2]. Source spectra and light curves were extracted from a circular region with a radius of 80″ centered on the source. The background was extracted from a circular region with a radius of 100″ situated as far as possible from the source. The spectra for the two NuSTAR detectors

---

[1]https://swift.gsfc.nasa.gov/results/transients/V0332p53/
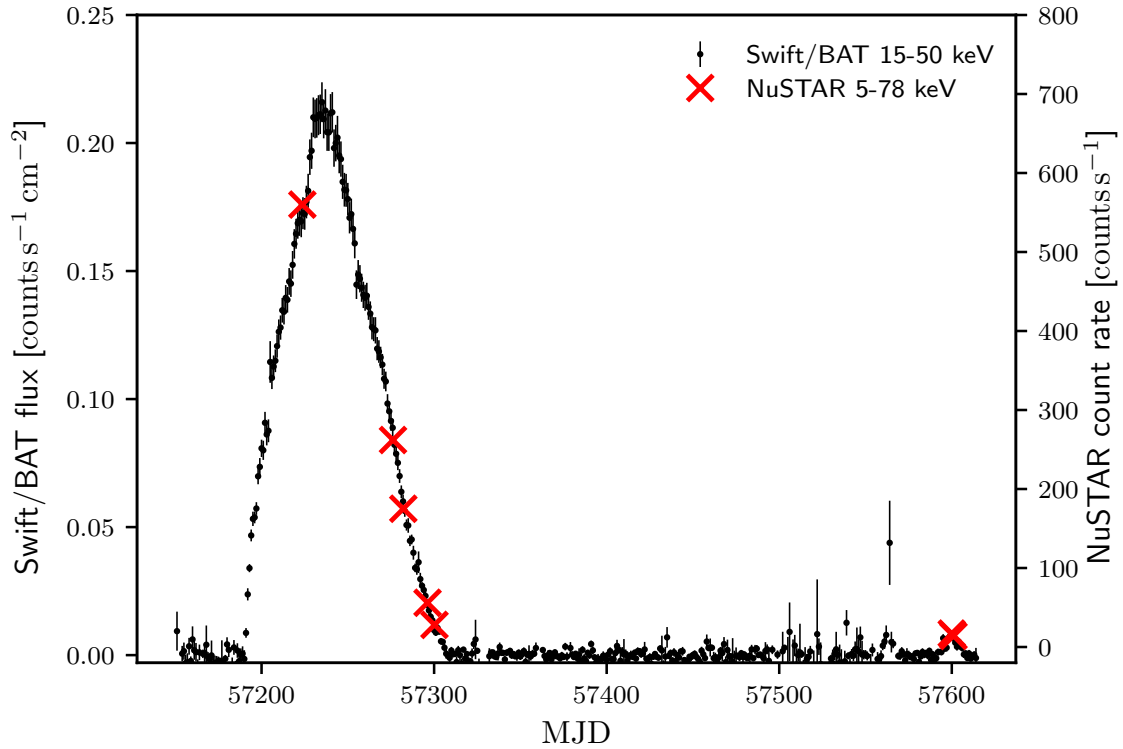[2]https://heasarc.gsfc.nasa.gov/docs/nustar/analysis/nustar_swguide.pdf

Figure 4.1: NuSTAR pointed observations of V 0332+53 during the 2015 giant outburst (red crosses) and the 2016 minor outburst (magenta crosses); the Swift/BAT light curve in the 15-50 keV energy band are shown as black data points.

were analyzed simultaneously in the 5-78 keV energy range for all observations. XSPEC 12.9, Sherpa CIAO 4.9 packages and my own scripts written in the Python programming language were used to analyze the extracted spectra, grouped to at least 25 counts per bin.

In addition to the fundamental line at around 30 keV, the first harmonic of the cyclotron line at ∼ 50 keV is also detected in the broadband NuSTAR spectrum of the source. Being quite prominent, the first harmonic may also affect the fundamental line parameters, so the size of the extraction regions was chosen to optimize the signal-to-noise ratio at high energies where the harmonic is detected.

4.3 Spectral analysis

4.3.1 Flux-averaged spectroscopy

The spectral analysis consisted of two stages: a standard analysis of the pulse-averaged spectra and the pulse-amplitude-resolved analysis or flux-resolved analysis. To carry this out, a spectral model has to be selected. Normally, the spectral continuum of many accreting pulsars is described with a phenomenological model since the underlying physical processes are still not fully understood and there is no generally accepted physical model, despite many theoretical investigations (Wang & Frank 1981; Becker & Wolff 2007; Fer-
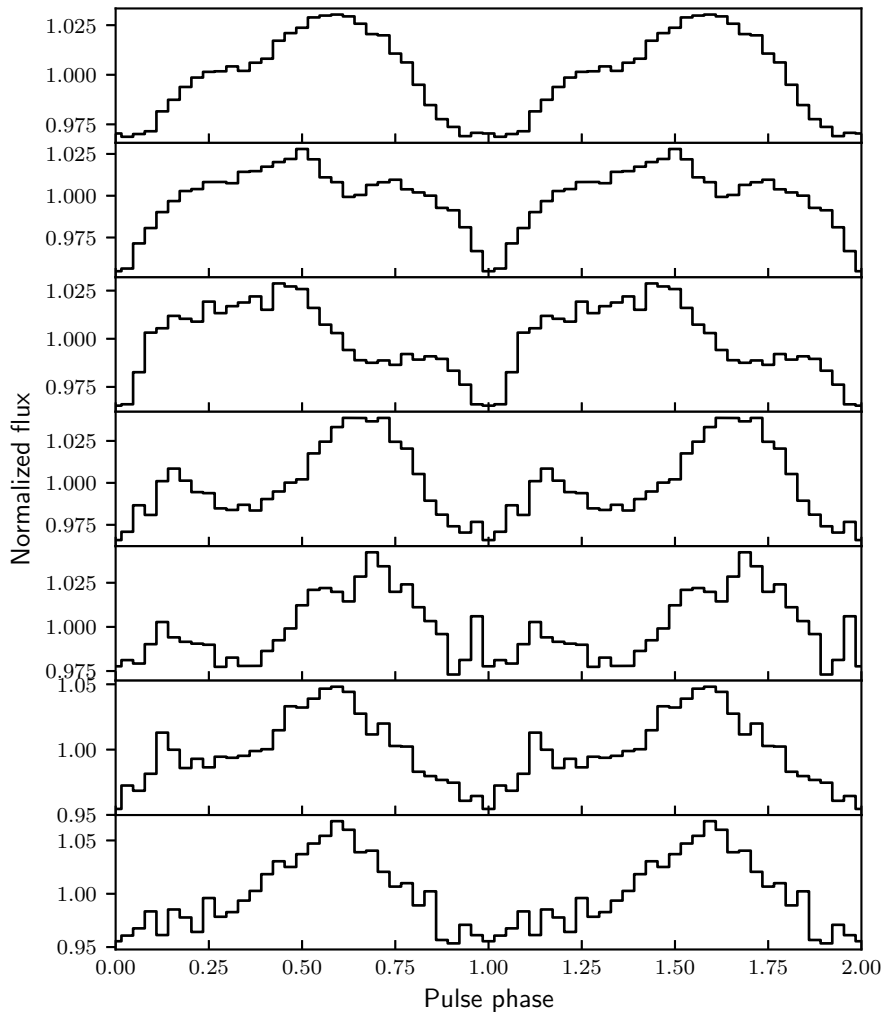
Figure 4.2: NuSTAR pulse profiles in the 3-79 keV energy range. The first five pulse profiles from the top correspond to the 2015 giant outburst, whereas the last two profiles belong to the 2016 minor outburst.

rigno et al. 2009; Farinelli et al. 2012; Ceccobello et al. 2014; Farinelli et al. 2016; Wolff et al. 2016). Nevertheless, the continua of several accreting pulsars are well described with physically based models, and V 0332+53 is one of those sources. The selected model, called `compTT`[3] in the XSPEC utility, was suggested by Titarchuk (1994a) and is based on analytical solutions of the Kompaneets equation (Kompaneets 1956), which describes the Compton interaction of photons propagating in a hot plasma. Note, the model does not include bulk comptonization processes. The basic analytical solutions and approximations for this model were given earlier in Sunyaev & Titarchuk (1980, 1985). The model was also verified through Monte Carlo computations of the comptonization problem in a fully relativistic way by Hua & Titarchuk (1995). This model predicts X-ray and gamma-ray spectra forming as a result of comptonization of soft photons in a hot plasma of both small and large optical depths with corrections of relativistic effects. A

---

[3]https://heasarc.gsfc.nasa.gov/xanadu/xspec/manual/node155.html

more detailed description of this model is given in Appendix B B.

NuSTAR spectra of V 0332+53 were thus analyzed in the 5-78 keV energy range using the `compTT` model as a continuum and a multiplicative Gaussian line of the form

$$G(E) = 1 - d \exp\left(-\ln 2 \frac{(E - E_{\text{cyc}})^2}{\sigma_{\text{cyc}}^2}\right) \qquad (4.1)$$

to describe the cyclotron features. Here d is the depth, σ_{cyc} is the width, and E_{cyc} is the centroid energy of the line. The choice of the cyclotron lines is based on a slightly better description of these features in comparison with the exponential Gaussian line (`gabs`[4] in XSPEC) as shown in Doroshenko et al. (2017). The spectra of the all NuSTAR observations described with the model outlined above with residuals to this model are presented in Fig. 4.3, in which the change of the centroid position of the fundamental cyclotron feature is clearly noticed. The centroid of the harmonic also seems to change between observations, but it is located at the high energy tail of the NuSTAR spectral band, so sufficiently large uncertainties hamper any significant detection of the position change. . The fundamental cyclotron line centroid energy is not entangled to the other parameters of the model as shown by its contour plots in Fig. 4.4. These χ^2 maps also show that the continuum parameters (kT_e and τ) are not correlated with the cyclotron line centroid energy, except the faintest observations, in which these parameters are correlated but not strongly. This justifies the further analysis devoted to revealing correlations between the cyclotron line centroid energy and source X-ray luminosity.

Moreover, such a model selection allows us to compare parameters of the phase averaged spectra with Doroshenko et al. (2017) because we analyzed spectra extracted from the same NuSTAR observations, although in a different manner. For instance, we included the harmonic of the CRSF, but despite the optimization of the extraction region, the width of the harmonic is poorly constrained because of the low statistics, and in particular in the fainter observations. Thus, we fixed the width of the harmonic to a value of 10 keV found for the brightest observation where the parameters of the line are well constrained.

The Fe K_α line is described with a simple Gaussian line profile

$$F(E) = \frac{A}{\sigma \sqrt{2\pi}} \exp \frac{-(E - E_0)^2}{2\sigma^2}, \qquad (4.2)$$

where A is the amplitude in total photons $\text{s}^{-1} \text{cm}^{-2}$ in the line, σ is the line width and E_0 is the centroid energy of the iron line. The iron line also is not detected confidently at low fluxes, so that we fixed the energy and width of the line to values measured during the brightest observation.

Despite a slightly different energy range and the absence of the Swift/BAT data, the continuum and the fundamental cyclotron line parameters are very close to the values obtained by Doroshenko et al. (2017).

4.3.2 Flux-resolved spectroscopy

To assess the variation in the cyclotron line energy with flux within individual observations, we produced pulse-amplitude-resolved spectra by applying the pulse-to-pulse technique elaborated in Klochkov et al. (2011). This method uses flux variability that a source

---

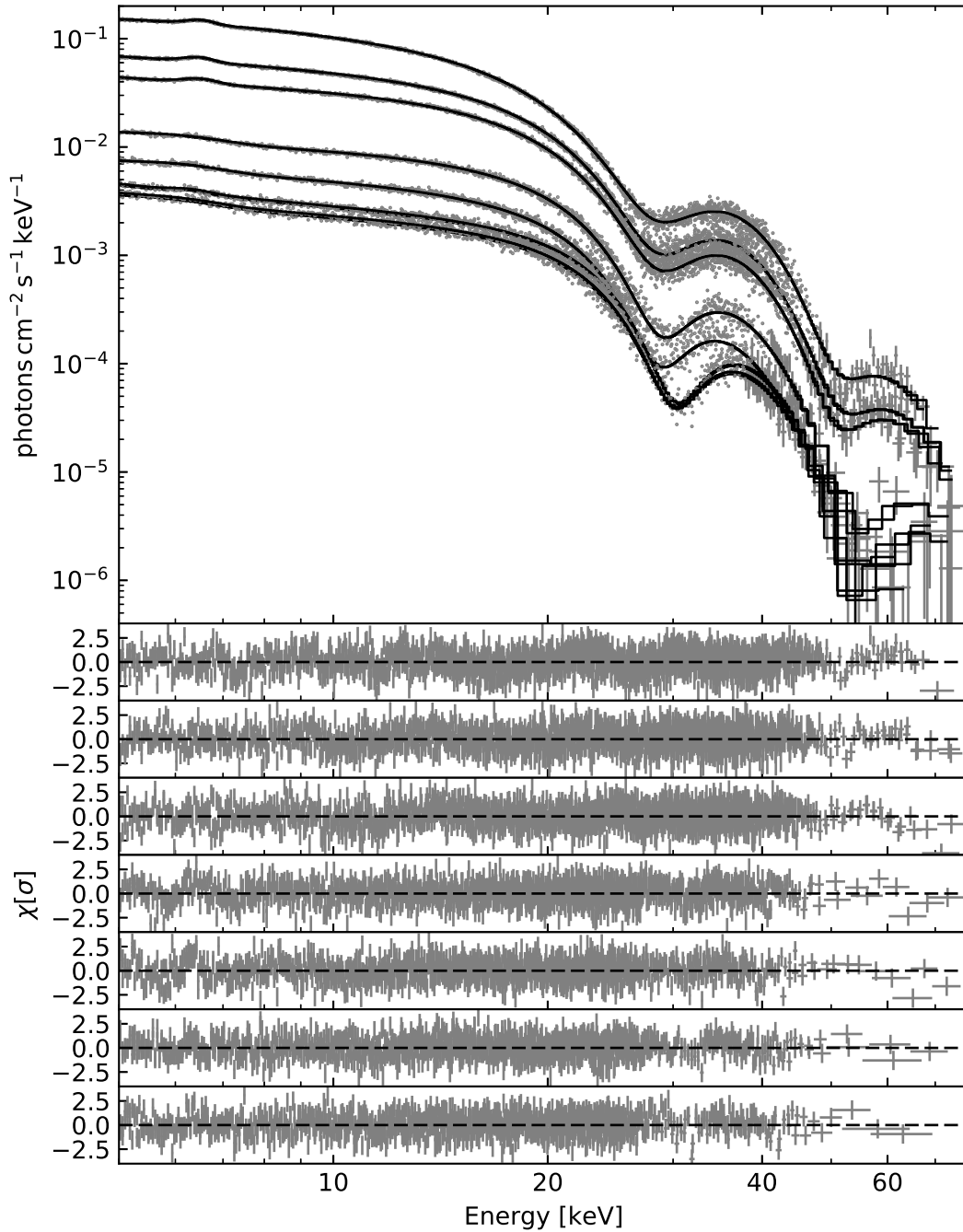[4]https://heasarc.gsfc.nasa.gov/xanadu/xspec/manual/node232.html

Figure 4.3: Phase-averaged spectra between 5 and 78 keV of the all NuSTAR observations performed during the 2015 and 2016 outbursts, and corresponding best-fitting residuals arranged in chronological order from the top to bottom. The best-fit model was chosen to be the `compTT` model as a continuum with two multiplicative Gaussian lines of the form (4.2) as the fundamental line and its harmonic. The fit parameters of the model for each spectrum are presented in Table. 4.2 and Table. 4.3.
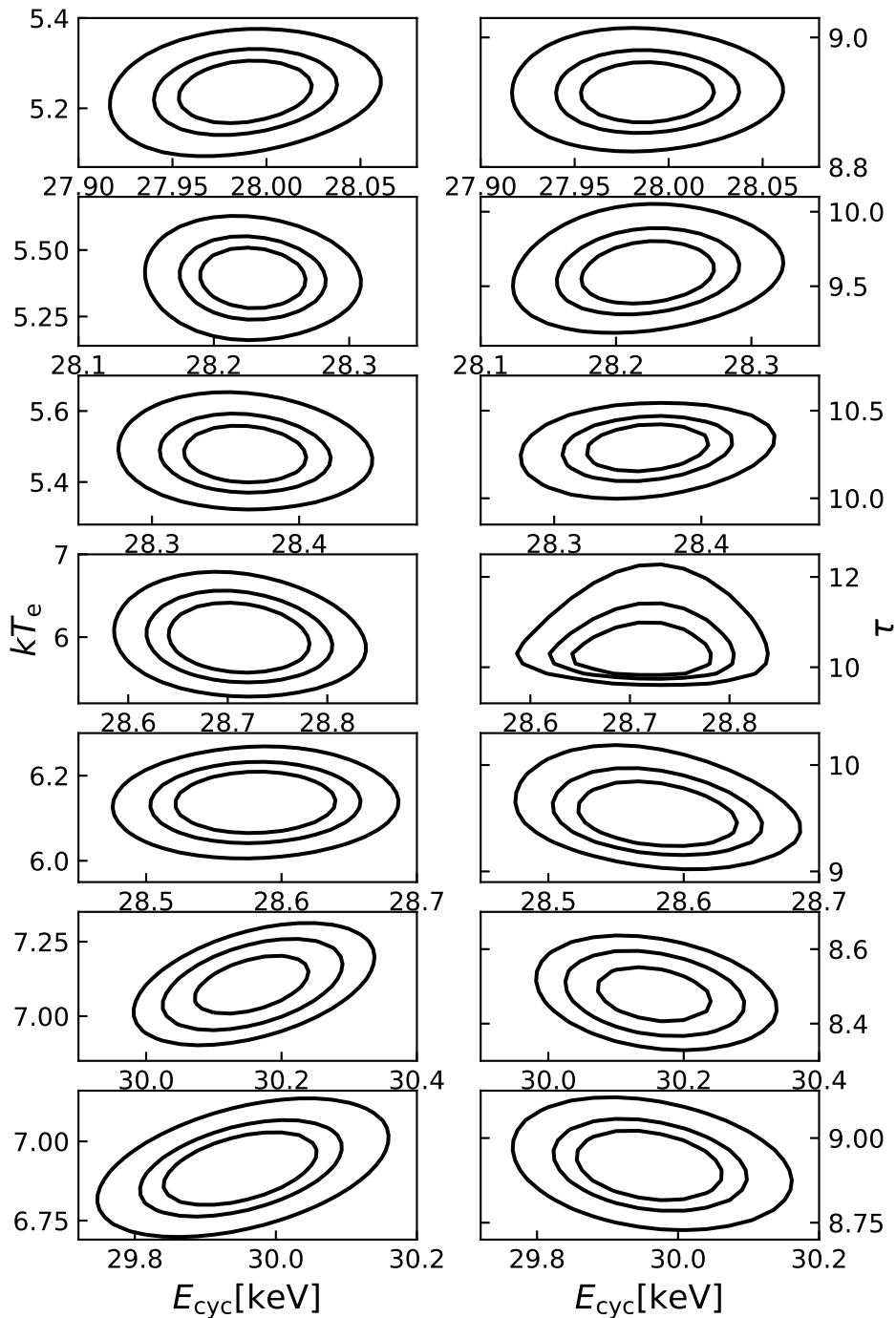
Figure 4.4: Confidence regions of the cyclotron centroid energy E_{cyc} and the continuum parameters kT_e and τ. These parameters are chosen since they define the high energy part and slope of the continuum, and may affect the cyclotron line. The left column shows confidence regions between the cyclotron centroid energy and the energy of the comptonizing electrons kT_e, while at the right side the cyclotron centroid energy versus the optical thickness τ is shown. The observations are arranged in chronological order from the top to bottom. The contours correspond to the 1σ, 2σ, and 3σ confidence levels.

Table 4.2: Parameters of the best-fit model of the pulse-averaged spectra shown in Fig. 4.3 in the energy range of 5-78 keV, obtained with NuSTAR during the 2015 outburst. The "1" superscript marks the harmonic line parameters. The indicated uncertainties are at 1σ (68%) confidence level.

Parameter	80102002002	80102002004	80102002006	80102002008	80102002010
T_0 [keV]	$1.21^{+0.02}_{-0.02}$	$1.04^{+0.03}_{-0.03}$	$0.79^{+0.05}_{-0.07}$	$0.6^{+0.2}_{-0.6}$	$0.6^{+1.5}_{-0.6}$
kT_e [keV]	$5.24^{+0.06}_{-0.06}$	$5.39^{+0.08}_{-0.08}$	$5.47^{+0.06}_{-0.06}$	$6.0^{+0.2}_{-0.3}$	$6.2^{+0.3}_{-0.4}$
τ	$8.9^{+0.1}_{-0.1}$	$9.6^{+0.1}_{-0.1}$	$10.2^{+0.1}_{-0.1}$	$10.2^{+04}_{-0.2}$	$9.5^{+0.9}_{-0.4}$
E_{cyc} [keV]	$27.99^{+0.02}_{-0.02}$	$28.23^{+0.03}_{-0.03}$	$28.36^{+0.03}_{-0.03}$	$28.71^{+0.04}_{-0.04}$	$28.58^{+0.05}_{-0.05}$
w_{cyc}[a] [keV]	$8.2^{+0.1}_{-0.1}$	$7.4^{+0.1}_{-0.1}$	$7.2^{+0.1}_{-0.1}$	$6.2^{+0.1}_{-0.1}$	$5.7^{+0.1}_{-0.1}$
d_{cyc}	$0.858^{+0.003}_{-0.004}$	$0.859^{+0.003}_{-0.003}$	$0.860^{+0.002}_{-0.002}$	$0.877^{+0.004}_{-0.004}$	$0.869^{+0.006}_{-0.006}$
E_{cyc}^1 [keV]	$50.8^{+0.2}_{-0.2}$	$51.1^{+0.2}_{-0.2}$	$50.8^{+0.3}_{-0.2}$	$53.7^{+0.7}_{-0.7}$	$53.5^{+1.2}_{-0.9}$
w_{cyc}^1 [keV]	$10.2^{+0.5}_{-0.5}$	$11.7^{+0.6}_{-0.6}$	$11.7^{+0.6}_{-0.5}$	$19.4^{+3.1}_{-2.7}$	$21.3^{+3.7}_{-3.7}$
d_{cyc}^1	$0.86^{+0.01}_{-0.01}$	$0.89^{+0.01}_{-0.01}$	$0.90^{+0.01}_{-0.01}$	$0.98^{+0.1}_{-0.1}$	$1.0^{+0.02}_{-0.1}$
d_{cyc}^1	$0.86^{+0.01}_{-0.01}$	$0.89^{+0.01}_{-0.01}$	$0.90^{+0.01}_{-0.01}$	$0.98^{+0.1}_{-0.1}$	$1.0^{+0.02}_{-0.1}$
$E_{\mathrm{Fe}\,K_\alpha}$ [keV]	$6.5^{+0.01}_{-0.01}$	$6.5^{+0.01}_{-0.01}$	$6.4^{+0.01}_{-0.02}$	$5.8^{+0.1}_{-0.2}$	$6.0^{+0.2}_{-0.5}$
$\sigma_{\mathrm{Fe}\,K_\alpha}$ [keV]	$0.28^{+0.01}_{-0.01}$	$0.30^{+0.02}_{-0.02}$	$0.35^{+0.02}_{-0.02}$	$1.0^{+0.1}_{-0.1}$	$0.9^{+0.5}_{-0.3}$
A_{Fe}[b]	$8.5^{+0.3}_{-0.3}$	$4.6^{+0.2}_{-0.2}$	$3.4^{+0.2}_{-0.2}$	$4.1^{+1.2}_{-0.8}$	$1.6^{+2.2}_{-0.8}$
C_{FPMB}[c]	1.0127 ± 0.0007	1.0145 ± 0.0009	1.013 ± 0.001	1.011 ± 0.002	1.009 ± 0.002
$L_{5-78\,\mathrm{keV}}$[d]	14.9 ± 0.2	7.6 ± 0.1	5.2 ± 0.1	1.66 ± 0.08	0.91 ± 0.02
χ^2_{red}/d.o.f.	$1.14/1943$	$1.15/1887$	$1.12/1833$	$1.06/1375$	$1.06/1246$

[a] The width is in terms of the FWHM.
[b] In 10^{-3} photons s^{-1} cm^{-2} keV^{-1} at 1 keV.
[c] A cross-calibration constant for FPMB relative to FPMA.
[d] Luminosity within the 5-78 keV range in 10^{37} erg/s.

Table 4.3: Parameters of the best-fit models of the pulse-averaged spectra shown in Fig. 4.3 in the energy range of 5-78 keV, obtained with NuSTAR during the 2016 outburst. The "1" superscript marks the harmonic line parameters. The indicated uncertainties are at 1σ (68%) confidence level.

Parameter	90202031002	90202031004
T_0 [keV]	$0.6^{+0.1}_{-0.6}$	$0.6^{+0.2}_{-0.6}$
kT_e [keV]	$7.1^{+0.5}_{-0.3}$	$6.9^{+0.6}_{-0.5}$
τ	$8.4^{+0.3}_{-0.1}$	$8.9^{+0.4}_{-0.2}$
E_{cyc} [keV]	$30.15^{+0.06}_{-0.06}$	$29.95^{+0.07}_{-0.06}$
w_{cyc}[a] [keV]	$6.2^{+0.1}_{-0.1}$	$6.2^{+0.2}_{-0.2}$
d_{cyc}	$0.90^{+0.01}_{-0.01}$	$0.89^{+0.01}_{-0.01}$
E^1_{cyc} [keV]	$55.3^{+0.8}_{-0.6}$	$56.6^{+1.3}_{-1.0}$
w^1_{cyc} [keV]	22^{+7}_{-3}	24^{+10}_{-5}
d^1_{cyc}	$1.0^{+0.1}_{-0.1}$	$1.0^{+0.1}_{-0.1}$
$E_{\mathrm{Fe}\,K_\alpha}$ [keV]	$6.3^{+0.1}_{-0.1}$	$6.2^{+0.1}_{-0.2}$
$\sigma_{\mathrm{Fe}\,K_\alpha}$ [keV]	$0.4^{+0.1}_{-0.1}$	$0.8^{+0.2}_{-0.1}$
A_{Fe}[b]	$0.3^{+0.1}_{-0.1}$	$0.7^{+0.3}_{-0.1}$
C_{FPMB}[c]	1.031 ± 0.003	1.047 ± 0.004
$L_{5-78\,\mathrm{keV}}$[d]	0.56 ± 0.02	0.44 ± 0.02
χ^2_{red}/d.o.f.	0.97/1203	1.03/1162

[a] ,[b], [c], [d] The same as in Table 4.2.

exhibits from pulse to pulse, allowing us to investigate spectral-luminosity dependencies on timescales on the order of the pulse period.

First of all, to produce a binary-corrected light curve, the orbit parameters of the source published by Doroshenko et al. (2016) were used. Then barycenter correction was also applied to the light curve using the `barrycorr` tool from the HEASoft package. Given the binary- and barycenter-corrected data, the pulse periods, presented in Table 4.1, are measured and the pulse profiles shown in Fig. 4.2 are produced.

For every pulse we measured a number of counts in the whole pulse in the 3 - 78 keV energy range, and this number of counts, which is apparently equivalent to the pulse amplitude, is used as a measure of the pulse brightness. Note that this number of counts should be calculated not from the event file containing photon arrival times, but derived from the dead-time corrected light curve because V 0332+53 in outburst states is too bright for the NuSTAR detectors, in particular in the first three observations of the 2015 outburst. Dead-time corrections thus have to be taken into account, otherwise the shape of the pulse profile is completely wrong as shown in Fig.4.6, leading to the incorrect number of counts in pulses.

We then built a frequency distribution of pulses as a function of the total number of counts in a pulse (Fig. 4.5). We verified that the distribution is wider than the Poisson distribution with the same mean value of counts in a pulse, otherwise the observed pulse amplitude variability is caused by statistical fluctuations. Based on the observed distribution of pulse amplitudes we then divided all the pulses into four groups to conduct the pulse-amplitude-resolved spectral analysis. The number of groups is somewhat arbitrary and depends on the available counting statistics, so that it was defined experimentally to ensure that the cyclotron line centroid energy is well constrained when fitting the resulting spectra. We derived a pulse using good time intervals (GTIs), then defined to which part of the distribution it belongs by calculating the number of counts in this pulse, and finally stacked up the counts of all pulses that fall into the same part of the distribution. This procedure was performed for five NuSTAR observations of the 2015 giant outburst. The observations of the 2016 outburst have insufficient statistics to apply the pulse-to-pulse technique.

The spectra of the source and the background of each interval were extracted and described using the same model as described above. In the case of limited counting statistics, we had to fix the continuum parameters, the width of the fundamental, and parameters of the harmonic to values obtained for the flux-averaged spectrum, concentrating thus only on the changes in the fundamental centroid energy.

4.4 Results

The analysis has resulted in several $E_{\mathrm{cyc}}/L_{\mathrm{x}}$ correlations obtained on short timescales for each observation and presented in Fig. 4.7, to which we refer below as "p2p" correlations. In particular, Fig. 4.7 shows that there are two distinct groups of observations, i.e., showing a positive or negative correlation of the line energy with flux.

Group 1 includes the high luminous observations (ObsID 80102002002, 80102002004 and 80102002006), where a negative $E_{\mathrm{cyc}}/L_{\mathrm{x}}$ correlation is observed. For Group 2 (ObsID 80102002008 and 80102002010) the trend reverses to a clear positive $E_{\mathrm{cyc}}/L_{\mathrm{x}}$ correlation, confirming the transition already reported by Doroshenko et al. (2017). Here, however,
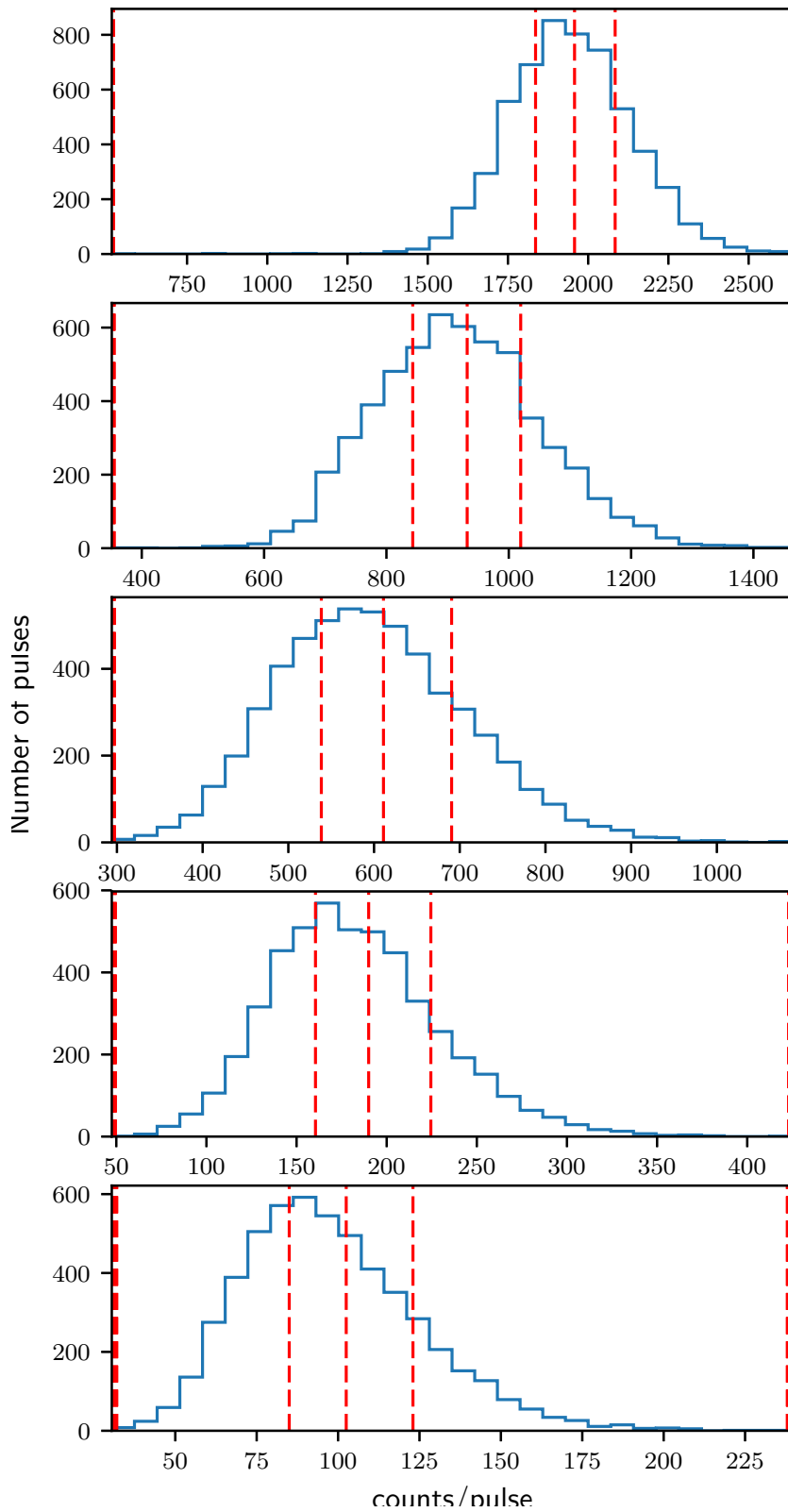
Figure 4.5: Normalized distributions of counts in individual pulses for the observations during the giant outburst used in the pulse-amplitude-resolved analysis. The date of observations increases from top to bottom. The red dashed lines indicate the boundaries of the amplitude bins in which the total number of counts is equal.
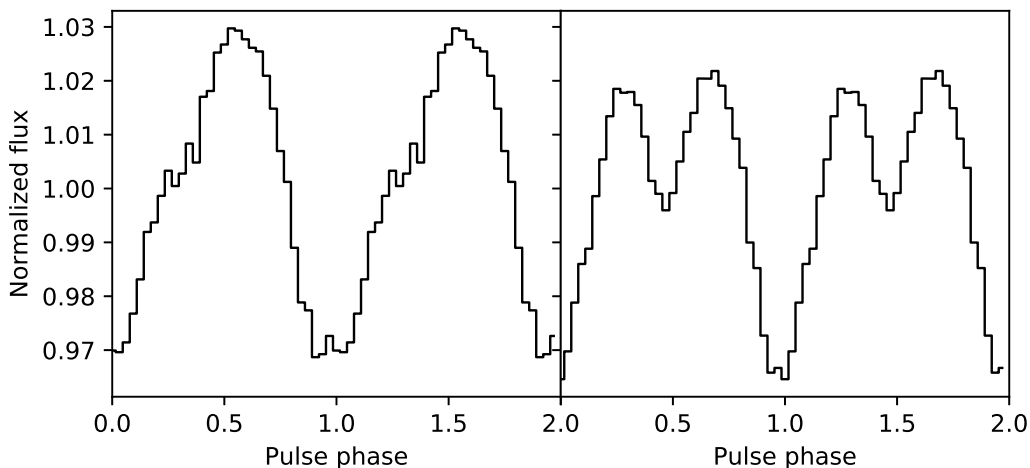
Figure 4.6: Example of the pulse profile of the first (ObsID 80102002002) observation in the 3-78 energy range derived from the dead-time corrected light curve (left) compared with the pulse profile produced without taking the dead-time effect into account (right).

we can measure the variations in the line energy more precisely because we are able to use a larger number of data points with sufficiently small error bars splitting each observation according to the pulse amplitude. This is very important for the low-flux observations, for which we obtained eight points instead of two.

The dependence of E_{cyc} on luminosity turns out to be linear and the slopes are consistent with being the same for all observations within the two groups. This becomes evident when the time dependence of E_{cyc} is removed (see Fig. 4.8). The shift between the individual observations is associated with the previously reported decrease in cyclotron energy with time (Cusumano et al. 2016). Assuming that each observation probes an "instantaneous" behavior of the cyclotron line (the influence of the time variation is negligible within individual observations), we estimated the rate of the decrease in the line energy using the observed shifts based on *NuSTAR* data alone. So, fitting all five p2p-correlations simultaneously using a broken linear model, similarly to Doroshenko et al. (2017), assuming common slopes within each group, is successful and neatly shown in the upper part of Fig. 4.8. The broken linear model has the following free parameters: the luminosity at which the correlation changes from positive to negative, the corresponding value for E_{cyc} (the reference time is the onset of the 2015 outburst, MJD 57190.0), the two slopes of the linear correlations, and the value for the (assumed linear) drift of E_{cyc} with time.

We find the slopes for the two groups of -0.139 ± 0.007 keV/[10^{37}erg s^{-1}] and 0.21 ± 0.08 keV/[10^{37}erg s^{-1}] and, therefore, we confirm the reported transition from a negative correlation at high luminosities to a positive correlation at low luminosities in V 0332+53 with high significance ($\sim 22\sigma$). The transition luminosity is found to be $(2.1 \pm 0.4) \times 10^{37}$ erg/s (assumed at MJD $\sim$ 57288). The decay rate of E_{cyc} in the observations with negative correlation is found to be -0.0162 ± 0.0009 keV/day, which is consistent with the values reported by Doroshenko et al. (2017). The total decrease in line energy over the entire outburst is then ~ 1.5 keV, consistent with the value reported by Cusumano et al. (2016).

We note that after Her X-1, for which the first combined analysis of the coexisting luminosity and time dependences of a cyclotron line was reported (Staubert et al. 2016),

69

Table 4.4: Luminosities and cyclotron line energies of the best-fit models of spectra produced by the pulse-to-pulse technique. The luminosities are derived based on observed fluxes in the 5-78 keV energy range assuming the source distance of 7 kpc; uncertainties for luminosities are correspond to 1σ-uncertanties in bins of the count distributions represented in Fig. 4.7. Other model parameters were fixed to values obtained from averaged spectra.

| ObsID	$L_{5-78\,\text{keV}}$	E_{cyc}	χ^2/d.o.f
	(10^{37} erg/s)	(keV)	
80102002002	16.7 ± 0.7	27.76 ± 0.02	
	15.3 ± 0.3	27.94 ± 0.02	1.055/5565
	14.5 ± 0.3	28.09 ± 0.02	
	13.2 ± 0.8	28.25 ± 0.02	
80102002004	8.9 ± 0.6	28.00 ± 0.03	
	7.9 ± 0.2	28.19 ± 0.03	1.061/5227
	7.2 ± 0.2	28.27 ± 0.03	
	6.2 ± 0.5	28.37 ± 0.03	
80102002006	6.4 ± 0.5	28.20 ± 0.03	
	5.5 ± 0.2	28.38 ± 0.03	1.074/5027
	4.9 ± 0.2	28.46 ± 0.03	
	4.1 ± 0.4	28.52 ± 0.03	
80102002008	2.2 ± 0.2	28.83 ± 0.05	
	1.8 ± 0.1	28.73 ± 0.05	1.036/4132
	1.5 ± 0.1	28.76 ± 0.05	
	1.2 ± 0.2	28.66 ± 0.05	
80102002010	1.2 ± 0.2	28.83 ± 0.05	
	0.96 ± 0.05	28.73 ± 0.05	1.033/3849
	0.81 ± 0.04	28.76 ± 0.05	
	0.62 ± 0.09	28.66 ± 0.05	
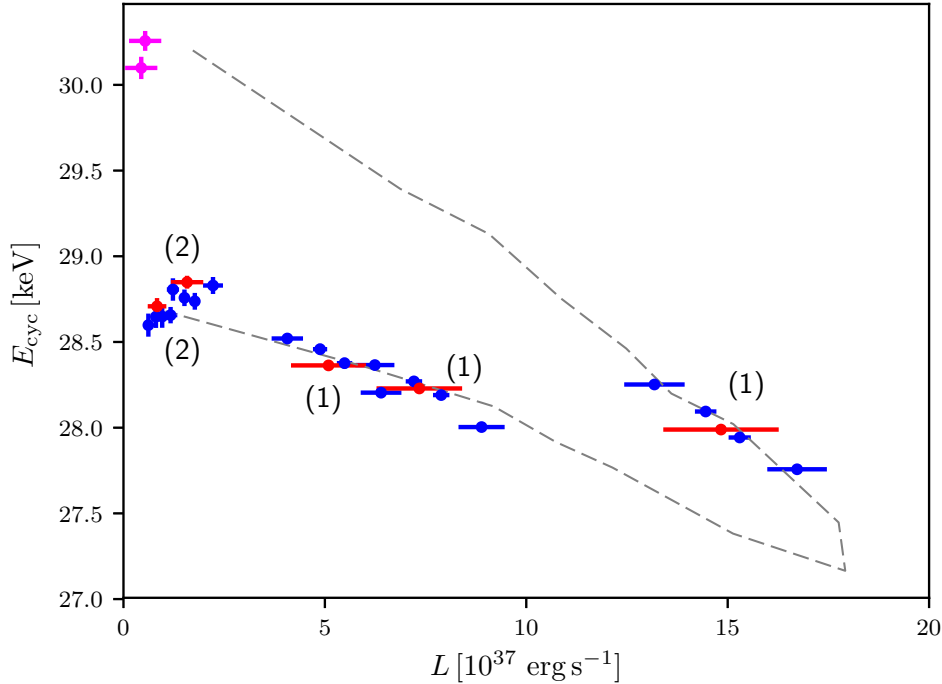
Figure 4.7: Dependence of the energy of the fundamental cyclotron line on luminosity. The two positive and three negative correlations clearly seen in the figure are derived from the pulse-to-pulse analysis (blue crosses). The red and magenta crosses are values obtained from the pulse-averaged spectra of the 2015 giant outburst and the 2016 outburst. The observations with negative p2p-correlations comprise Group 1, while Group 2 consists of two observations with positive p2p-correlations, labeled (1) and (2), respectively. The gray line reflects the "hysteresis" behavior observed with Swift/BAT (Cusumano et al. 2016).

and Vela X-1 (La Parola et al. 2016), V 0332+53 is now the third source that shows such a behavior.

Figure 4.8 shows data points corrected for the time variation (blue crosses) and for the combined fit reflecting the behavior of the CRSF energy with luminosity in the giant outburst corrected for a linear decay in time. Consistent with the report in Doroshenko et al. (2017), the line energies measured in the 2016 outburst (magenta crosses) do not seem to be shifted, that is the drop of the CRSF energy during the giant outburst was completely recovered by that time.

It is the first time that both the pulse-amplitude-resolved and the traditional pulse-amplitude-averaged analyses of the same observations of an outburst of the same source provide the same result, demonstrating the potential of this novel technique.

It also is interesting to note that the overall decay of the cyclotron line energy seems to slow down or even reverse closer to the end of the outburst, as shown in Fig. 4.9. If we describe the observed line energy offsets with a broken linear function (i.e., flattening to a constant after a break), the break surprisingly occurs at MJD ~ 57282(4), close to the transition between the two accretion regimes (MJD ~ 57288), which might suggest
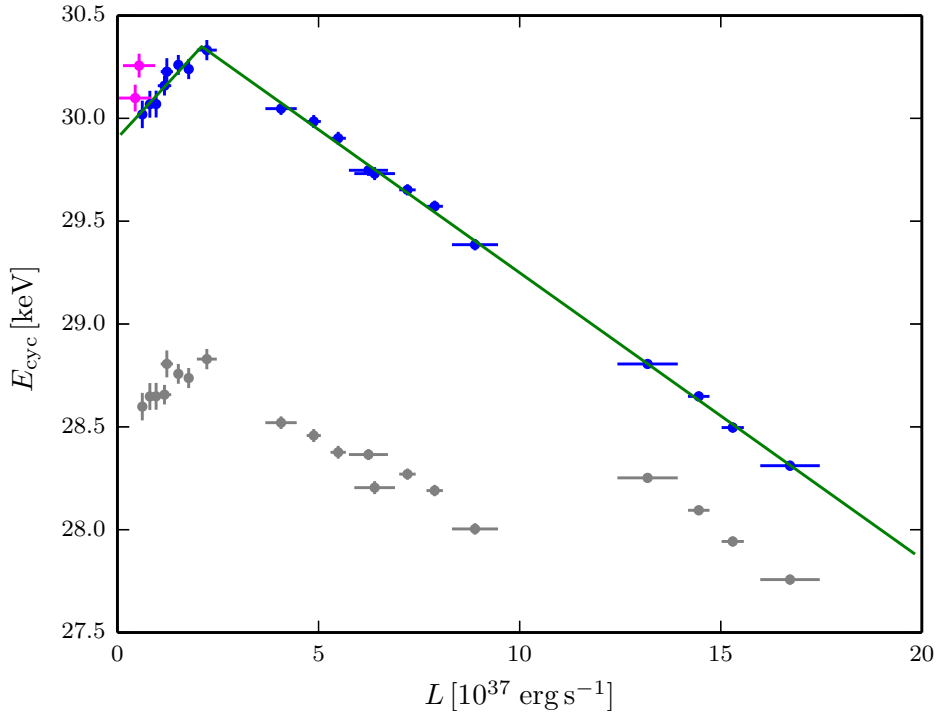
Figure 4.8: Observed correlations between the fundamental cyclotron line energy and luminosity as a result of the pulse-amplitude-resolved analysis (gray crosses). The blue crosses are the correlations corrected for the time drift. The green line is the best fit model to the blue crosses, which reflect the E_{cyc}/L_x dependence corrected for the time drift. The reference time corresponds to the beginning of the giant outburst. The data of the 2016 outburst are marked as the magenta crosses.

that there is a connection between these two events. The significance of the break in the linear drift of the cyclotron energy can be estimated, for instance, using the multiple linear regression (MLR) test (Protassov et al. 2002). The linear fit to the 2016 data gives $\chi^2 \sim 9$ for three degrees of freedom, whereas the statistics improve to $\chi^2 \sim 0.63$ for two degrees of freedom using the broken linear model. The more complex model is thus preferred at a $\sim 99.6\%$ confidence level based on the MLR test. One can also assume that the break time coincides with the accretion regime transition and estimate the slopes before and after the break, which are -0.016(1) and 0.02(3), i.e., they differ at a $\sim 90\%$ confidence level.

4.5 Discussion

A possible transition from a negative to a positive E_{cyc}/L_x correlation has been reported by Doroshenko et al. (2017) based on the analysis of averaged NuSTAR and Swift/BAT spectra. This transition likely reflects the change in the accretion regime from super- to subcritical. This conclusion, however, is hampered to some extent by a generally complex evolution of the line energy throughout the 2015 outburst because of a peculiar gradual decay, by uncertainties in the energy cross-calibration of Swift/BAT and NuSTAR, and the
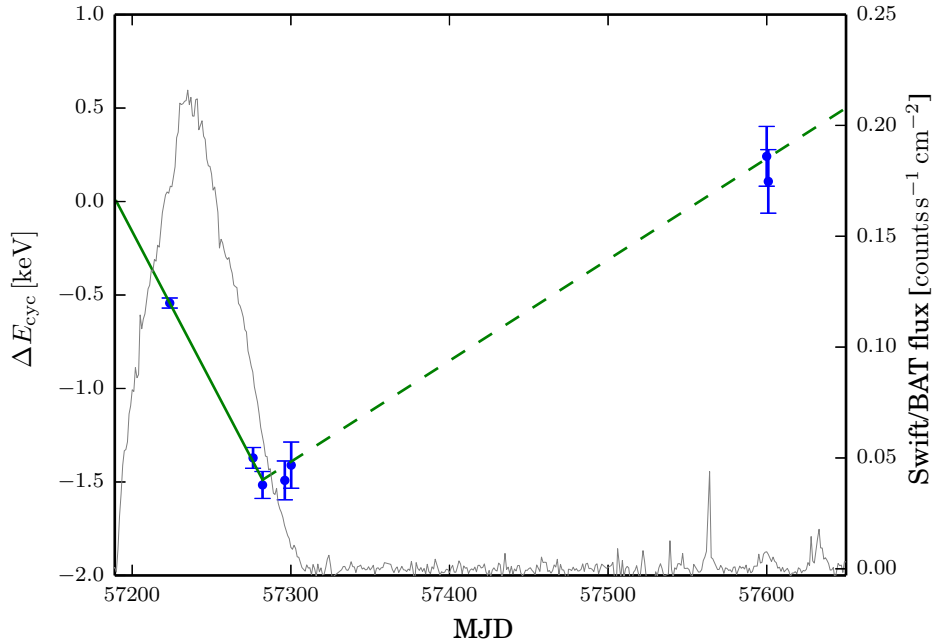
Figure 4.9: Energy offsets (blue bars) due to the time drift modeled as a broken linear function (green line). The offsets are measured from the beginning of the giant outburst (T_0 = 57190.0 MJD). The gray line is the 15-50 keV Swift/BAT time profile similar to that in Fig. 4.1.

low number of observations below the transition. As a result, the statistical significance of the observed transition in Doroshenko et al. (2017) was fairly low.

To confirm or refute the presence of the transition, we carefully analyzed the evolution of the cyclotron line during the 2015 and 2016 outbursts by applying the pulse-amplitude-resolved spectral analysis using NuSTAR data alone. Using data of a single instrument we avoid uncertainties related to cross-calibration issues. This approach also allows us to decouple the time dependence of the line energy from changes related to luminosity by obtaining E_{cyc}/L_x correlations measured on short timescales. As shown above, the slopes of the short timescale correlations were found to be the same as those measured on long timescales, i.e., the long-term decay of the line and flux-related variations are indeed independent.

Our analysis also revealed that the linear decay of the line energy reported in Doroshenko et al. (2017) seems to flatten out at later stages of the 2015 outburst when the source became too faint to be observed by Swift/BAT. The break occurred around MJD ~ 57282, which is very close to the transition from the super- to subcritical accretion regime, suggesting that these two events might be related. In this context, the break of the line decay could be associated with a transformation of the radiation-supported accretion column into an optically thin accretion mound, which should be present in the subcritical regime.

Moreover, by the 2016 outburst the cyclotron line energy rebounded to the values found at the beginning of the 2015 outburst (Fig. 4.9). If changes in the intrinsic magnetic field were responsible for the time evolution of the cyclotron line, as suggested by (Cusumano et al. 2016), it would imply an increase in the magnetospheric radius in

2016. Unfortunately, we could not estimate the magnetosphere size at later stages of the 2015 outburst or for the 2016 outburst using the observed spin-up rates as suggested in Doroshenko et al. (2017) because the spin-up rate could not be constrained due to the small time span between the two observations and insufficient counting statistics.

However, the effective magnetospheric radius has been reported to correlate with a high-frequency cutoff in the power density spectrum (PDS) of flux fluctuations (Revnivtsev et al. 2009; Doroshenko et al. 2014). A power density spectrum is the square of the amplitude of the Fourier coefficient of a given signal, which is the light curve in our case. Indeed, the nonperiodic flux variability is believed to be due to accretion rate fluctuations throughout the accretion disk on local Keplerian timescales (Lyubarskii 1997), so that the high-frequency cutoff in the PDS is associated with the truncation of the accretion disk by the magnetosphere, which is expected to occur close to the local Keplerian frequency at the inner edge of the disk (Revnivtsev et al. 2009; Doroshenko et al. 2014). A higher frequency of the cutoff thus corresponds to a smaller radius of the inner disk edge and the magnetosphere at a given accretion rate. The analysis of the PDS thus provides an alternative probe for the effective magnetosphere radius.
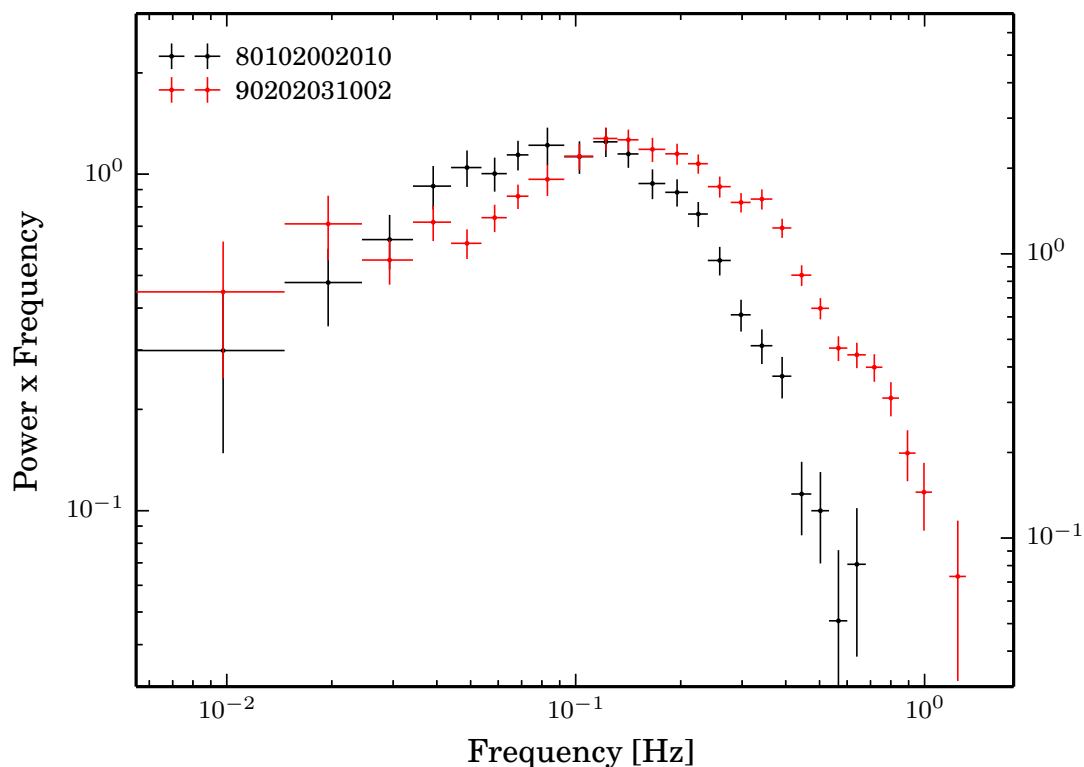

Figure 4.10: NuSTAR power density spectra of V 0332+53 of the last 2015 observation (black crosses) and the first observation of the 2016 outburst (red crosses). The apparent excess at high frequencies is clearly seen in the spectrum of the 2016 observation, suggesting a decrease in the effective magnetospheric radius between the outbursts. The power spectra were built with the `powspec` utility from HEASoft using the Leahy normalization (Leahy et al. 1983) with white noise subtraction.

To obtain the power density spectra in the last 2015 NuSTAR observation and the first 2016 observation, the same light curves, which were used to produce the pulse profiles, are used as an input for the `powspec` utility from HEASoft. This tool computes power density spectra either by a fast Fourier transformation algorithm or a direct slow Fourier algorithm. Derived Fourier coefficients must be normalized, and `powspec` provides a few ways to do it. We use the normalization, known as the Leahy normalization, suggested by (Leahy et al. 1983). In this case the spectral power is expressed as it follows

$$P_i = \frac{2A_i^2}{N},\tag{4.3}$$

where A_i is the Fourier amplitude of the i-th harmonic and N is the number of photons in the light curve interval where the power spectrum is calculated. The main feature of this normalization is that, for the Poisson noise with N much greater than unity, the mean value of spectral power $\bar{P}_i = 2$ at all frequencies. Thus, if the signal contains an intrinsic periodicity, the spectral power should be greater than two.

However, if the dead time effect is significant in the observations used for building of power spectra, it introduces a spurious noise since photon registration is no longer a Poisson process. This is reflected in a distortion of the power density spectrum, making it difficult to subtract the background noise level. A comprehensive investigation of the dead time influence on a timing analysis of NuSTAR data is given in Bachetti et al. (2015). Fortunately, although the first three NuSTAR observations of the 2015 outburst suffer of the dead time effect, in the last two observations in 2015 as well as the observations of the 2016 outburst the dead-time effect can be neglected since it is pronounced at incident count rates $\gtrsim 100$ counts per second.

It was verified that the white noise level corresponds to the the expected power of two in the both observations, i.e. it is not distorted by dead time effect or any other instrumental effects. The obtained power density spectra are present in Fig. 4.10, where the y-axis represents a spectral power in terms of the Leahy normalization with a white noise subtraction (normalization=-1 in `powspec`) multiplied by frequency.

Significantly higher frequencies of the variability in 2016 compared to 2015 at similar luminosities reflect a smaller effective magnetospheric radius during the 2016 outburst. This contradicts the idea that changes in the intrinsic magnetic field are responsible for the time evolution of the line energy sustaining the argumentation from Doroshenko et al. (2017). Thus, the observed rebound of the line energy between the outbursts is most likely related to changes in the emission region configuration in this case as well.

In particular, a smaller magnetosphere corresponds to a larger area of the polar region where the cyclotron line is believed to form because it depends on the effective magnetospheric radius R_{m} as $1/R_{\mathrm{m}}$. Since the source was in the subcritical regime during the last two observations of the 2015 giant outburst and during the 2016 outburst, the shock is no longer radiatively dominated and the infalling matter decelerates at some height either via Coulomb interactions (Staubert et al. 2007, 2014, 2016) or in a collisionless shock above the surface, which is supposed to form due to collective effects in the plasma (Langer & Rappaport 1982; Bykov & Krasilshchikov 2004), leading to a positive $E_{\mathrm{cyc}}/L_{\mathrm{X}}$ correlation.

The CRSF is thought to arise mostly in the vicinity of the collisionless shock whose height is proportional to the electron density in the emission region (Shapiro & Salpeter
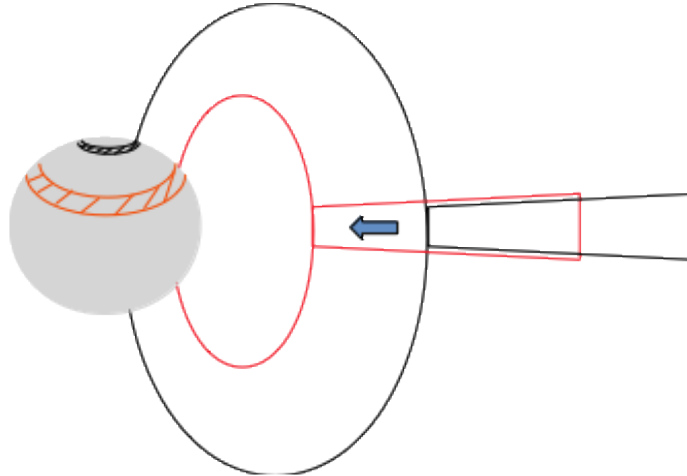
Figure 4.11: Sketch to the interpretation of the cyclotron line energy rebound by the 2016 outburst as a result of the accretion disk movement resulting in changing of the magnetosphere size. The black line corresponds to the state at the tail of the 2015 outburst, whereas the red line show the state in the 2016 outburst.

1975). This model was successfully applied to interpret the $E_{\mathrm{cyc}}/L_{\mathrm{X}}$ correlations in Cep X-4 (Vybornov et al. 2017) and GX 304-1 (Rothschild et al. 2017) as well as the change in a spectral hardness in Cep X-4 (Vybornov et al. 2017). As discussed above, the PDSs point to a larger polar cap area in the 2016 observations at a luminosity comparable to that found during the two last observations in 2015, implying a lower electron density in the emission region in 2016. This is expected to reduce the height of the collisionless shock and thus to increase the CRSF energy as observed.

An alternative model suggested by Mushtukov et al. (2015c) to explain a $E_{\mathrm{cyc}}/L_{\mathrm{X}}$ correlation in subcritical sources relates the observed changes in cyclotron line energy to the Doppler effect associated with the bulk motion of the accreting flow in the vicinity of the neutron star surface. In this model the observed CRSF appears red-shifted by an amount proportional to the accretion flow velocity, which is expected to decrease with higher accretion rate, so that the line energy appears to be correlated with luminosity. Since the local electron density decreases with the increasing polar cap area at a given mass accretion rate, the flow velocity in the vicinity of the hot spot is expected to increase according to this model, i.e., for V 0332+53 one could expect a higher flow velocity and a lower line energy in the 2016 outburst, which does not agree with observations.

For V 0332+53, the observed rebound of the cyclotron line energy by the 2016 outburst is therefore explained rather with the collisionless shock model. We note, however, that the Doppler effect must still play a role also in this case, and should be taken into account. We conclude, therefore, that the results presented here can be very useful for the further development and verification of these models.

4.6 Conclusions

Using NuSTAR observations of the Be-transient X-ray pulsar V 0332+53 carried out during a giant outburst in 2015, and a subsequent ordinary outburst in 2016, we investigated

for the first time the dependence of the CRSF centroid energy on luminosity both on long (months) and short (seconds) timescales using the pulse-to-pulse analysis technique.

We found that the dependence is essentially the same on both timescales and confirmed with high significance the reported transition from an anti-correlation to a correlation at $L_{cr} = (2.1 \pm 0.4) \times 10^{37}$ erg/s, which is likely associated with the transition between the super- and subcritical accretion regimes defined according to the presence/absence of the radiation-supported accretion column.

We also found that the time-linear decay during the 2015 outburst is likely to break up at the transition between the two types of the E_{cyc}/L_X correlation, which could be associated with changes in the accretion structure above the polar cap caused by switching between the super- and subcritical accretion regimes.

The line energy then rebounded between the 2015 and 2016 outbursts to values observed at the beginning of the giant outburst. We argue that this change is also likely related to a change in the geometrical configuration of the emission region. This conclusion is supported by the analysis of power density spectra of nonperiodic flux fluctuations, which exhibits variability at a significantly higher frequency in the 2016 outburst compared with the decay phase of the 2015 outburst. We interpret this as an evidence of a smaller truncation radius of the accretion disk, and as a result, a smaller magnetosphere in 2016. We briefly discuss how such a change is expected to affect the observed line energy in the framework of the model proposed by Mushtukov et al. (2015c) and the model with a collisionless shock (Rothschild et al. 2017; Vybornov et al. 2017). We conclude that the latter model more readily explains the observations.

We note that a long-term evolution has been reported before for Her X−1 (Staubert et al. 2014, 2016) and Vela X−1 (La Parola et al. 2016). In the case of V 0332+53, we argue that the observed time evolution of the CRSF energy is driven by changes in the geometry of the emission region.

5. Observations of Her X-1

5.1 Introduction

5.1.1 System overview

Hercules X-1 (Her X-1) is a well known and probably most investigated object among X-ray pulsars, which is why, to give a substantial overview of the object, the Introduction is divided into subsections. Her X-1 is together with Cen X-3 among first ever discovered X-ray pulsars. Her X-1 was discovered with *Uhuru* in 1972 (Tananbaum et al. 1972; Giacconi et al. 1973). The source was soon established to be a fast rotating magnetized neutron star emitting X-rays because of accretion, as understood from the periodicity of the detected light curve. The period of pulsations, the spin period of the neutron star, was found to be 1.24 s. Periodical deep drops in the light curve were interpreted to be eclipses, which also confirmed the binary nature of the source, as also indicated by the Doppler shift of the pulse arrival times.

The orbit is almost circular with an orbital period of 1.7 days and an eccentricity of about 0.0004 and inclined by ~ 84 degrees (the angle between the normal to the orbit's plane and the line of sight), i.e. a distant observer sees it almost edge-on (Gerend & Boynton 1976; Staubert et al. 2009). This orbit's orientation produces of the regular 5.5-hours eclipses of the X-ray source by the optical companion. In addition to this variable behaviour, the X-ray light curve exhibits a strong modulation with a superorbital period of about 35 days, which manifests itself in the alternation of states with high X-ray flux (on-states) and states with low X-ray flux (off-states). During every 35-day superorbital cycle two on-states are observed, namely the *main-on* lasting around 7 orbital periods and *short-on* containing ~5 orbital periods (Fig. 5.2). At the maximum of the main-on the X-ray intensity is about five times higher than that in the maximum of the short-on. Between the on-states the X-ray flux usually drops for ~4-5 orbital periods, but sometimes the source, in fact, stays in the off-state for a so long time that the 35-day periodicity can hardly be traced (Parmar et al. 1999). These rare states occur every 5-10 years and are sometimes called the *anomalous lows*. While the presence of the main-on state was discovered during first *Uhuru* observations, the short-on was detected with the *Copernicus* mission a bit later (Fabian 1973).

The transition from the off-state to the on-state is characterized by a short time, from 1.2 to 2 orbital cycles. In the case of the main-on, this rise phase is called the X-ray turn-on of the source and is usually used as a phase zero for counting of superorbital cycles. The rise phase of the short-on state is sometimes referred to as the secondary turn-on. The main-on begins, by definition, at a phase of 0 and fades away at $\phi_{35d} = 0.31$, whereas the short-on covers phases $\phi_{35d} = 0.56 - 0.76$ (Scott & Leahy 1999). It is important to note
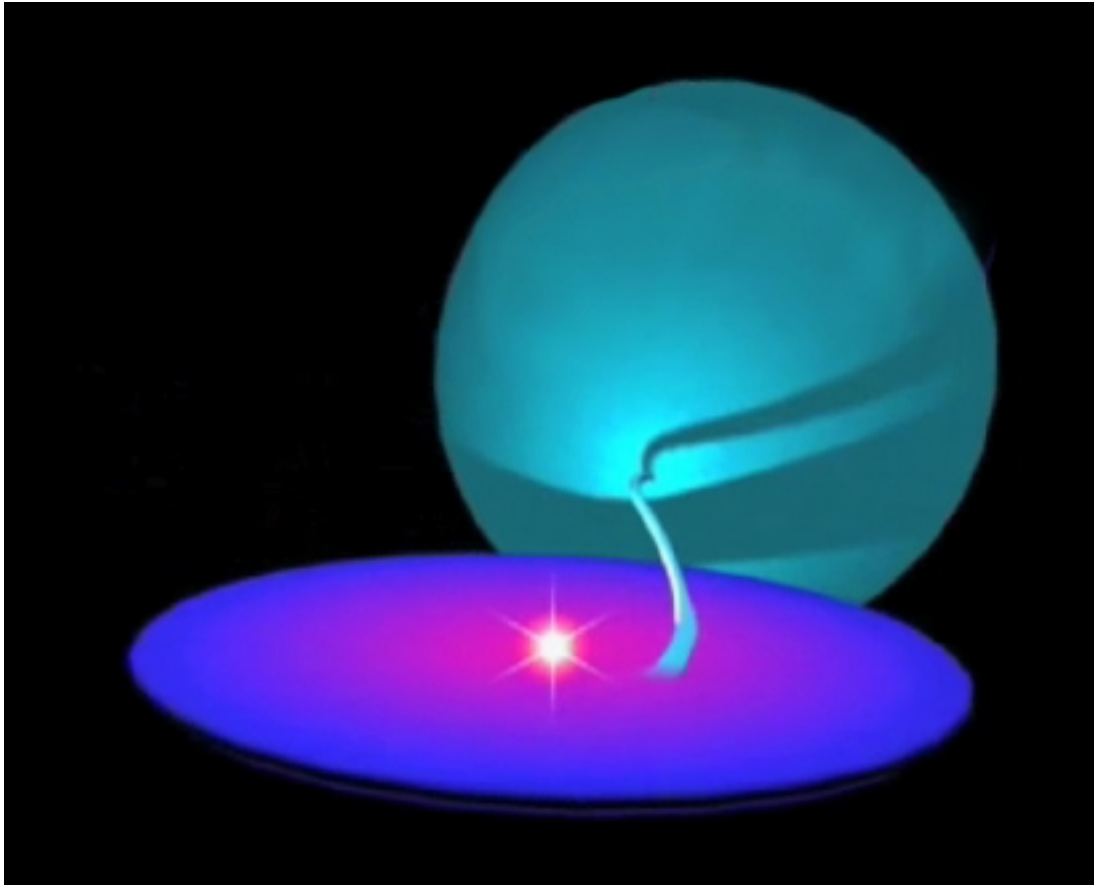
Figure 5.1: Representation of the binary system containing the Her X-1 accreting pulsar and HZ Her, the optical component. The neutron star is believed to posses a prominent accretion disk, which is precessing, being a cause of the 35d superorbital period. The X-rays coming from the neutron star poles illuminate and heat the surface of the normal star on the side facing the pulsar. Credit: D. Klochkov.

that turn-ons occur at certain orbital phases $\phi_{orb} = 0.2, 0.7$, which results in the duration variation of the 35-day cycle, so that it lasts 20, 20.5 or 21 orbital periods (Staubert et al. 1983). This behaviour is probably caused by quasi-periodic variations with a period of around several years in the mass transfer between the normal companion and the accretion disk since the duration of the 35-day superorbital cycle is correlated with the spin-up of the neutron star on long time scales of ∼2000 days (Staubert et al. 2000, 2006).

In addition to the 35-day superorbital modulation, drops of X-ray flux due to eclipses and X-ray dips are observed during the on-states. While X-ray drops due to eclipses are a common feature of binary systems, the origin of the X-ray dips is still poorly understood. The X-ray dips in the Her X-1 light curve are usually distinguished: pre-eclipse dips being followed by eclipses at orbital phases of 0.6-0.9 and tending to move to earlier orbital phases due to their period of about 1.62 days (a beat frequency between 35d and 1.7d); post-eclipse dips, which are sometimes observed as a few hour delay after the first eclipse in the turn-on and anomalous dips, which occur randomly within the orbital phase interval $\phi = 0.45 - 0.65$ during the first one or two orbital cycles after turn-on. The average duration of the dips is comparable to that of eclipses (∼5.5 hours). The X-ray

dips are characterized not only by a sudden decrease of the X-ray flux, but the spectrum also undergoes significant changes, in particular, at low energies due to high photoelectric absorption with a typical column density of $\sim 10^{23}$ cm^{-1} (Giacconi et al. 1973).
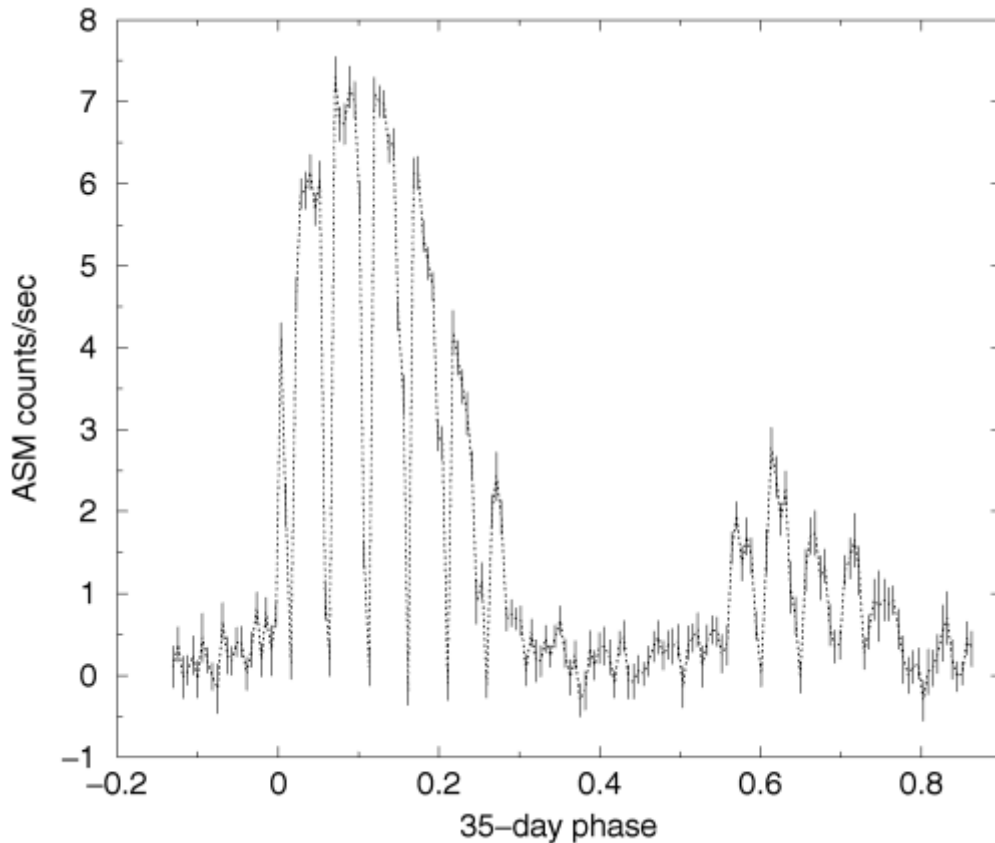

Figure 5.2: Light curve of the 35-day superorbital cycle of Her X-1 obtained with RXTE/ASM. Source: Leahy (2002).

The donor component in the X-ray binary is a main sequence star, known as HZ Her, whose optical luminosity is modulated with a period of around 1.7 days (Kurochkin 1972; Boynton et al. 1973). The optical spectrum also varies from the late A type to the B type (Liller 1972; Crampton & Hutchings 1974) with the same period. The effective temperatures of the optical component lie between 8000 and 9500 K, which corresponds to a stellar mass of about 2 $M_\odot$, placing this system between HMXBs and LMXBs (Reynolds et al. 1997). The optical spectrum and temperature variability are attributed to the illumination and heating of the part of the normal star atmosphere by X-rays coming from the pulsar (Middleditch 1983). Because of the binary system rotation with an orbital period of around 1.7 days, a distant observer sees the color and spectrum modulations with this period. In addition to the 1.7-day period, Boynton et al. (1973) reported a clear variation of the optical light curve in the B filter with the 35-day superorbital period. Thus, the main properties of the X-ray light curve are in many ways reflected in the optical light curve.

The X-ray source does not exhibit any flare activity and is considered to be persistent. However, as shown in Fig. 5.2, the X-ray intensity shows a sufficiently complicated light curve. Because of such complicated behaviour of the X-ray and optical properties, Her X-
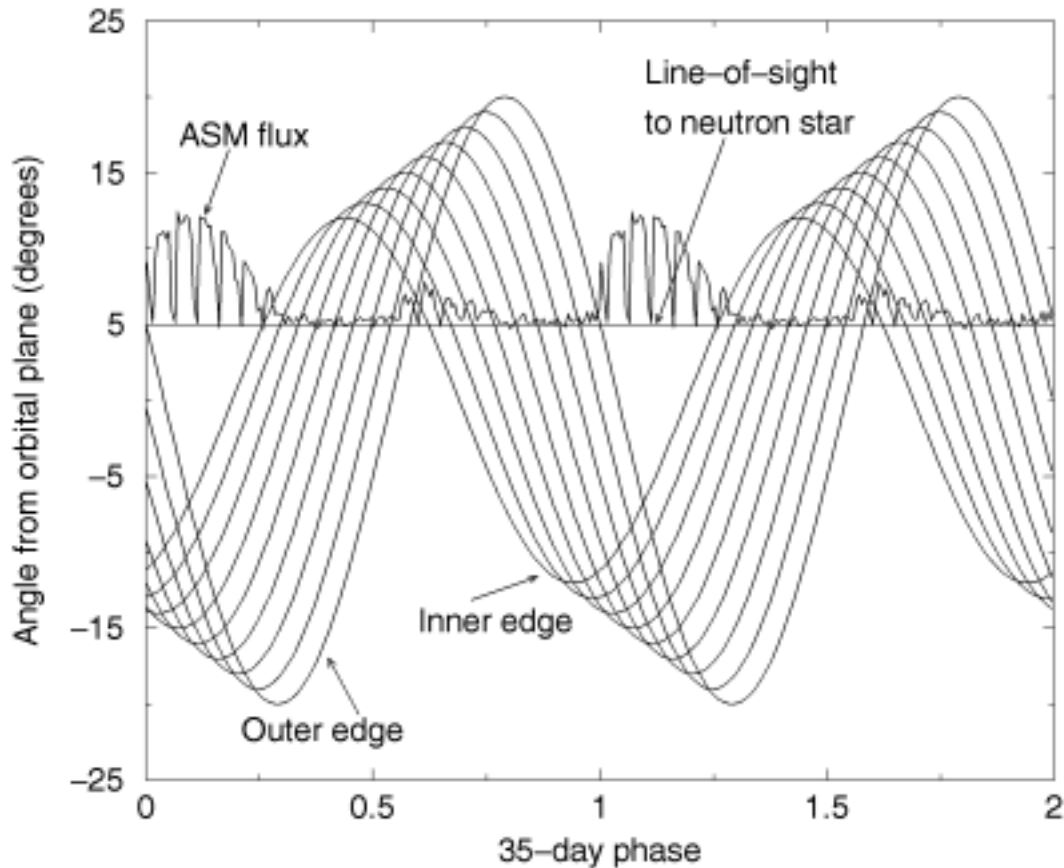
Figure 5.3: Appearance of the X-ray source as a function of the 35-day phase owing to the accretion disk precession as the observer sees it from the direction inclined by 5 degrees to the orbital plane (i.e the line of sight is perpendicular to the figure plane and directed along the horizontal line at 5 degrees) according to Leahy (2002). The sinusoidal lines show several disk rings. The tilt of the outer rim is 20 degrees, while the tilt of the inner edge is 11 degrees. Source: Leahy (2002).

1 is always very interesting to be explored, and due to its brightness, it has been observed many times with different instruments, so that a large amount of data is available today. It allows astronomers to build a general picture of the binary system and shed light on the origin of the flux and spectrum variability.

The presence of the accretion disk around the neutron star plays a key role in such a complicated temporal behaviour. Precessing oppositely to the direction of the orbital motion, the tilted and warped disk periodically obscures the X-ray source, causing the 35-day superperiodical modulation. As the disk precesses, its outer rim crosses the line of sight and uncovers the neutron star. This corresponds to the turn-on at the beginning of the main-on state. The subsequent drop of the observed X-ray flux at the end of the main-on could be explained with covering the neutron star by the inner part of the disk (Fig. 5.3).

The presence of the short-on states could likewise be interpreted, taking into account that the amplitude of the X-ray flux in the short-on is lower because of the inclination of the disk's plane to the line of sigh, which is likely an effect of the orbit's plane inclination

81

(Petterson 1975, 1977; Scott et al. 2000). Such a scenario seems to be confirmed by spectral changes in turn-ons and decay phases, namely the soft part of the X-ray spectrum is suppressed in the turn-on, implying a photo-electric absorption in the outer part of the accretion disk. The decrease of the X-ray intensity during the decay phase of the on-states is not accompanied by notable spectral changes (Kuster et al. 2005).

The presence of the X-ray dips in the X-ray light curve can be explained with the stream-disk coupling model suggested by Shakura et al. (1999). In this model, a tilted twisted precessing accretion disk eclipses the X-ray source, producing a shadow on some part of the optical component surface. The photospheric temperature of the region illuminated by X-rays is up to 20000, while the photospheric temperature of shadowed region is about 8400 K. This high temperature difference leads to the emergence of powerful pressure gradients at the boundary separating illuminated and shadowed parts. Such gradients induce large-scale motions of matter near the inner Lagrangian point perpendicular to the orbital plane. As a result, matter flows non-coplanar with the orbital plane, and streams cross the line of sight shortly before eclipses of the X-ray source, which is observed as the pre-eclipse X-ray dips. Tidal forces and the dynamics of the matter stream produce the disk wobbling, which may be the cause of the obscuration of X-rays by the disk after the turn-on, explaining anomalous and post-eclipse X-ray dips both in main-ons and short-ons. A nice animation illustrating the shape of the Her X-1 X-ray light curve is available here [1].

The presence of a counter precessing accretion disk is also confirmed by optical observations. Gerend & Boynton (1976) showed that to explain and reproduce the optical light curve obtained by Deeter et al. (1976), a combination of several factors is needed, namely an accretion disk, which precesses oppositely to the orbital motion and emits optical radiation, and the occultation of the optical component by this disk. Theoretical calculations, carried out by Katz (1973), confirmed the accretion disk in this binary system should be tilted and precess in the retrograde direction.

Given a distance of about 7 kpc, found by Reynolds et al. (1997), the X-ray luminosity of the pulsar L_X is estimated to be $\sim 2 \times 10^{37}$ erg/s, which corresponds to a mass accretion rate of about 2×10^{17} g/s (assuming an efficiency of the accretion onto the neutron star of around 10%). The recent GAIA release gives a value of 6.7 ± 1.2 kpc, which is compatible with previous measurements (Treuz et al. 2018).

5.1.2 Pulse profile

The pulse profile of an X-ray pulsar is the flux dependence on rotational phase of the neutron star. To build the pulse profile, the X-ray curve has to be barycenter and binary corrected as well as other instrumental effects such as dead-time, pile-up should be taken into account.

The magnetic field of the neutron star is so high that the plasma pressure is dominated by magnetic pressure, so that the accreted plasma turns out to be frozen and can flow only along the magnetic field lines towards magnetic poles where it decelerates accompanied by X-ray emission. Since the rotation and magnetic axes of the neutron star do not coincide, and the X-ray emission is localized in the magnetic pole regions, pulse profiles of X-ray pulsars normally consist of one or two prominent peaks. In spite of this, the

---

[1]http://sci.esa.int/integral/42947-hz-her-her-x-1-binary-system-and-the-35d-light-curve
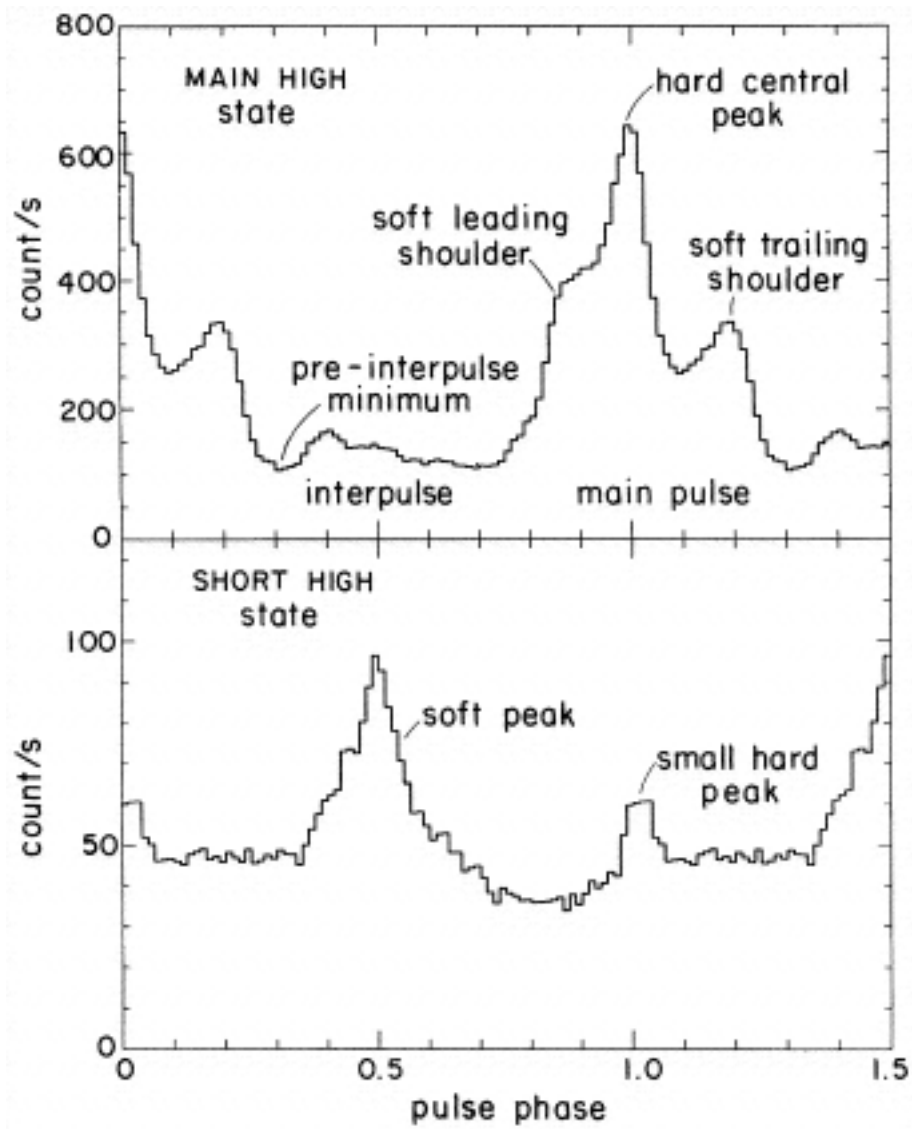
Figure 5.4: Ginga pulse profile in the 9.4-14 keV energy band, taken in main-on (top) and short-on (bottom) states. The nomenclature of typical pulse features is also presented. Source: Deeter et al. (1998).
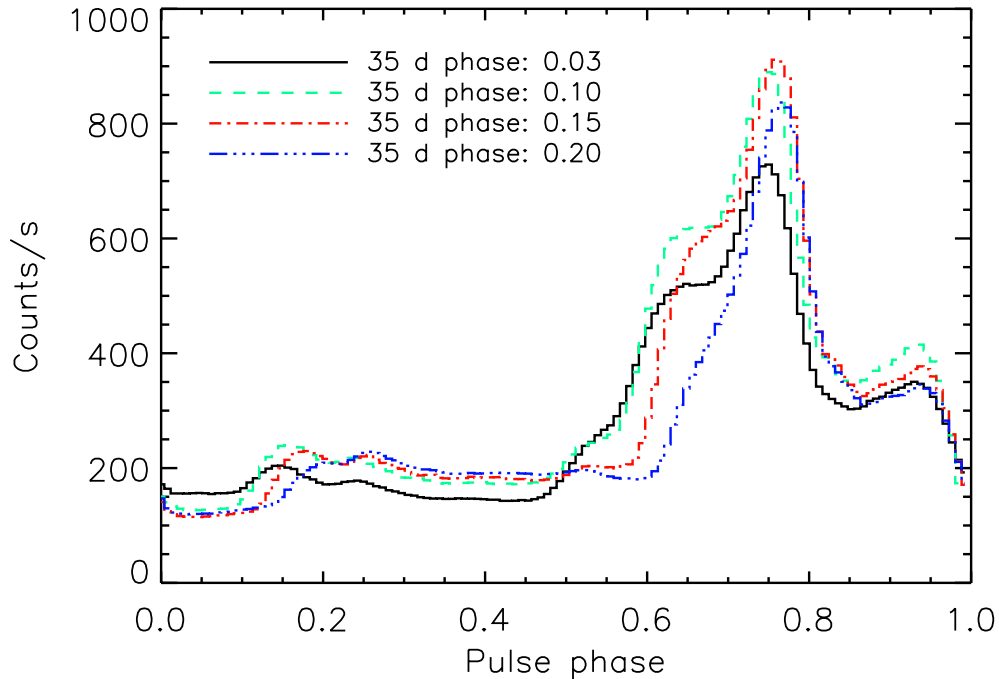
Figure 5.5: 9-13 keV RXTE pulse profile of Her X-1 during a main-on high state as a function of 35-day phase. As the X-ray source evolves with the 35-day phase, the leading shoulder disappears, whereas the central hard peak remains. The shape of the trailing shoulder also remains stable and is used as a reference point for pulse phase zero. Note that both the central peak and the interpulse are slightly shifted with the 35-day phase. This behaviour of the Her X-1 pulse profile is assumed to be attributed to precession of the tilted and twisted accretion disk. Source: Vasco et al. (2013).

shapes of pulse profile are diverse, substantially varying from source to source. The pulse profile of an X-ray pulsar depends on energy and can evolve in time, providing important information on the geometry of the emission region as well as on properties of accretion processes.

Her X-1 shows two different pulse profiles during main-on and short-on. Although there is changing with energy, the typical X-ray pulse profile of Her X-1 during main-on as well as short-on has characteristic shapes, which are sufficiently stable and recognizable. In main-on the pulse profile consists of a hard central peak with two soft shoulders, and a minor peak, or interpulse, approximately half of the spin cycle from the main peak. In short-on the main peak appears at the phase of the interpulse in main-on is, implying the alternating obscuration of the two emitting regions by the accretion disk (Fig. 5.4).

The pulse profile evolves with the 35-day phase both during main-on and short-on state. Since main-on states are more studied because they are brighter than short-on states, the phase evolution is most apparent in main-on state, as shown in Fig. 5.5, which represents RXTE pulse profiles obtained by Vasco et al. (2013). It is clearly seen that the soft leading shoulder taking place in turn-on disappears as X-ray flux fades out. The shape of the pulse profile of the short-on also varies with superorbital phase (Fig. 5.6, bottom panels). The shape of the main peak changes not significantly during short-on, whereas the hard small peak disappears after two orbital cycles.
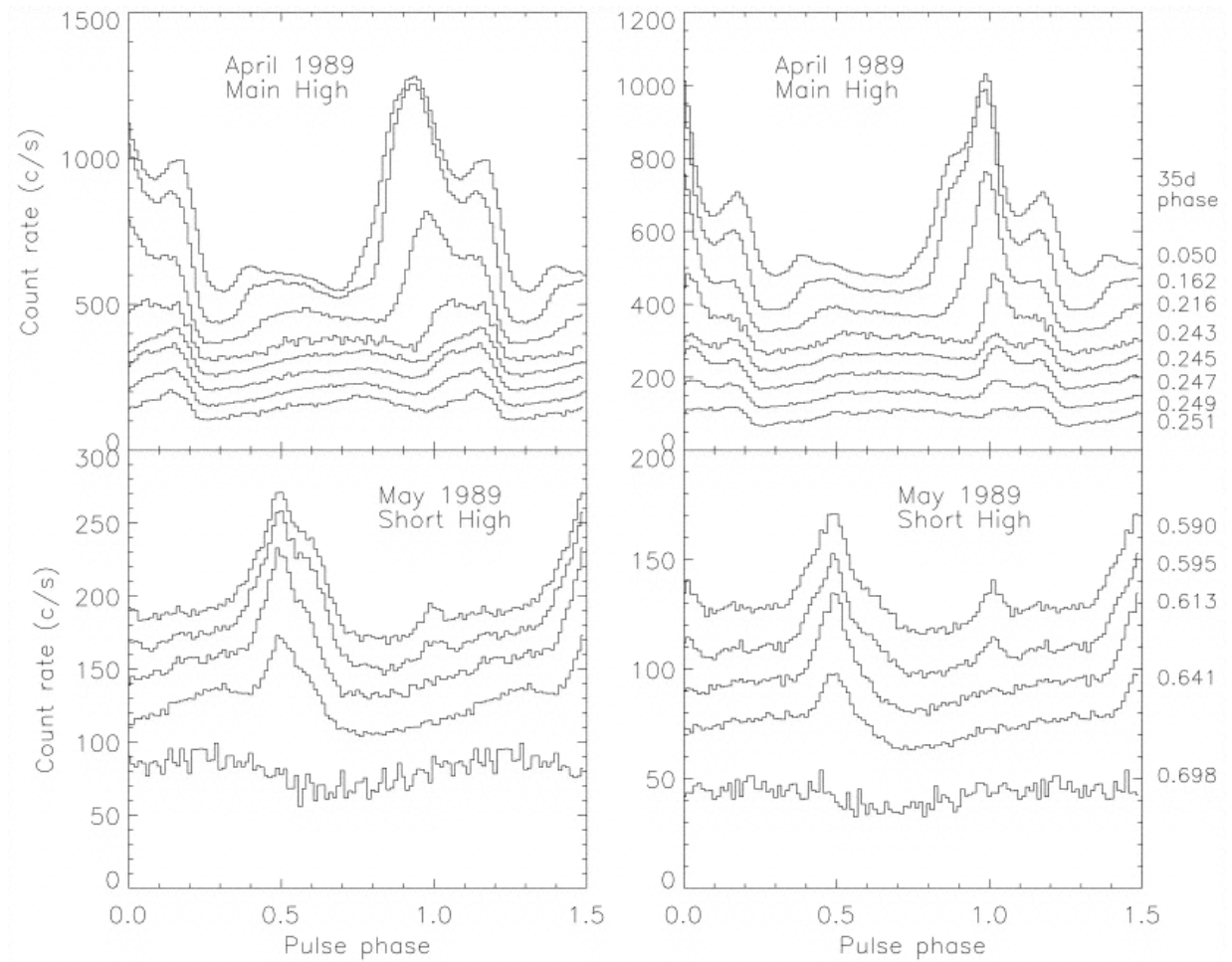
Figure 5.6: Observations of the time evolution of the Her X-1 pulse profile during the main-on state (top panels) and short-on state (bottom panels) obtained by (Scott et al. 2000). The left and right panels show pulse profiles in the 1.0- 4.6 keV and 9.3–14 keV energy band, respectively. Source: Scott et al. (2000).

Moreover, the whole structure of the pulse profiles both during main-on and short-on tends to shifts with time to higher phases. Such behaviour could be explained either in terms of the free precession model of the neutron star suggested by Postnov et al. (2013), or with an inclined warped counter-precessing accretion disk, which gradually shields X-ray emitting regions during its precessing (Staubert et al. 2013). While the former model demands some specific assumptions, such as multipolarity of the neutron star magnetic field and a narrow pencil radiation beam, the latter approach does not need any physics assumptions. It should be noted that the role of the accretion disk for pulse profile shape changes has also been earlier proposed by Petterson et al. (1991). The accretion disk thus seems to be responsible for the evolution of the pulse profile with time.

In addition to the variation with the 35-day phase, the shape of the Her X-1 pulse profile also depends on energy. The left panels of Fig. 5.6 represents observations in the 1.0-4.6 keV energy band, whereas on the right side the pulse profile is in the 9.3-14 keV energy band. As it can be seen, the shape of the main pulse changes significantly with energy, mainly because of the decay of the soft leading shoulder. Note that the trailing shoulder does not change significantly with energy, in particular the position of its right edge, which is often taken as a reference point in time analysis using the phase-connection method (Staubert et al. 2009). The pulse profile in short high state, instead, remains relatively stable, without significant changes in shape of the major and minor peak with increasing energy.

5.1.3 Spectrum

The continuum of the Her X-1 spectrum is typically described with a phenomenological model, as most continua of other accreting pulsars. Although there were a number of attempts to explain continua of X-ray pulsars (see i.e. Becker & Wolff (2007)), there is still not a generally accepted physical model explaining the production of hard X-ray emission in the accretion mound. All phenomenological models include a power law with a slope index Γ and a high-energy cutoff at E_{cut} with a folding energy E_{fold}.

Typical models used in the case of Her X-1 observations include a Fermi–Dirac cutoff (`fdcut`, Tanaka 1986), an exponential cut-off (`highecut`, White et al. 1983) or a negative–positive exponential cutoff (`NPEX`, Makishima et al. 1999). Other phenomenological models used for modeling of accreting pulsar continua such as `cutoffpl`[2] and `comptt`[3] are not appropriate for Her X-1.

Regardless of instruments, the `highecut` model has been shown to be the preferable (in terms of χ^2) to describe the Her X-1 continuum (dal Fiume et al. 1998; Gruber et al. 2001; Klochkov et al. 2008; Fürst et al. 2013). However, this model has a peculiarity: the common continuum function consisting of the power-law and the exponential functions has a derivative discontinuity at E_{cut}, leading to the presence of a sharp feature in residuals at this energy (Kretschmar et al. 1997; Kreykenbohm et al. 1999). To smooth this feature, a multiplicative line with a Gaussian profile with the energy fixed to the cutoff energy is normally used (Coburn et al. 2002).

In addition to the `highecut` model, an additional component is needed to take into account the feature at about 40 keV (Fig. 5.7), interpreted as a cyclotron resonant scattering

---

[2]https://heasarc.gsfc.nasa.gov/xanadu/xspec/manual/XSmodelCutoffpl.html
[3]https://heasarc.gsfc.nasa.gov/xanadu/xspec/manual/node155.html
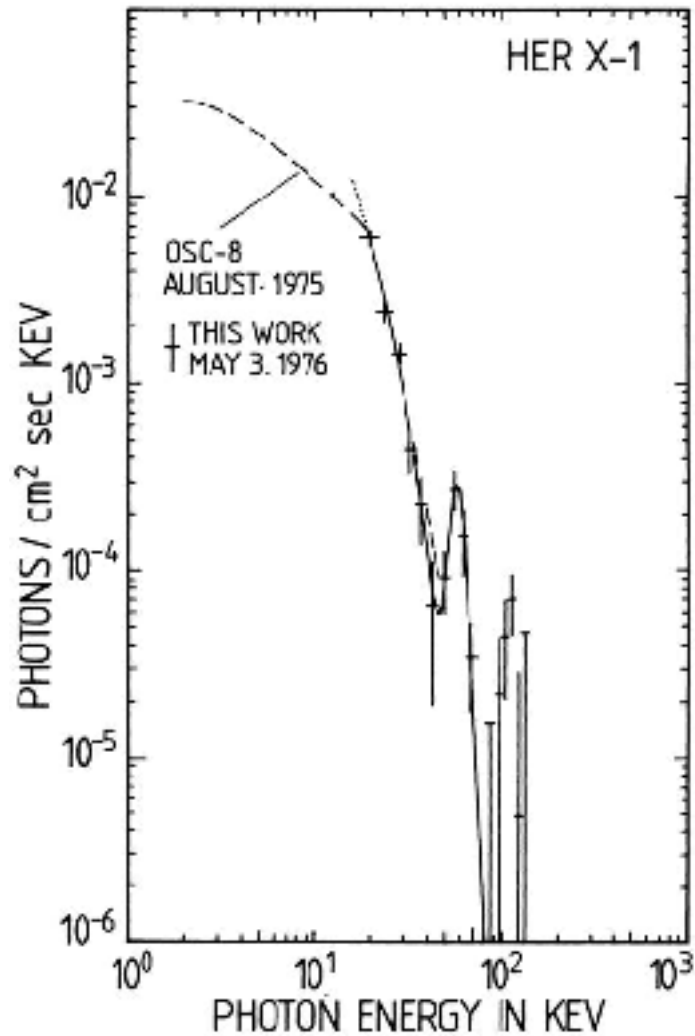
Figure 5.7: The first X-ray spectrum of Her X-1 with a presence of a feature at about 40 keV, interpreted as a cyclotron resonant scattering feature (CRSF). The dashed line is a result of the observations of a 1975 on-state by OSO-8, while the solid line represents a best-fit to the data taken during a balloon observations of the source carried out by Trümper et al. (1978) . Source: Trümper et al. (1978).
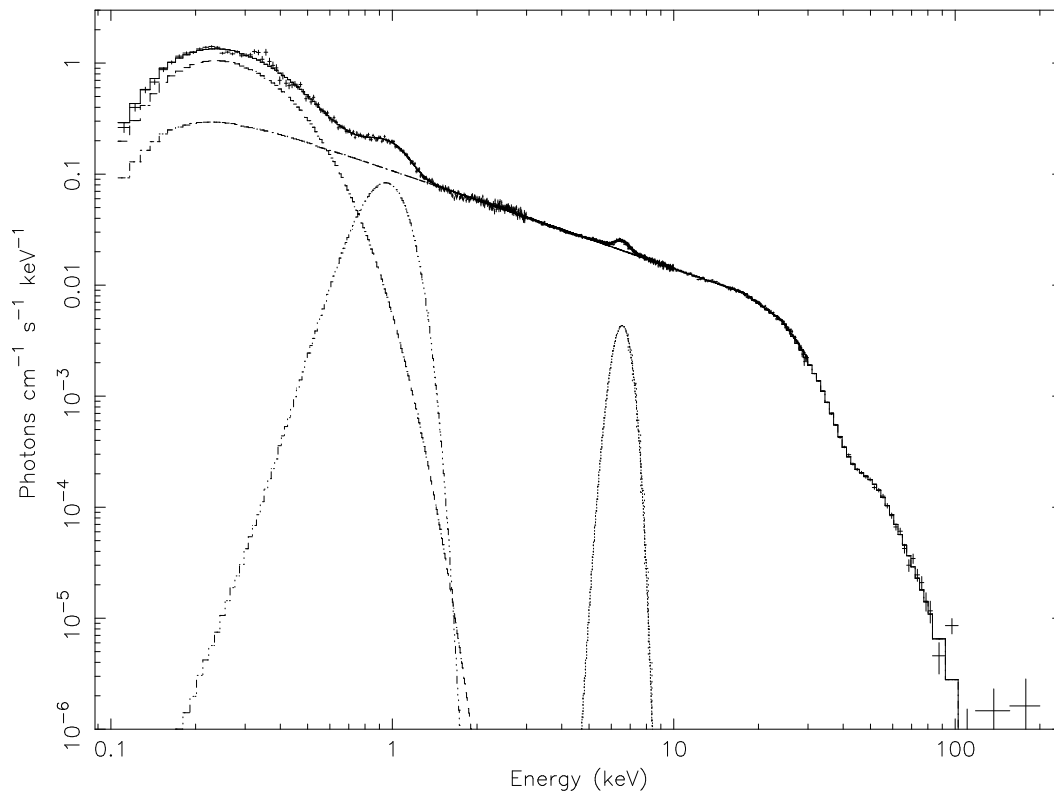
Figure 5.8: Broadband photon spectrum of Her X-1 taken with BeppoSAX in the 0.1-100 keV energy range. The dashed lines indicate distinct spectral components, which are used for fitting the spectrum. The soft bump is described by a 0.1 keV blackbody component; two Gaussian lines correspond to the Fe L and K lines at 1 keV an 6.4 keV, respectively; the continuum is fitted by a power law with a high energy cutoff. The cyclotron feature at around 40 keV is also seen. Source: dal Fiume et al. (1998).

feature (CRSF). The presence of a CRSF in the Her X-1 spectrum at around 40 keV was discovered during a balloon observation in 1976 (Trümper et al. 1978). Initially, it was not clear whether this feature was an absorption or an emission line, but later theoretical calculations (Nagel 1980) and observations (Kunz et al. 1996) showed that the cyclotron feature in accreting pulsars is in absorption. To model the CRSF in the Her X-1 spectrum, a multiplicative absorption line with a Gaussian optical-depth profile (`gabs`[4] in XSPEC) or with a pseudo-Lorentzian optical-depth profile (`cyclabs`[5] in XSPEC) are usually used. Knowing the centroid energy of the line, one can estimate the magnetic field of the emission region directly. In the case of Her X-1 the corresponding magnetic field in the region of the line formation is found to be about 3×10^{12} Gauss.

Since Her X-1 is a persistent and sufficiently bright X-ray source to be a good target for a huge number of observations with different missions. This allowed to carry a comprehensive study of various kinds of variabilities (dependencies on luminosity, pulse phase, secular variations, etc) of the whole spectrum as well as its distinct components. It is mostly interesting how the energy of the cyclotron line varies with time and luminosity, though the behavior of other spectral components and properties such as the iron line and

---

[4]https://heasarc.gsfc.nasa.gov/xanadu/xspec/manual/node232.html

[5]https://heasarc.gsfc.nasa.gov/xanadu/xspec/manual/node230.html

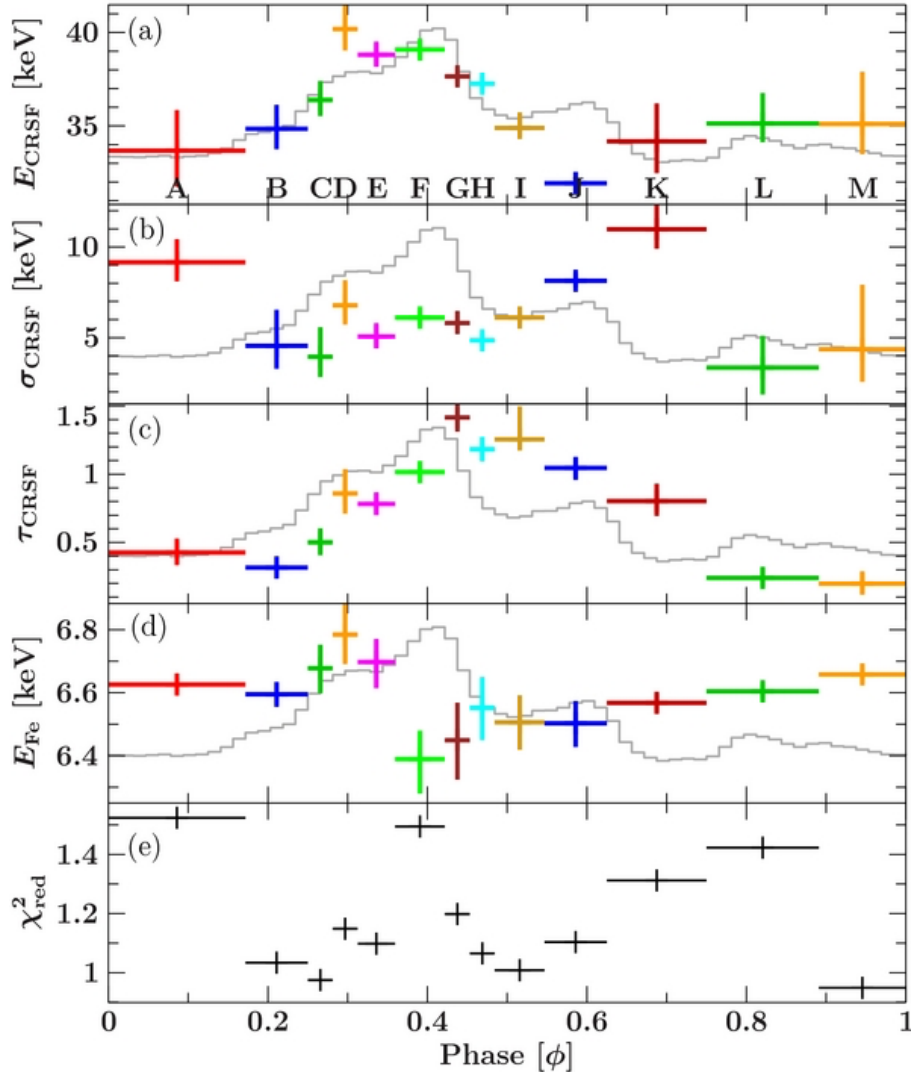hardness are also very informative.

Figure 5.9: Parameters of the cyclotron line (three top panels) and iron line (second from bottom) as function of pulse phase obtained by Fürst et al. (2013). The spectra were taken with NuSTAR during a main-on in 2012. The bottom panel indicates the fit quality of the model, used by the authors. The cyclotron feature is modeled as a line with a Gaussian optical-depth profile (`gabs` in XSPEC). The gray line in each panel is the pulse profile in the 9-13 keV energy band. The iron line is modeled as an additive Gaussian line. The figure is taken from Fürst et al. (2013).

The energy of the cyclotron line of Her X-1 has been found to change with time on several time scales, namely it depends on pulse phase, superorbital 35-day cycle phase and has also a long-term secular variation.

Figure 5.9 (top panel) shows the cyclotron line centroid energy as a function of pulse phase as observed with NuSTAR by Fürst et al. (2013). The other panels of Fig. 5.9 represent behaviour of other parameters of the cyclotron line, which was modeled as a `gabs` function, the energy of the iron line and quality of the best-fit function. As it can be seen, the cyclotron line energy changes considerably over the pulse profile, generally
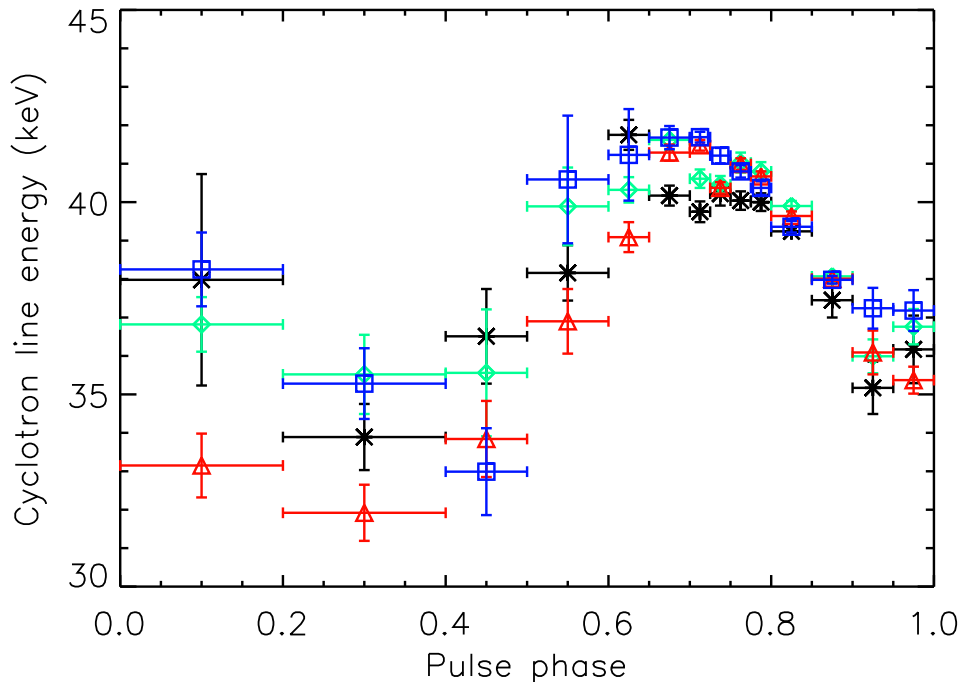
Figure 5.10: Cyclotron line centroid energy as a function of pulse phase at different phases of the 35-day cycle. Black, green, red and blue crosses correspond to mean 35-day phases 0.03, 0.10, 0.15 and 0.20, respectively. The figure is taken from Vasco et al. (2013).

following the shape of the 9-13 keV pulse profile. The energy maximum is reached near the peak of the pulse profile. One of the interpretations of this fact is that at this phase a distant observer looks right inside the column-like accretion structure, and the optical depth $\tau = 1$ at the cyclotron frequency is reached at lower heights (where the magnetic field is stronger) than at other phases of pulse profile. The optical depth, τ_{CRSF}, has a similar behaviour, becoming higher with higher flux, however with some phase shift. The width of the cyclotron line, σ_{CRSF}, in contrast, seems to become lower during the bright part of the pulse profile.

The dependence of the iron line is different: it shows a significant drop at the peak of the pulse profile. This drop seems to be associated with illumination of the part of the accretion disk that lies on the line of sight between the observer and the neutron star and, as a result, the observer does not see this part because of the obscurity by the outer parts of the accretion disk.

The 35-day dependence of the cyclotron line centroid energy generally remains sinusoidal-like over on-state (Fig. 5.10). However, as shown by Vasco et al. (2013) using RXTE data, there is a slight but significant difference between energies at the peak of the 9-13 keV pulse profile: the line energy increases with 35-day phase.

Another type of the cyclotron line energy variability is the long-term evolution over a few decades. As shown in Fig. 5.11, the energy of cyclotron line changes significantly and non-monotonically, undergoing a dramatic jump at the beginning of the 1990s. After that, the line energy was decaying gradually for 20 years, but the recent NuSTAR and Integral observations have shown that the decay has probably stopped in 2015-2016. This suggests that energy's rises and decays seem to alternate periodically on time scales of
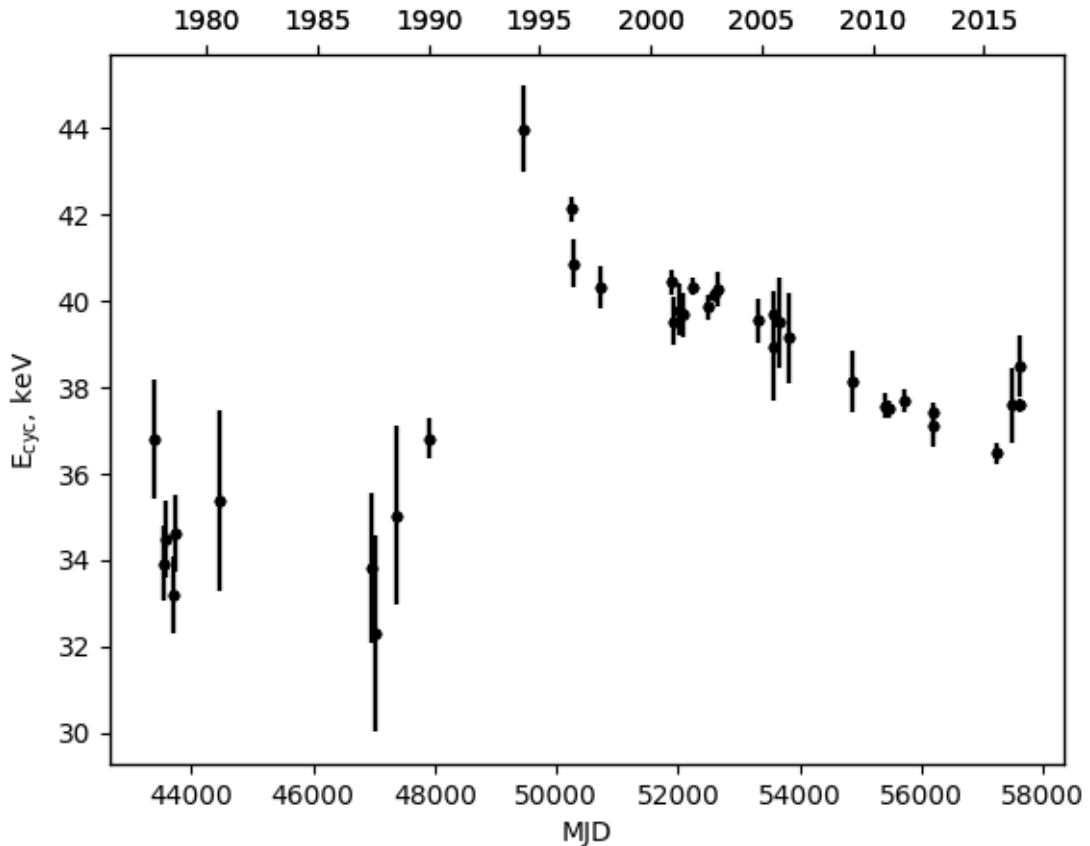
Figure 5.11: Long-term evolution of the cyclotron line energy in Her X-1. The data points were taken with a number of different X-ray missions, such as HEAO-1, Mir HEXE, Ginga, RXTE, BeppoSAX, Suzaku, NuSTAR, Integral and others. The figure is based on the data points taken from Staubert et al. (2014) with an addition of the recent NuSTAR and INTEGRAL observations reported in Staubert et al. (2016) and Staubert et al. (2017).

tens years.

In addition to the variations with time on different time scales, the energy of the cyclotron line in Her X-1 has been found to depend on X-ray luminosity. Staubert et al. (2007) reported a positive correlation between the line energy and X-ray flux based on RXTE and Integral observations carried out between 1996 and 2005. Her X-1 is thus the first object, in which a positive correlation has been discovered. The presence of a strong positive correlation between the line cyclotron line energy and X-ray luminosity in Her X-1 was subsequently confirmed by Klochkov et al. (2011), who also analyzed RXTE data, but using a more sophisticated pulse-amplitude-resolved, or just pulse-to-pulse, method, which was also applied in the previous two chapters, devoted to V 0332+53 and Cep X-4. Here, we try using the pulse-amplitude-resolved method to produce a correlation between the line cyclotron line energy and X-ray luminosity, but using NuSTAR data.
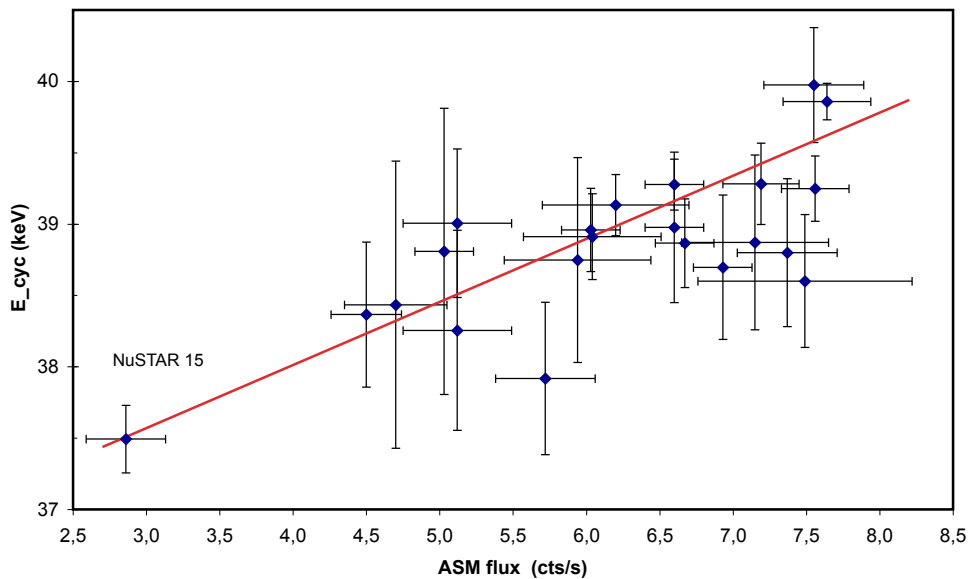
Figure 5.12: Positive correlation between the cyclotron line energy and X-ray flux in Her X-1, as a result of analysis of a decade-long monitoring with RXTE, Integral and NuSTAR. The correlation is corrected for the long-term time dependence of the line energy. The figure is taken from Staubert et al. (2016).

5.2 Analysis of a NuSTAR observation

Her X-1 has been being monitored. Here, I analyze the recent Her X-1 NuSTAR observation performed in August 2016 making use of the pulse-amplitude-resolved technique. Although Her!X-1 RXTE data have been analyzed by means of the this technique (Klochkov et al. 2011), it has never been applied to NuSTAR data. The NuSTAR observation with obsID 10202002002 seems to be suitable for this purpose because the source was in a main-on state and the exposure time of this observation is the largest (more than 36 ks), compared to other NuSTAR observations of the Her X-1. Also, as already mentioned above, Staubert et al. (2017) reported a change in the secular behaviour of the cyclotron line energy: in the recent NuSTAR observation the line energy begins increasing again after a 20-year gradual decay (Fig. 5.11).

First of all, the pulse-averaged spectrum has been extracted and briefly examined in terms of the best-fit function to find the position of the cyclotron line and other peculiarities, if any. The source and background spectra were extracted in a standard manner using circular regions with radii of 100″ and 80″, respectively. The region used for background extraction was selected as far as possible from the source. The data processing was performed using the standard `nupipeline` and `nuproducts` utilities and XSPEC[6] v12.9 as part of HEASOFT[7] 6.19 with CALDB version 20180312.

The resulted NuSTAR spectra are shown in Fig. 5.13. The blue and green colours correspond to distinct detectors, FMPA and FPMB, respectively. The continuum generally has not changed compared to previous NuSTAR observations and is described well with

---

[6]https://heasarc.gsfc.nasa.gov/xanadu/xspec/

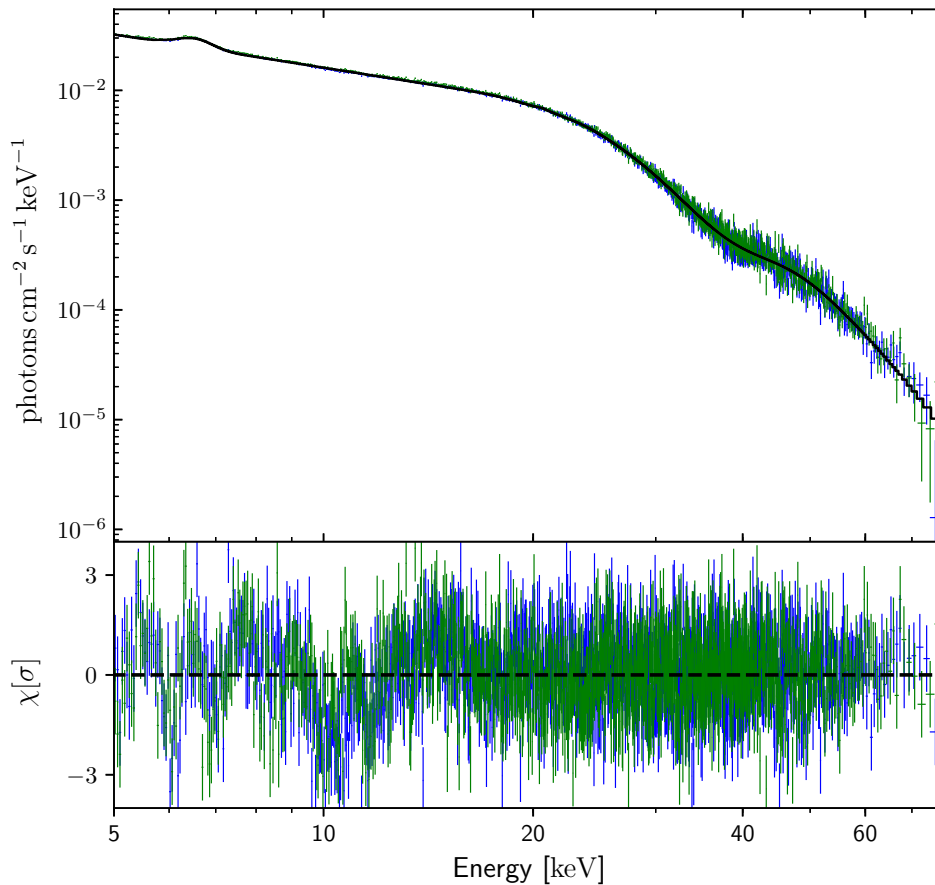[7]http://heasarc.nasa.gov/lheasoft/

Figure 5.13: 5-79 keV Her X-1 pulse-phase-averaged spectra of the NuSTAR observation performed in August 2016 (obsID 10202002002). The blue and green colours correspond to FMPA and FPMB detectors, respectively. The solid black line in the upper panel is the best-fit function.

a power law with a high energy exponential cutoff (the highecut function in XSPEC). As in the case of Cep X-4, to model the feature in the residuals around 20 keV caused by the derivative discontinuity between the power-law and highecut functions, an additional multiplicative component is needed. In the case of Her X-1 the gabs function with the centroid energy fixed to the cutoff energy is an appropriate selection. The iron line is fitted by an additive Gaussian emission line. The cyclotron line, like in previous NuSTAR observations, is described well with a gabs function. The main best fit parameters are presented in Table 5.1.

Note that the cyclotron line energy is indeed higher than in the previous 2015 NuSTAR observation (Staubert et al. 2016). The Her X-1 spectrum, however, is more complicated because several well-visible features remain in the residuals. One of them is the continuum feature around 10 keV, which has also been found in other X-ray pulsars observed by different missions. Two relatively sharp features in the iron line also are noticeable. The

Table 5.1: Parameters of the best-fit models of the pulse-averaged spectra, represented in Fig. 5.13, in the 5-79 keV energy range extracted from a circular region with a radius of 100″. The parameters of the additional wide Gaussian emission line are denoted by the "add" subscript. The line strength is expressed in terms of the optical depth with the equation $\tau = d/(\sigma\sqrt{2\pi})$. The indicated uncertainties are at 1σ (68%) confidence level.

Parameter	Value
Γ	$1.005^{+0.002}_{-0.002}$
E_{cut} [keV]	$20.6^{+0.2}_{-0.1}$
E_{fold} [keV]	$10.32^{+0.06}_{-0.07}$
E_{add} [keV]	$= E_{\text{cut}}$
σ_{add} [keV]	$1.60^{+0.07}_{-0.07}$
$E_{\text{Fe }K_\alpha}$ [keV]	$6.51^{+0.1}_{-0.1}$
$\sigma_{\text{Fe }K_\alpha}$ [keV]	$0.38^{+0.01}_{-0.01}$
E_{CRSF} [keV]	$37.45^{+0.14}_{-0.14}$
σ_{CRSF} [keV]	$5.9^{+0.2}_{-0.2}$
d_{CRSF}	$8.4^{+0.5}_{-0.3}$
$\chi^2_{\text{red}}/\text{d.o.f.}$	$1.25/2153$

iron line thus has a more complicated shape than a single line with a Gaussian optical-depth profile. But here we do not go into the investigation of these features.

To carry out the pulse-amplitude-resolved analysis, it is necessary to produce a distribution of the pulse heights, which is basically equivalent to a distribution of the number of counts in each pulse. The counts used for producing the distribution may be taken not only from the whole pulse, but also from a particular pulse phase range. To achieve a better signal-to-noise ratio, we chose the bright part of the pulse profile, i.e. the counts between phases of 0.1 and 0.9, (Fig. 5.14), to produce the distribution. Then this pulse phase interval is refereed to as pulse. Note that the 5-79 keV pulse profile has also not changed compared to that in other previous observations.

The resulted counts-in-pulse distribution is shown in Fig. 5.15. Both NuSTAR detectors were taken into account to build the distribution. The distribution turns out to have very similar shape compared to the Poisson distribution with the same average number of counts (Fig. 5.15). This implies that we see not intrinsic variability of the X-ray flux, but statistical fluctuations described by the Poisson distribution. The pulse-amplitude-resolved analysis is therefore not informative in the case of NuSTAR observations of Her X-1, which is explained with two reasons. The first is that Her X-1 is a persistent source showing no outburst or flaring activity. Second, the effective area of the NuSTAR detectors is not sufficient to collect an enough number of counts during the pulse cycle to reveal intrinsic X-ray flux fluctuations. Note that larger exposure time would apparently not affect this picture, it would only improve the distribution shape. Consequently, all NuSTAR observations of Her X-1 are not appropriate to be analyzed with the pulse-amplitude-
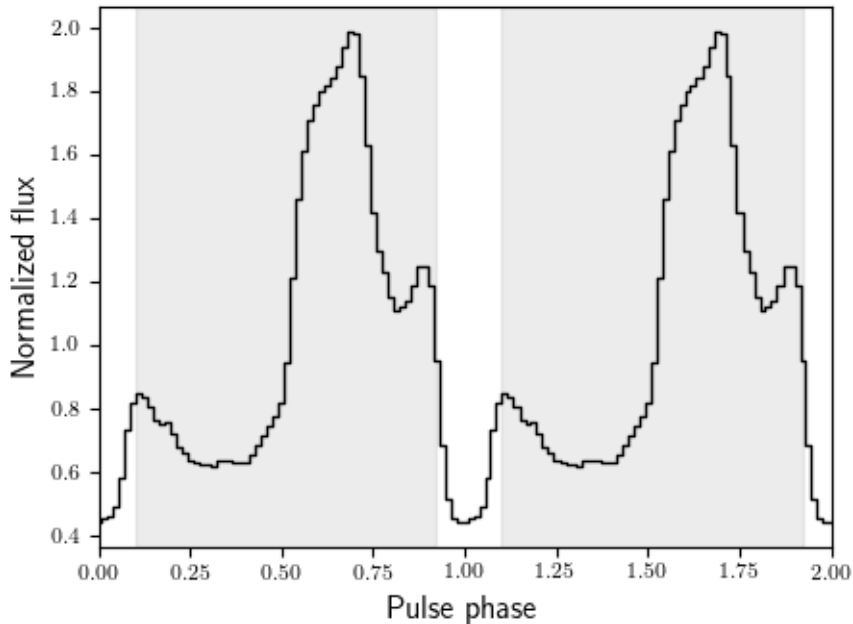
Figure 5.14: 3-79 keV NuSTAR pulse profile of the observation performed in August 2016 (obsID 10202002002). The shaded areas indicate the pulse phase interval used for producing of the distribution of counts presented in Fig. 5.15. The part of the pulse profile within this interval is refereed to as pulse.

resolved method.

5.3 Conclusions

Her X-1 is probably the best investigated accreting pulsar because it is sufficiently bright and predictable. Nevertheless, this is a relatively intricate X-ray binary system, which continues providing knowledge, improving the understanding of accretion processes in X-ray pulsars. Here we consider mainly the behaviour of the cyclotron line in the broad-band X-ray spectrum. One of the main features of this behaviour is the secular variability. Second feature is the positive correlation between the cyclotron line energy and X-ray luminosity. This result was obtained on long time scales (~10 years) as well as on short time scales (in the order of pulse cycle) by applying the phase-amplitude-resolved analysis to RXTE data.

The positive correlation in Her X-1 has been previously shown in RXTE data by using two different methods by Klochkov et al. (2011). According to a communication with Prof. Dr. Staubert, a correlation with the same slope is also shown in the last five NuSTAR observations with different maximum fluxes, but this result has not yet been published. The confirmation of this result in NuSTAR data using the phase-amplitude-resolved analysis would be valuable. The phase-amplitude-resolved analysis was successfully applied to the Cep X-4 and V0332+53 observations performed with NuSTAR as described in the previous two chapters. It was attempted to use this method for NuSTAR observations of
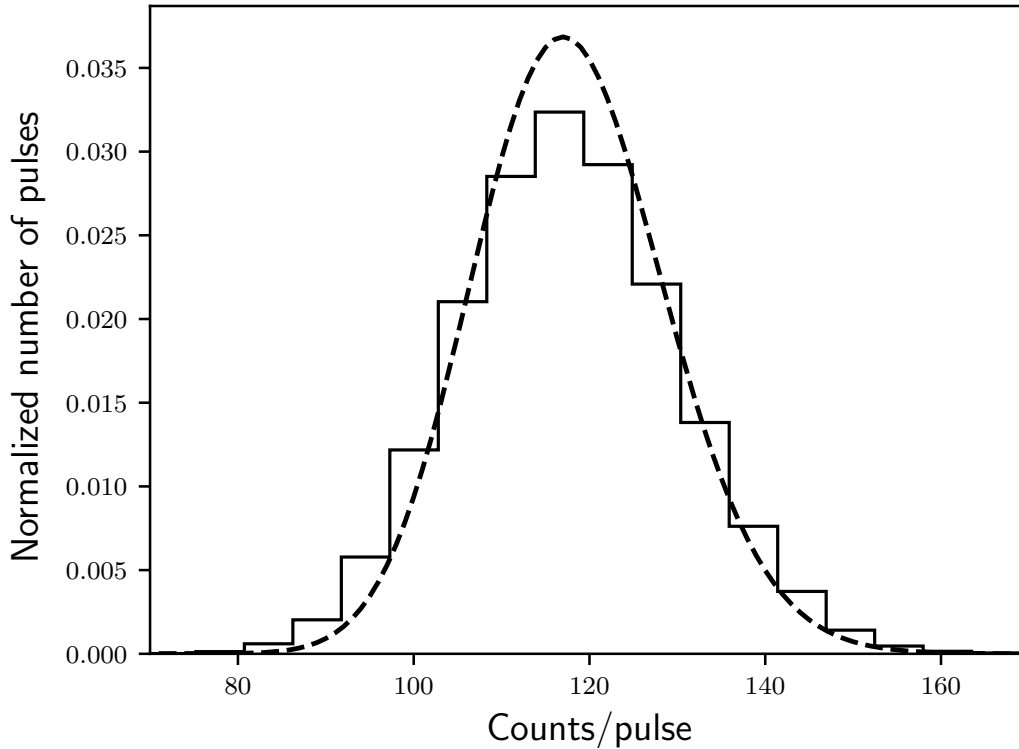
Figure 5.15: Normalized distribution of counts in individual pulses between 0.1 and 0.9 pulse phases (solid steps) and a Poisson distribution (dashed line), for comparison. The center of the Poisson (Gauss) distribution corresponds to the mean flux of the count distribution. The NuSTAR observation's obsID is 10202002002.

Her X-1.

The persistence of the central accreting machine that make Her X-1 convenient to study is a disadvantage to use the phase-amplitude-resolved analysis because this method demands a sufficiently large number of counts in a single pulse at the light curve, which is normally reached during the high flux states of transient sources in outburst. As shown above, a relatively short period and moderate brightness do not allow NuSTAR's detectors with their effective area to collect a sufficient number of counts to implement the analysis. In the case of Her X-1, the observed variability from pulse to pulse is caused by statistical fluctuations well described by a Poisson distribution.

Therefore, all NuSTAR observations of Her X-1 cannot be used for studying the cyclotron line energy dependence on X-ray luminosity with the phase-amplitude-resolved analysis.

6.   Summary and Outlook

The main topic of the present thesis is the study of the cyclotron line energy in the accreting pulsars Cepheus X-4, V 0332+53 and Hercules X-1. To perform our study, we used phase-averaged as well as flux-resolved spectra. To obtain spectra as a function of the X-ray flux, the pulse-amplitude-resolved technique was used. This technique allows us to investigate the variability of spectra of accreting pulsars on short time scales, i.e., time-scales of individual pulses. This opens the possibility to study the luminosity dependence of spectra in persistent sources, such as Her X-1 (Klochkov et al. 2011). In addition, since the method is insensitive to gradual time variations, it allowed us to decouple the luminosity dependence of the cyclotron line centroid energy from its long-term variability, as we have shown for V 0332+53. The pulse-amplitude-resolved technique requires, however, a sufficiently high number of photons within the single pulse cycle. This implies that the studied source shall be sufficiently bright and have not a too short spin period. This restriction clearly depends on the instrument used for the observations. For example, it was not possible to study the correlation between the cyclotron line energy and luminosity in Her X-1 using NuSTAR data since the neutron star spin period is too short to allow us to collect sufficient photon statistics. Unlike NuSTAR, the larger effective area of RXTE/PCA allowed Klochkov et al. (2011) to reveal a positive correlation between the cyclotron line energy and luminosity in Her X-1.

The key results of the thesis are summarized as it follows:

- *Cepheus X-4.* It was shown that the cyclotron line energy is positively correlated with the X-ray luminosity within each observation during the 2014 outburst and for the different observations. The slope of the correlations obtained with the pulse-amplitude-resolved technique is consistent with the slope measured between the observations, implying that the same physical mechanism generates the spectrum-luminosity variability on short time scales as well as on long time scales. This also indicates the absence of any long-term variability of the cyclotron line centroid energy in the considered data.

  In addition to the detection the positive correlation between the cyclotron line energy and X-ray luminosity, we found that the continuum changes with luminosity as well, namely the spectral hardness ratio ($F_{8-12\,\mathrm{keV}}/F_{4-6\,\mathrm{keV}}$) increases with the X-ray flux, i.e., the continuum becomes harder with flux. The pulse-amplitude-resolved technique allowed us to determine that the shape of the hardness – luminosity dependence is not linear and could be described by a model implying a collisionless shock above the neutron star surface in the case of sub-critical accretion regime. However, the model is hardly applicable to describe the $E_{\mathrm{CRSF}} - L_{\mathrm{x}}$ dependence, though this could be a result of insufficient data quality.

We have also detected the harmonic of the cyclotron line based on NuSTAR data as a result of an in-depth analysis of the phase-averaged spectra. We thus confirm the finding of Jaisawal & Naik (2015), who used Suzaku data.

The results of this study have been published in Vybornov et al. (2017).

- *V 0332+53.* Using the pulse-amplitude-resolved technique, we were able to decouple the luminosity dependence of the cyclotron line energy from its long-term time dependence. We also confirmed with high significance the transition from an anti-correlation to a correlation between the cyclotron line energy and X-ray luminosity. We observed the transition luminosity at $L_{cr} = (2.1 \pm 0.4) \times 10^{37}$ erg/s, which likely reflects the transition between the super- and sub-critical accretion regimes.

  We also found that the aforementioned time dependence of the cyclotron line energy breaks up when the source changes its accretion regime. After the break-up, e.g., by the minor 2015 outbursts, the line energy returned to the value observed at the beginning of the giant 2014 outburst. Based on the analysis of the power density spectra we concluded that the temporal changes in the cyclotron line energy are related to changes in the geometrical configuration of the emission region rather than to intrinsic changes of the global dipole magnetic field as suggested in literature.

  The results of this study have been published in Vybornov et al. (2018).

- *Hercules X-1.* We attempted to apply the pulse-amplitude-resolved technique to NuSTAR Her X-1 data to investigate the behaviour of the cyclotron line. This could also have confirmed the presence of the positive correlation previously found with RXTE/PCA by Klochkov et al. (2011). Unfortunately, the capabilities of the NuSTAR telescopes turned out to be insufficient to identify the intrinsic pulse-to-pulse variability in Her X-1, and the observed variability was compatible with statistical noise. Therefore, we showed the limits of the applicability of the pulse-amplitude-resolved method for real data.

  Nevertheless, Her X-1 exhibits a positive correlation between the cyclotron line energy and X-ray luminosity on long time scales. In addition to the correlation with luminosity, the cyclotron line energy also shows a long-term gradual decay, i.e. it depends both on luminosity and on time. The NuSTAR observations confirmed that the decay was still ongoing in 2015.

  The results of the monitoring of the cyclotron line energy behaviour based on the NuSTAR observations performed in 2015 have been published in Staubert et al. (2016).

Although accreting pulsars were discovered about fifty years ago, many issues concerning the accretion physics and the evolution of such objects are still open. Many models to explain the formation of the emission and its variability, have been proposed by different authors. However, these models are still being developed and discussed, and there is not a general agreement on the main aspects of the accretion physics in X-ray pulsars. For example, it is poorly understood what geometry the accretion mound has, where and how the cyclotron feature forms, what is responsible for long-term variability of the cyclotron line energy. Moreover, in recent years, new classes of accreting neutron stars, such as ultra-luminous X-ray pulsars, millisecond and transitional pulsars were

discovered. This shows that the study of accreting pulsars still remains a hot topic in astrophysics. A new generation of X-ray observatories is most likely needed to progress on this topic, since these new observatories will provide statistically robust observational results, which are the base of new theoretical models and our understanding of these fascinating objects.

A. On collisionless shocks in space

Here I would like to give a general introduction into the understanding of what collisionless shocks in space are. I do not discuss the particular physics of collisionless shocks in the case of accretion onto a neutron star. It was already considered in Bisnovatyi-Kogan & Fridman (1969); Shapiro & Salpeter (1975); Langer & Rappaport (1982) and other works. Nevertheless, since the therm might be confusing, it needs to be clarified.

The collisionless shock can be defined as a dramatic rise in density, temperature, magnetic and electric field strengths (and other parameters of plasma) caused by the traveling of supersonic plasma flows. "Collisionless" means that the width of the shock front is much narrower compared to the electron mean free path in the plasma. This situation is realized in low density plasma with high temperature, i.e. in interplanetary and interstellar environments. Indeed, collisionless shocks are present in a variety of astrophysical sources, such as coronal mass ejects, supernova remnants, active galactic nuclei, galaxy clusters, gamma-ray binaries and more. But if there are no collisions, how does the shock form and how does the energy dissipate?

To answer these questions, we should go back to the concept of the speed of sound in plasma. This is the speed of ion acoustic waves, which are one of the longitudinal oscillations in the plasma. While they propagate, these waves interact with the plasma electromagnetic field. This is different than the propagation of acoustic waves in a neutral gas. While the collisions of particles in a neutral gas are responsible for the propagation of the longitudinal oscillations, the ion acoustic waves have a collective nature. The existence of ion acoustic waves is defined by the condition

$$v_i \ll \frac{\omega}{k} \ll v_e \tag{A.1}$$

where v_i, v_e are the thermal velocities of the ions and electrons, respectively; ω, k are the frequency and wavenumber of a wave. The phase velocity of an ion acoustic wave $v_{ph} = \omega/k$ should therefore be much large than the thermal velocities of the ions and much smaller than the thermal velocities of the electrons.

The dispersion relation for this kind of waves is

$$\omega(k) = \frac{k v_s}{\sqrt{1 + (k r_D)^2}}, \tag{A.2}$$

where

$$v_s = \sqrt{\frac{T_e}{m_i}} \tag{A.3}$$

is the speed of sound (T_e is the electrons temperature and m_i is the ion mass) and
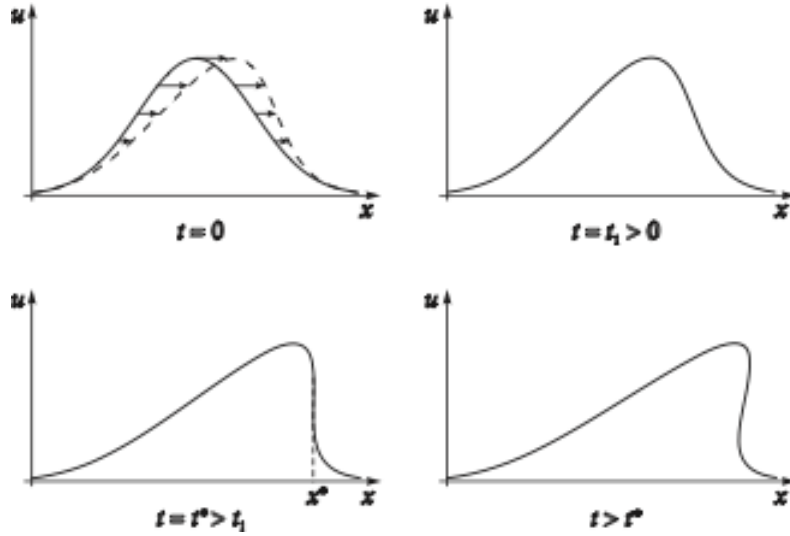
$$r_D = \sqrt{\frac{T_e}{4\pi e^2 N_e}} \tag{A.4}$$

Figure A.1: Formation of the steeping-speed profile of a non-linear wave.

is the Debye radius (e is the electron charge and N_e is the electron density). As can be seen, in the case of long wavelengths, $kr_D \ll 1$, the dispersion relation is linear, i.e. $\omega(k) = kv_s$, which is the same as for the speed of sound in a neutral gas.

Since magnetic fields are always present in the cosmic space, cosmic plasma is normally imbued with them, which substantially changes and complicates the character of waves propagation in plasma. Magnetosonic waves, which are low-frequency (compared to the ion cyclotron frequency) oscillations of the ions and the magnetic field, have to be considered in real cosmic conditions. In the cold plasma with the pressure p, lower than the magnetic pressure p_M ($p \ll H^2/8\pi$), these waves propagate with Alfvén velocity

$$v_A = \frac{H}{\sqrt{4\pi\rho}} \tag{A.5}$$

where ρ is the plasma density and H is the magnetic field strength. In magnetized plasma, the Alfvén velocity plays the role of the speed of sound.

If some part of plasma begins to move with a speed that exceeds the Alfvén velocity, arising disturbances can not keep escaping as magnetosonic waves, which results in plasma compressing and increasing of the frozen magnetic field in the shock vicinity. This process is similar to a moving piston that has supersonic speed. Planetary or neutron star magnetospheres could play the role of such a piston as well as the surface of the neutron star. As the magnetic field strength increases, the local Alfvén velocity rises, which enables disturbances to tear away from the "piston" forming the front of the collisionless shock.

In a neutral gas, the width of the shock front is comparable to the particle mean free path because it is confined by particle collisions in the shock, whereas, in the cosmic plasma, the mean free path far exceeds the width of the shock front. But the questions are, what the collisionless shock front is, how far away from the "piston" the front can be and why it does not smear ad infinitum?

In general terms, owing to the presence of some velocity distribution, particles at the shock front with velocities higher than the average velocity always exist. These particles

penetrate into the undisturbed plasma where they either move following a circular line by the Lorentz force (if the shock propagates transversely to the magnetic field lines, i.e. a perpendicular shock) or decelerate due to plasma instabilities (for example, the beam instability in a parallel shock), inducing the excitation of high-amplitude oscillations before the shock front and preventing the front smearing.
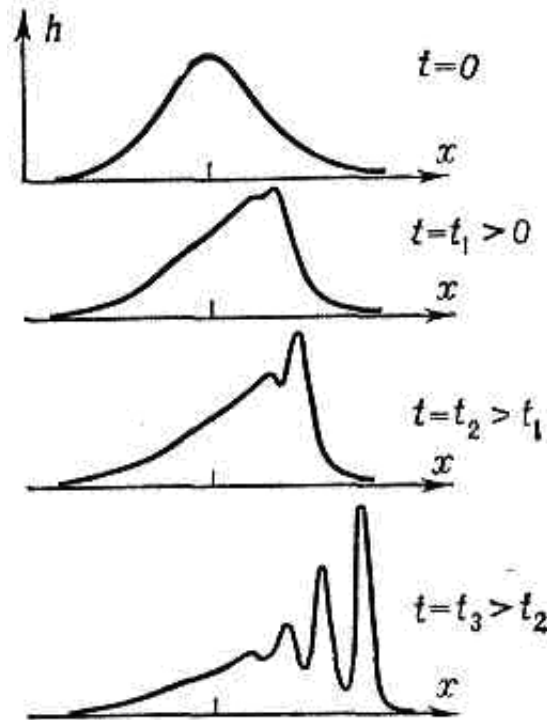

Figure A.2: Formation of a soliton structure due to non-linear and dispersion properties of plasma medium.

The shock is always associated with energy dissipation and the transformation of the stationary motion of particles before the shock to chaotic motion after the shock. Intense oscillations of density, magnetic field and other parameters turn out to be present after the collisionless shock. These oscillations are caused by not only plasma instabilities, but they can also be solitons, which are formed due to specific dispersion peculiarities of plasma. These features, mainly dispersion packet spreading, are able to prevent the wave steeping (Fig. A.1), associated with non-linearity of plasma. In other words, wave steeping is the formation of the harmonics with a higher value of the wavenumber. In the medium that posses the wave dispersion, these higher harmonics lose contact with the main wave packet. Depending on medium properties, these harmonics either leave the main wave packet behind or are left behind by it. As a result, separate magnetosonic solitons are created (Fig. A.2), and their superposition forms the front of the collisionless shock. However, the solitons are not the agents where the energy dissipates, since a soliton is formed due to only two factors, namely, the non-linearity of plasma and the waves dispersion. The energy dissipation of the magnetosonic waves after the front is ensured either through the Landau damping (in the laminar flow) or through plasma instabilities developing at the shock front (in the turbulent case). Solitons thus could only contribute to generating various kind of plasma instabilities.

B.   On the `compTT` model

Comptomozation is a problem of the radiative transfer of photons scattering on free electrons in a plasma cloud. The average energy exchange per scattering is determined by the energy relation between the photon and electron. If the electrons have a thermal energy distribution with the temperature T_e, the change in the photon energy is

$$\frac{\Delta \nu}{\nu} = \frac{4kT_e - h\nu}{m_e c^2},$$ (B.1)

where ν is the photon frequency, m_e is the electron mass, c is the speed of light and k and h are the Boltzmann and Plank constants, respectively. When the photon energy is larger than the mean electron energy, the photon loses its energy due to the recoil effect, i.e. the ordinary Compton effect is observed. In the opposite case, when $h\nu \ll kT_e$, the photon gains energy due to the Doppler effect, which is called the inverse Compton effect. These two processes compete with each other and result in distortion of the initial spectrum. The shape of the observed spectrum is determined by the Comptonization parameter

$$y \approx \frac{4kT_e}{m_e c^2}\bar{u},$$ (B.2)

where $\bar{u}$ is the average number of scattering, which photons undergo in the plasma cloud, assuming the Thomson cross-section. In the diffusion approximation, i.e. for a plasma cloud with the optical depth $\tau \gg 1$, the average number of scatterings $\bar{u} \sim \tau^2$, and the Comptonization parameter

$$y \approx \frac{4kT_e}{m_e c^2}\tau^2.$$ (B.3)

For the moderate values of the Comptonization parameter, $y \sim 1$, some of the soft seed photons scatter less frequently than $\bar{u}$, so that they penetrate deeper in the plasma cloud retaining the information about the initial spectral distribution, and thus contribute this information to the observed spectrum. The spectral distribution of the photons that have a number of scatterings much greater than $\bar{u}$ is mainly characterized by the optical depth τ and the temperature T_e, and the outgoing spectrum distribution is so distorted that is is almost independent of the initial distribution of the soft seed photons. This results in a power-law spectrum with the spectral index

$$\alpha = \left(\frac{9}{4} + \frac{1}{y}\right)^{\frac{1}{2}} - \frac{3}{2}.$$ (B.4)

The observed spectrum thus includes the soft part retaining the information about the seed photons and the hard part with the shape depending on τ and T_e. A harder spectrum

corresponds to a higher τ, while T_e determines the high energy cut-off. Note that for $y \gg 1$ the entire spectrum has a Wien shape since, in this case, the equilibrium between photons and electrons is reached. The model is valid for plasma temperatures of 2-500 keV and is not applicable when the temperature and optical depth are simultaneously low or high.

Bibliography

Alexander, S. G., Meszaros, P., & Bussard, R. W. 1989, ApJ, 342, 928

Alpar, M. A., Cheng, A. F., Ruderman, M. A., & Shaham, J. 1982, Nature, 300, 728

Archibald, A. M., Stairs, I. H., Ransom, S. M., et al. 2009, Science, 324, 1411

Bachetti, M., Harrison, F. A., Cook, R., et al. 2015, ApJ, 800, 109

Bachetti, M., Harrison, F. A., Walton, D. J., et al. 2014, Nature, 514, 202

Basko, M. M. & Sunyaev, R. A. 1975, A&A, 42, 311

Basko, M. M. & Sunyaev, R. A. 1976, MNRAS, 175, 395

Bassa, C. G., Patruno, A., Hessels, J. W. T., et al. 2014, MNRAS, 441, 1825

Becker, P. A., Klochkov, D., Schönherr, G., et al. 2012, A&A, 544, A123

Becker, P. A. & Wolff, M. T. 2007, ApJ, 654, 435

Bisnovatyi-Kogan, G. S. & Fridman, A. M. 1969, AZh, 46, 721

Bogdanov, S., Deller, A. T., Miller-Jones, J. C. A., et al. 2018, ApJ, 856, 54

Boldin, P. A., Tsygankov, S. S., & Lutovinov, A. A. 2013, Astronomy Letters, 39, 375

Bond, H. E., White, R. L., Becker, R. H., & O'Brien, M. S. 2002, PASP, 114, 1359

Bonnet-Bidaud, J. M. & Mouchet, M. 1998, A&A, 332, L9

Boynton, P. E., Canterna, R., Crosa, L., Deeter, J., & Gerend, D. 1973, ApJ, 186, 617

Brandt, N. & Podsiadlowski, P. 1995, MNRAS, 274, 461

Brightman, M., Harrison, F. A., Fürst, F., et al. 2018, Nature Astronomy, 2, 312

Burnard, D. J., Arons, J., & Klein, R. I. 1991, ApJ, 367, 575

Bussard, R. W., Alexander, S. B., & Meszaros, P. 1986, Phys. Rev. D, 34, 440

Bykov, A. M. & Krasilshchikov, A. M. 2004, Astronomy Letters, 30, 309

Caballero, I., Santangelo, A., Kretschmar, P., et al. 2008, A&A, 480, L17

Cannon, C. J. 1970, ApJ, 161, 255

Ceccobello, C., Farinelli, R., & Titarchuk, L. 2014, A&A, 562, A99

Christensen, F. E., Jakobsen, A. C., Brejnholt, N. F., et al. 2011, in Proc. SPIE, Vol. 8147, Society of Photo-Optical Instrumentation Engineers (SPIE) Conference Series, 81470U

Coburn, W., Heindl, W. A., Rothschild, R. E., et al. 2002, ApJ, 580, 394

Coburn, W., Kretschmar, P., Kreykenbohm, I., et al. 2005, The Astronomer's Telegram, 381

Corbet, R. H. D. 1986, MNRAS, 220, 1047

Crampton, D. & Hutchings, J. B. 1974, ApJ, 191, 483

Cusumano, G., La Parola, V., D'Aì, A., et al. 2016, MNRAS, 460, L99

dal Fiume, D., Orlandini, M., Cusumano, G., et al. 1998, A&A, 329, L41

Davidson, K. 1973, Nature Physical Science, 246, 1

Davidson, K. & Ostriker, J. P. 1973, ApJ, 179, 585

Deeter, J., Crosa, L., Gerend, D., & Boynton, P. E. 1976, ApJ, 206, 861

Deeter, J. E., Scott, D. M., Boynton, P. E., et al. 1998, ApJ, 502, 802

Delgado, A. & Thomas, H. 1981, A&A, 96, 142

Doroshenko, V., Santangelo, A., Doroshenko, R., et al. 2014, A&A, 561, A96

Doroshenko, V., Santangelo, A., Nakahira, S., et al. 2013, A&A, 554, A37

Doroshenko, V., Tsygankov, S., & Santangelo, A. 2016, A&A, 589, A72

Doroshenko, V., Tsygankov, S. S., Mushtukov, A. A., et al. 2017, MNRAS, 466, 2143

Ebisuzaki, T. & Nakamura, N. 1988, ApJ, 328, 251

Elsner, R. F. & Lamb, F. K. 1977, ApJ, 215, 897

Fabian, A. C. 1973, Nature, 244, 212

Farinelli, R., Ceccobello, C., Romano, P., & Titarchuk, L. 2012, A&A, 538, A67

Farinelli, R., Ferrigno, C., Bozzo, E., & Becker, P. A. 2016, A&A, 591, A29

Ferrigno, C., Becker, P. A., Segreto, A., Mineo, T., & Santangelo, A. 2009, A&A, 498, 825

Frontera, F., dal Fiume, D., Morelli, E., & Spada, G. 1985, ApJ, 298, 585

Fujimoto, M. Y., Hanawa, T., & Miyaji, S. 1981, ApJ, 247, 267

Fürst, F., Grefenstette, B. W., Staubert, R., et al. 2013, ApJ, 779, 69

Fürst, F., Pottschmidt, K., Miyasaka, H., et al. 2015, ApJ, 806, L24

Fürst, F., Pottschmidt, K., Wilms, J., et al. 2014, ApJ, 780, 133

Fürst, F., Walton, D. J., Harrison, F. A., et al. 2016, ApJ, 831, L14

Fushiki, I. & Lamb, D. Q. 1987a, ApJ, 323, L55

Fushiki, I. & Lamb, D. Q. 1987b, ApJ, 317, 368

Gerend, D. & Boynton, P. E. 1976, ApJ, 209, 562

Ghosh, P. & Lamb, F. K. 1978, ApJ, 223, L83

Ghosh, P. & Lamb, F. K. 1979, ApJ, 234, 296

Giacconi, R., Gursky, H., Kellogg, E., et al. 1973, ApJ, 184, 227

Giacconi, R., Gursky, H., Kellogg, E., Schreier, E., & Tananbaum, H. 1971, ApJ, 167, L67

Gnedin, Y. N. & Sunyaev, R. A. 1973, MNRAS, 162, 53

Gonthier, P. L., Baring, M. G., Eiles, M. T., et al. 2014, Phys. Rev. D, 90, 043014

Goranskij, V. & Barsukova, E. 2004, The Astronomer's Telegram, 245

Grimm, H.-J., Gilfanov, M., & Sunyaev, R. 2002, A&A, 391, 923

Gruber, D. E., Heindl, W. A., Rothschild, R. E., et al. 2001, ApJ, 562, 499

Hailey, C. J., An, H., Blaedel, K. L., et al. 2010, in Proc. SPIE, Vol. 7732, Space Telescopes and Instrumentation 2010: Ultraviolet to Gamma Ray, 77320T

Harrison, F. A., Craig, W. W., Christensen, F. E., et al. 2013, ApJ, 770, 103

Hemphill, P. B., Rothschild, R. E., Markowitz, A., et al. 2014, ApJ, 792, 14

Hoffman, J. A., Lewin, W. H. G., & Doty, J. 1977, ApJ, 217, L23

Hu, C.-P., Li, K. L., Kong, A. K. H., Ng, C.-Y., & Lin, L. C.-C. 2017, ApJ, 835, L9

Hua, X.-M. & Titarchuk, L. 1995, ApJ, 449, 188

Illarionov, A. F. & Sunyaev, R. A. 1975, A&A, 39, 185

Israel, G. L., Papitto, A., Esposito, P., et al. 2017, MNRAS, 466, L48

Ivanova, N., Justham, S., Avendano Nandez, J. L., & Lombardi, J. C. 2013, Science, 339, 433

Iyer, N., Mukherjee, D., Dewangan, G. C., Bhattacharya, D., & Seetha, S. 2015, MNRAS, 454, 741

Jaisawal, G. K. & Naik, S. 2015, MNRAS, 453, L21

Katz, J. I. 1973, Nature Physical Science, 246, 87

Kendziorra, E., Kretschmar, P., Pan, H. C., et al. 1994, A&A, 291, L31

Kitaguchi, T., Grefenstette, B. W., Harrison, F. A., et al. 2011, in Proc. SPIE, Vol. 8145, Society of Photo-Optical Instrumentation Engineers (SPIE) Conference Series, 814507

Klochkov, D., Doroshenko, V., Santangelo, A., et al. 2012, A&A, 542, L28

Klochkov, D., Staubert, R., Postnov, K., et al. 2008, A&A, 482, 907

Klochkov, D., Staubert, R., Santangelo, A., Rothschild, R. E., & Ferrigno, C. 2011, A&A, 532, A126

Kluźniak, W. & Lasota, J.-P. 2015, MNRAS, 448, L43

Kompaneets, A. 1956, ZhETF, 31, 876

Kong, A. K. H., Homer, L., Kuulkers, E., Charles, P. A., & Smale, A. P. 2000, MNRAS, 311, 405

Kong, A. K. H., Hu, C.-P., Lin, L. C.-C., et al. 2016, MNRAS, 461, 4395

Koyama, K., Kawada, M., Tawara, Y., et al. 1991, ApJ, 366, L19

Kraus, U. 2001, ApJ, 563, 289

Kraus, U., Zahn, C., Weth, C., & Ruder, H. 2003, ApJ, 590, 424

Kretschmar, P., Kreykenbohm, I., Wilms, J., et al. 1997, in ESA Special Publication, Vol. 382, The Transparent Universe, ed. C. Winkler, T. J.-L. Courvoisier, & P. Durouchoux, 141

Kreykenbohm, I., Kretschmar, P., Wilms, J., et al. 1999, A&A, 341, 141

Kreykenbohm, I., Mowlavi, N., Produit, N., et al. 2005, A&A, 433, L45

Kunz, M., Kendziorra, E., Kretschmar, P., et al. 1996, A&AS, 120, 233

Kurochkin, N. E. 1972, Peremennye Zvezdy, 18, 425

Kuster, M., Wilms, J., Staubert, R., et al. 2005, A&A, 443, 753

La Parola, V., Cusumano, G., Segreto, A., & D'Aì, A. 2016, MNRAS, 463, 185

Lamb, F. K., Pethick, C. J., & Pines, D. 1973, ApJ, 184, 271

Langer, S. H. & Rappaport, S. 1982, ApJ, 257, 733

Leahy, D. A. 2002, MNRAS, 334, 847

Leahy, D. A., Darbro, W., Elsner, R. F., et al. 1983, ApJ, 266, 160

Leahy, D. A. & Kostka, M. 2008, MNRAS, 384, 747

Liller, W. 1972, IAU Circ., 2415

Lipunov, V. M. 1987, Soviet Ast., 31, 167

Lipunov, V. M. & Shakura, N. I. 1976, Soviet Astronomy Letters, 2, 133

Liu, Q. Z., van Paradijs, J., & van den Heuvel, E. P. J. 2007, A&A, 469, 807

London, R. A., Howard, W. M., & Taam, R. E. 1984, ApJ, 287, L27

London, R. A., Taam, R. E., & Howard, W. M. 1986, ApJ, 306, 170

Lyubarskii, Y. É. 1986, Astrophysics, 25, 577

Lyubarskii, Y. E. 1997, MNRAS, 292, 679

Makino, F. & GINGA Team. 1988, IAU Circ., 4575

Makishima, K., Mihara, T., Ishida, M., et al. 1990, ApJ, 365, L59

Makishima, K., Mihara, T., Nagase, F., & Tanaka, Y. 1999, ApJ, 525, 978

Malacaria, C., Klochkov, D., Santangelo, A., & Staubert, R. 2015, A&A, 581, A121

Malacaria, C., Mihara, T., Santangelo, A., et al. 2016, A&A, 588, A100

McBride, V. A., Wilms, J., Kreykenbohm, I., et al. 2007, A&A, 470, 1065

McGowan, K. E. & Charles, P. A. 2003, MNRAS, 339, 748

Middleditch, J. 1983, ApJ, 275, 278

Mihara, T., Makishima, K., Kamijo, S., et al. 1991, ApJ, 379, L61

Mowlavi, N., Kreykenbohm, I., Shaw, S. E., et al. 2006, A&A, 451, 187

Müller, D., Klochkov, D., Caballero, I., & Santangelo, A. 2013a, A&A, 552, A81

Müller, S., Ferrigno, C., Kühnel, M., et al. 2013b, A&A, 551, A6

Mushtukov, A. A., Suleimanov, V. F., Tsygankov, S. S., & Poutanen, J. 2015a, MNRAS, 454, 2539

Mushtukov, A. A., Suleimanov, V. F., Tsygankov, S. S., & Poutanen, J. 2015b, MNRAS, 447, 1847

Mushtukov, A. A., Tsygankov, S. S., Serber, A. V., Suleimanov, V. F., & Poutanen, J. 2015c, MNRAS, 454, 2714

Nagel, W. 1980, ApJ, 236, 904

Nagel, W. 1981a, ApJ, 251, 288

Nagel, W. 1981b, ApJ, 251, 278

Nagel, W. & Meszaros, P. 1985, ApJ, 298, 147

Negueruela, I., Roche, P., Fabregat, J., & Coe, M. J. 1999, MNRAS, 307, 695

Okazaki, A. T. & Negueruela, I. 2001a, A&A, 377, 161

Okazaki, A. T. & Negueruela, I. 2001b, X-ray Astronomy: Stellar Endpoints, AGN, and the Diffuse X-ray Background, 599, 810

Oosterbroek, T., Parmar, A. N., Orlandini, M., et al. 2001, A&A, 375, 922

Paczynski, B. 1976, Comments on Astrophysics, 6, 95

Paczynski, B. 1983, ApJ, 267, 315

Parmar, A. N., Oosterbroek, T., dal Fiume, D., et al. 1999, A&A, 350, L5

Patruno, A., Archibald, A. M., Hessels, J. W. T., et al. 2014, ApJ, 781, L3

Petterson, J. A. 1975, ApJ, 201, L61

Petterson, J. A. 1977, ApJ, 218, 783

Petterson, J. A., Rothschild, R. E., & Gruber, D. E. 1991, ApJ, 378, 696

Pfahl, E., Rappaport, S., & Podsiadlowski, P. 2003, ApJ, 597, 1036

Podsiadlowski, P., Rappaport, S., & Pfahl, E. D. 2002, ApJ, 565, 1107

Postnov, K., Shakura, N., Staubert, R., et al. 2013, MNRAS, 435, 1147

Postnov, K. A., Gornostaev, M. I., Klochkov, D., et al. 2015, MNRAS, 452, 1601

Pottschmidt, K., Kreykenbohm, I., Wilms, J., et al. 2005, ApJ, 634, L97

Poutanen, J., Mushtukov, A. A., Suleimanov, V. F., et al. 2013, ApJ, 777, 115

Pozdnyakov, L. A., Sobol, I. M., & Syunyaev, R. A. 1983, Astrophysics and Space Physics Reviews, 2, 189

Pringle, J. E. & Rees, M. J. 1972, A&A, 21, 1

Protassov, R., van Dyk, D. A., Connors, A., Kashyap, V. L., & Siemiginowska, A. 2002, ApJ, 571, 545

Radhakrishnan, V. 1982, Contemporary Physics, 23, 207

Rana, V. R., Cook, III, W. R., Harrison, F. A., Mao, P. H., & Miyasaka, H. 2009, in Proc. SPIE, Vol. 7435, UV, X-Ray, and Gamma-Ray Space Instrumentation for Astronomy XVI, 743503

Reig, P. 2007, MNRAS, 377, 867

Revnivtsev, M., Churazov, E., Postnov, K., & Tsygankov, S. 2009, A&A, 507, 1211

Revnivtsev, M., Postnov, K., Kuranov, A., & Ritter, H. 2011, A&A, 526, A94

Reynolds, A. P., Quaintrell, H., Still, M. D., et al. 1997, MNRAS, 288, 43

Roche, P., Green, L., & Hoenig, M. 1997, IAU Circ., 6698

Rothschild, R. E., Kühnel, M., Pottschmidt, K., et al. 2017, MNRAS, 466, 2752

Roy, J., Ray, P. S., Bhattacharyya, B., et al. 2015, ApJ, 800, L12

Runacres, M. C. & Owocki, S. P. 2005, A&A, 429, 323

Sartore, N., Jourdain, E., & Roques, J. P. 2015, ApJ, 806, 193

Schwarm, F.-W., Schönherr, G., Falkner, S., et al. 2017, A&A, 597, A3

Scott, D. M. & Leahy, D. A. 1999, ApJ, 510, 974

Scott, D. M., Leahy, D. A., & Wilson, R. B. 2000, ApJ, 539, 392

Shakura, N., Postnov, K., Kochetkova, A., & Hjalmarsdotter, L. 2012, MNRAS, 420, 216

Shakura, N. I., Prokhorov, M. E., Postnov, K. A., & Ketsaris, N. A. 1999, A&A, 348, 917

Shapiro, S. L. & Salpeter, E. E. 1975, ApJ, 198, 671

Stappers, B. W., Archibald, A. M., Hessels, J. W. T., et al. 2014, ApJ, 790, 39

Staubert, R., Bezler, M., & Kendziorra, E. 1983, A&A, 117, 215

Staubert, R., Kendziorra, E., Pietsch, W., et al. 1980, ApJ, 239, 1010

Staubert, R., Klochkov, D., Fürst, F., et al. 2017, A&A, 606, L13

Staubert, R., Klochkov, D., Vasco, D., et al. 2013, A&A, 550, A110

Staubert, R., Klochkov, D., Vybornov, V., Wilms, J., & Harrison, F. A. 2016, A&A, 590, A91

Staubert, R., Klochkov, D., & Wilms, J. 2009, A&A, 500, 883

Staubert, R., Klochkov, D., Wilms, J., et al. 2014, A&A, 572, A119

Staubert, R., Schandl, S., Klochkov, D., et al. 2006, in American Institute of Physics Conference Series, Vol. 840, The Transient Milky Way: A Perspective for MIRAX, ed. F. D'Amico, J. Braga, & R. E. Rothschild, 65–70

Staubert, R., Schandl, S., & Wilms, J. 2000, in American Institute of Physics Conference Series, Vol. 510, American Institute of Physics Conference Series, ed. M. L. McConnell & J. M. Ryan, 153–157

Staubert, R., Shakura, N. I., Postnov, K., et al. 2007, A&A, 465, L25

Stella, L. & White, N. E. 1983, IAU Circ., 3902

Stella, L., White, N. E., Davelaar, J., et al. 1985, ApJ, 288, L45

Strohmayer, T. & Bildsten, L. 2003, ArXiv Astrophysics e-prints

Sunyaev, R. A. & Titarchuk, L. G. 1980, A&A, 86, 121

Sunyaev, R. A. & Titarchuk, L. G. 1985, A&A, 143, 374

Swank, J. H., Becker, R. H., Boldt, E. A., et al. 1977, ApJ, 212, L73

Taam, R. E., Woosley, S. E., & Lamb, D. Q. 1996, ApJ, 459, 271

Tanaka, Y. 1986, in Lecture Notes in Physics, Berlin Springer Verlag, Vol. 255, IAU Colloq. 89: Radiation Hydrodynamics in Stars and Compact Objects, ed. D. Mihalas & K.-H. A. Winkler, 198

Tananbaum, H., Gursky, H., Kellogg, E. M., et al. 1972, ApJ, 174, L143

Terrell, J. & Priedhorsky, W. C. 1984, ApJ, 285, L15

Thorstensen, J. R. & Armstrong, E. 2005, AJ, 130, 759

Titarchuk, L. 1994a, ApJ, 434, 570

Titarchuk, L. 1994b, ApJ, 429, 340

Treuz, S., Doroshenko, V., Santangelo, A., & Staubert, R. 2018, ArXiv, 1806.11397

Trümper, J., Pietsch, W., Reppin, C., et al. 1978, ApJ, 219, L105

Tsygankov, S. S., Lutovinov, A. A., Churazov, E. M., & Sunyaev, R. A. 2006, MNRAS, 371, 19

Tsygankov, S. S., Lutovinov, A. A., Churazov, E. M., & Sunyaev, R. A. 2007, Astronomy

Letters, 33, 368

Tsygankov, S. S., Lutovinov, A. A., & Serber, A. V. 2010, MNRAS, 401, 1628

Ulmer, M. P., Baity, W. A., Wheaton, W. A., & Peterson, L. E. 1973, ApJ, 184, L117

Vasco, D., Staubert, R., Klochkov, D., et al. 2013, A&A, 550, A111

Verner, D. A., Ferland, G. J., Korista, K. T., & Yakovlev, D. G. 1996, ApJ, 465, 487

Vybornov, V., Doroshenko, V., Staubert, R., & Santangelo, A. 2018, A&A, 610, A88

Vybornov, V., Klochkov, D., Gornostaev, M., et al. 2017, A&A, 601, A126

Walter, R. & Zurita Heras, J. 2007, A&A, 476, 335

Walton, D. J., Fürst, F., Bachetti, M., et al. 2016, ApJ, 827, L13

Wang, Y.-M. & Frank, J. 1981, A&A, 93, 255

White, N. E., Davelaar, J., Parmar, A. N., Stella, L., & van der Klis, M. 1984, IAU Circ., 3912

White, N. E., Swank, J. H., & Holt, S. S. 1983, ApJ, 270, 711

Wilms, J., Allen, A., & McCray, R. 2000, ApJ, 542, 914

Wolff, M. T., Becker, P. A., Gottlieb, A. M., et al. 2016, ApJ, 831, 194

Yamamoto, T., Sugizaki, M., Mihara, T., et al. 2011, PASJ, 63, S751

Acknowledgments

Publications

Changes in the cyclotron line energy on short and long timescales in V 0332+53
V. Vybornov, V. Doroshenko, R. Staubert and A. Santangelo
Astronomy & Astrophysics, Volume 610, id.A88, p.7, 2018;

We present the results of the pulse-amplitude-resolved spectroscopy of the accreting pulsar V 0332+53 using the NuSTAR observations of the source in 2015 and 2016. We investigate the dependence of the energy of the cyclotron resonant scattering feature (CRSF) as a function of X-ray luminosity on timescales comparable with the spin period of the pulsar within individual observations, and the behavior on longer timescales within and between the two observed outbursts. We confirm that in both cases the CRSF energy is negatively correlated with flux at luminosities higher than the critical luminosity and is positively correlated at lower luminosities. We also confirm the recently reported gradual decrease in the line energy during the giant outburst in 2015. Using the NuSTAR data, we find that this decrease was consistent with a linear decay throughout most of the outburst, and flattened or even reversed at the end of the 2015 outburst, approximately simultaneously with the transition to the subcritical regime. We also confirm that by the following outburst in 2016 the line energy rebounded to previous values. The observed behavior of the CRSF energy with time is discussed in terms of changes in the geometry of the CRSF forming region caused by changes in the effective magnetospheric radius.

Luminosity-dependent changes of the cyclotron line energy and spectral hardness in Cep X-4

V. Vybornov, D. Klochkov, M. Gornostaev, K. Postnov, E. Sokolova-Lapa, R. Staubert, K. Pottschmidt and A. Santangelo

X-ray spectra of accreting pulsars are generally observed to vary with their X-ray luminosity. In particular, the hardness of the X-ray continuum is found to depend on luminosity. In a few sources, the correlation between the energy of the cyclotron resonance scattering feature (CRSF) and the luminosity is clear. Different types (signs) of the correlation are believed to reflect different accretion modes. We analyse two NuSTAR observations of the transient accreting pulsar Cep X-4 during its 2014 outburst. Our analysis is focused on a detailed investigation of the dependence of the CRSF energy and of the spectral hardness on X-ray luminosity, especially on short timescales. To investigate the spectral changes as a function of luminosity within each of the two observations, we used the intrinsic variability of the source on the timescale of individual pulse cycles (tens of seconds) , the so-called pulse-to-pulse variability. We find that the NuSTAR spectrum of Cep X-4 contains two CRSFs: the fundamental line at ~30 keV and its harmonic at ~55 keV. We find for the first time that the energy of the fundamental CRSF increases and the continuum becomes harder with increasing X-ray luminosity not only between the two observations, that is, on the long timescale, but also within an individual observation, on the timescale of a few tens of seconds. We investigate these dependencies in detail including their non-linearity. We discuss a possible physical interpretation of the observed behaviour in the frame of a simple one-dimensional model of the polar emitting region with a collisionless shock formed in the infalling plasma near the neutron star surface. With this model, we are able to reproduce the observed variations of the continuum hardness ratio and of the CRSF energy with luminosity.

Continued decay in the cyclotron line energy in Hercules X-1

R. Staubert, D. Klochkov, V. Vybornov, J. Wilms, F. Harrison
Astronomy & Astrophysics, Volume 590, id.A91, p.7, 2016

The centroid energy E_{cyc} of the cyclotron line in the spectrum of the binary X-ray pulsar Her X-1 had been found to decrease with time on a time scale of a few tens of years - surprisingly short astrophysically. This was found for the pulse phase averaged line centroid energy using observational data from various X-ray satellites over the time frame 1996 to 2012, establishing a reduction of ~4 keV. Here we report on the result of a new observation by NuSTAR performed in August 2015. The earlier results are confirmed and strengthened, with respect to both, the dependence of E_{cyc} on flux (it is still present after 2006) and the dependence on time: the long-term decay continued with the same rate, corresponding to a reduction of ~5 keV in 20 years.

12.06.1988	geboren in Tula, Russland
1995 – 2005	Schule in Tula, Russland
09.2005 – 02.2011	Studium der Physik und Astronomie (Diplom), Fakultät für Physik der Staatliche Lomonossow-Universität Moskau, Russland. Diplomarbeit: "Suche nach Sonnenflares im Röntgenbereich mit der Raumsonde Mars Odyssey" am Pushkov Institut für den Erdmagnetismus, die Ionosphäre und die Radiowellenausbreitung der Russische Akademie der Wissenschaften (IZMIRAN) unter Anleitung von Prof. Dr. M. Livshits.
04.2011 – 12.2014	Forschungsassistent am IZMIRAN, Moskau, Russland. Thema: Studie über Sonnenflares im Röntgenbereich mit dem Röntgenweltraumteleskop RHESSI und der Raumsonde Mars Odyssey.
10.2013 – 01.2015	Forschungsassistent am Weltraumforschungsinstitut der Russische Akademie der Wissenschaften (IKI RAS), Moskau, Russland Thema: "Studie über Terrestrische Gammablitze mit dem Röntgenweltraumteleskop RHESSI".
seit 03.2015	Doktorand am Institut für Astronomie und Astrophysik der Uni-Tübingen, Deutschland. Doktorarbeit: "Änderungen in den Röntgenspektren der Röntgenpulsare auf kurzen und langen Zeitskalen" unter Anleitung von Prof. Dr. Andrea Santangelo und Prof. Dr. Rüdiger Staubert.

12.06.1988	born in Tula, Russia
1995 – 2005	School in Tula, Russia
09.2005 – 02.2011	Specialist degree in Astrophysics (M.S. equivalent) at Lomonosov Moscow State University (the Faculty of Physics). Diploma project: "Search for hard X-ray solar flares with the Mars Odyssey spacecraft" under supervision of Prof. Dr. M. Livshits at Pushkov Institute of Terrestrial Magnetism, Ionosphere and Radio Wave Propagation of the Russian Academy of Sciences (IZMIRAN).
04.2011 – 12.2014	Research assistant at IZMIRAN, Moscow, Russia. Topic: "Study of hard X-ray solar flares with the RHESSI X-ray space observatory and the Mars Odyssey spacecraft".
10.2013 – 01.2015	Research assistant at the Space Research Institute of the Russian Academy of Science (IKI RAS), Moscow, Russia. Topic: "Study of Terrestrial Gamma-ray Flashes (TGFs) with RHESSI".
since 03.2015	PhD candidate at the Institute for Astronomy and Astrophysics, Uni-Tübingen, Germany. Thesis: "Changes in X-ray spectra of accreting pulsars on short and long time scales" under supervision of Prof. Dr. Andrea Santangelo and Prof. Dr. Rüdiger Staubert.